1-1-2009

Formation-Keeping Strategies At The Earth-Moon L4 Triangular Libration Point

Frank Y.W. Wong
Ryerson University

FORMATION-KEEPING STRATEGIES AT THE EARTH-MOON L4 TRIANGULAR LIBRATION POINT

by

Frank Y.W. Wong
B.Eng., Aerospace Engineering
Ryerson University, 2005

A thesis presented to Ryerson University

in partial fulfillment of the requirements for the degree of

Master of Applied Science

in the Program of

Aerospace Engineering

Toronto, Ontario, Canada, 2009

AUTHOR'S DECLARATION

I hereby declare that I am the sole author of this thesis.

I authorize Ryerson University to lend this thesis to other institutions or individuals for the purpose of scholarly research.

I further authorize Ryerson University to reproduce this thesis by photocopying or by other means, in total or in part, at the request of other institutions or individuals for the purpose of scholarly research.

ABSTRACT

FORMATION-KEEPING STRATEGIES AT THE EARTH-MOON L4 TRIANGULAR LIBRATION POINT

Frank Y.W. Wong, Master of Applied Science, Aerospace Engineering
Ryerson University, Toronto, 2009

This thesis examines the use of thrusters and solar sails for spacecraft formation keeping control at the Earth-Moon L4 point. Particular emphasis was placed on the study of underactuated control, in which fewer control inputs than the system's degrees of freedom are available. A linear LQR control scheme, an integral augmented sliding mode controller and a bang-bang controller were applied to the dynamic spacecraft system. The nonlinear controllers produced errors falling within tighter tolerances than the linear controllers in the perturbed environment. Performing similarly well as the underactuated thrusters system was the solar-sails-controlled spacecraft formation using a bang-bang controller. This shows that solar sails could be a viable propellantless technique for relative control. A linear control technique was able to bound errors to within a couple hundred metres, using a hybrid propulsion system. Of the cases studied, only the fully-actuated thrusters-based system was able to explicitly track a circular trajectory, but had a ΔV requirement of more than 100 times greater than that needed for tracking the natural, elliptical trajectory.

ACKNOWLEDGMENTS

This work would not have been possible if not for the understanding and support of my thesis supervisors, Dr. Krishna Dev Kumar and Dr. David R. Greatrix. Their guidance, patience and mentorship throughout this journey were crucial to the completion of this work. I am extremely lucky and thankful to have had them as my supervisors.

I would also like to thank Kam Shahid, Godard and Surjit Varma for their valuable insights and encouragements throughout this process. I was also very fortunate to have Ms. Mary Yu by my side. Her undying support helped to see me through the worst of times and I am forever grateful for that.

Last, but not least, I would like to thank Mr. Jerry Karpynczyk, whose wise words in the beginning will continue to motivate me in days to come.

DEDICATION

This thesis is dedicated to my parents, Ann Tsui and the late Wiltung Wong, who supported me throughout and impressed upon me a lifelong appreciation for scholarly endeavors.

TABLE OF CONTENTS

LIST OF TABLES

LIST OF FIGURES

NOMENCLATURE

$\mathbf{a}_{srp}$	Acceleration due to solar radiation pressure
A	State matrix
B	Input matrix
$C_i, C_i^{'}$	Constants in linearized solution of motion equations
D, D_1, D_2	Distance between Earth and Moon and distances from barycentre to Earth and Moon, respectively
$E_i, E_i^{'}$	Constants in linearized solution of motion equations
G	Gravitational constant $= 6.673\times10^{-11}\ \mathrm{m}^3/(\mathrm{kg\ s}^2)$
H	Matrix solved through the Matrix Riccati equations
i	Inclination angle of the Earth-Moon orbit plane relative to the ecliptic
J_i	Constants in linearized solution of motion equations
$K_{1,2,3,4,z}$	Control parameters
$\hat{\mathbf{L}}$	Unit vector in the direction of incoming solar radiation
M_1, M_2, M_3	Mass of the Earth, Moon and Sun, respectively
n	Mean motion of the Earth-Moon system, $= \sqrt{G(M_1 + M_2)/D^3}$
n_e	Mean motion of the Earth-Moon barycentre about the Sun $\approx \sqrt{\mu_3 / D_3^3}$
$\hat{\mathbf{N}}$	Unit vector normal to the illuminated surface
P	Mean solar flux, $\approx 4.5\times10^{-6} N/m^2$
P_i where $i = 1, 2, 3...$	Sliding surface coefficients in conventional SMC method
Q	State weighting matrices in LQR control scheme
R	control weighting matrices in LQR control scheme
R_1, R_2	Distance from Earth and Moon to L4 point

$\mathbf{R}$	Position vector expressed in the XYZ frame
r_1, r_2, r_3	Position relative to the Earth, Moon and Sun, respectively
r_{ij}, where $i = 1,2,3$ and $j = F, L$	Distance from body i to j satellite, where Earth is 1, Moon is 2, Sun is 3
S	Sliding surface definition
s_1, s_2, s_z	Frequencies of the Long, Short and out-of-plane motions, respectively. $s_1 \approx 0.297931$, $s_2 \approx 0.954587$, $s_z = 1$
U	Control input vector $= [u_x \quad u_y \quad u_z]^T$
U_s	Gravitational potential of the Sun
X	X-coordinate in the synodic frame with origins at the Earth – Moon barycentre
X_e	X-coordinate of the L4 Point in XYZ frame
x	x-coordinate in the synodic frame with origins at the L4 point
Y	Y-coordinates in the synodic frame with origins at the Earth – Moon barycentre
Y_e	Y-coordinates of the L4 Point in XYZ frame
y	y-coordinates in the synodic frame with origins at the L4 point
Z	Z-coordinates in the synodic frame with origins at the Earth – Moon barycentre
Z_e	Z-coordinates of the L4 Point in XYZ frame
z	z-coordinates in the synodic frame with origins at the L4 point
α	Pitch; angle between $\mathbf{a}_{srp}$ and $x - y$ plane
δ	Yaw; angle between the projection of $\mathbf{a}_{srp}$ in the $x - y$ plane and the x axis
γ	Angle between $\hat{\mathbf{N}}$ and $\hat{\mathbf{L}}$
λ	Eigenvalues of the linearized system
Λ_i where $i = 1,2$	State weighting matrix in underactuated sliding surface definitions
$\eta_{1,2,3}$	Control Parameters
κ_i	Constants in linearized solution of motion equations
μ_1, μ_2, μ_3	$= GM_1, GM_2, GM_3$, respectively

Φ	Boundary layer tolerance to remove chattering in sliding mode controller
ψ	Angular position of Sun measured in ecliptic
ρ	Mass parameter = $M_2/(M_1+M_2)$ ≈ 0.012151
$\rho_{rs}, \rho_{rd}, \rho_a$	Solar specular, diffuse and absorption coefficients, sum of which equals unity
ρ'	$M_3/M_2 = 2.7066\times10^7$
θ	Angular position of Earth-Moon line measured in Earth-Moon orbit plane
$\sigma_{1,2}$	Magnitude of control input in bang-bang control
Subscript 'd'	Denotes desired relative states
Subscript 'F, L'	Denotes values pertaining to follower or leader satellite
Subscript 'r'	Denotes relative states
$\left(\bar{\cdot}\right)$	Denotes nondimensionalized expression for quantity within brackets
$\left(\tilde{\cdot}\right)$	Denotes errors in state within brackets

ACRONYMS

CR3BP	Circular Restricted Three Body Problem
L4	Fourth Lagrange Point
LQR	Linear Quadratic Regulator
SMC	Sliding Mode Control
SRP	Solar Radiation Pressure
VSC	Variable Structure Control
VR4BP	Very Restricted Four Body Problem

Chapter 1
Introduction

1.1 Introduction

The concept of spacecraft formation flying has gained a great deal of interest in recent years. Considered to be a technology vital to future space exploration programs [1], spacecraft formation flying involves two or more spacecraft flying in particular configurations and working cooperatively towards achieving mission goals. Formation flying systems have numerous benefits over traditional single spacecraft systems. A reduction in the tasks that each spacecraft in a formation performs translates into smaller, simpler individual designs. This in turn can shorten development times and lower production costs. Mission reliability is also greatly improved, in part due to the inherent redundant nature of formation systems. In a single satellite system, a failure in the propulsion or power systems could nullify the entire mission, wasting invested resources and efforts. In a satellite formation, the failure of these systems in any one satellite would not necessarily jeopardize the mission, but rather only diminish the formations capacity to perform optimally. The replacement of a spacecraft in a formation would be much more cost effective owing to its simpler design and smaller size relative to a single, large satellite.

Aside from its potential to improve a mission's reliability and reduce development costs, formation flying missions also opens doors to mission profiles with more ambitious objectives. As an example, consider the use of a spacecraft formation for imaging

interferometry. Imaging interferometry involves combining light sources from several telescopes to form an image that is comparable in clarity to one captured by a single telescope with an unattainably large aperture size. A spacecraft formation employing this technique can capture images of space phenomenon at resolutions several times sharper than images taken by the Hubble Space Telescope. This would be an invaluable resource to researchers. Several missions currently under development will make use of imaging interferometry. They include: the Micro-Arcsecond X-ray Imaging Mission (MAXIM), which will study the accretion disk in the region of a black hole [2]; the Darwin mission, which will search for extrasolar planets [3], and; the Stellar Imager, which will study solar and stellar magnetic fields [4]. All of these missions will be located at the Sun – Earth/Moon second equilibrium point, otherwise known as the second Lagrange point (L2 point).

The Lagrangian points are the equilibrium solutions of the classical Circular Restricted Three Body Problem (CR3BP). In the CR3BP model, two primary bodies orbit about their common barycentre in circular orbits. A third object of negligible mass is added to this system and the aim is to describe the motion of this object under the gravitational influence of the two primaries. If an object were to be placed at a Lagrangian point, that object would remain motionless relative to the orbiting bodies. In total, five such equilibrium points can be found. The position of three of these points, L1, L2 and L3, are aligned with the two primary bodies whereas the remaining two, L4 and L5, form equilateral triangles with them, as shown in Figure 1.1.

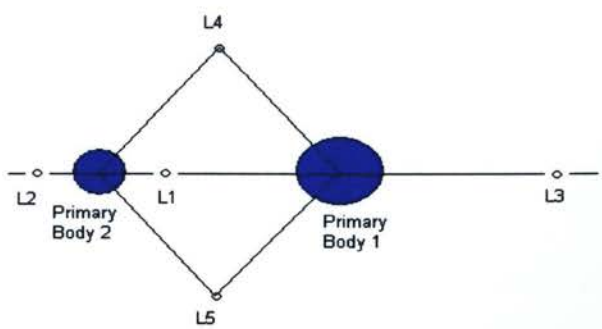

Figure 1.1 General locations of Lagrange points in a co-orbiting system

Interest in Lagrange points stem from the fact that their positions can provide unobstructed views of deep space and celestial bodies, making Lagrange point missions ideal for research purposes. Furthermore, the absence of atmospheric and magnetic field perturbations combined with the low gravitational environment allows for much lower station keeping requirements in comparison to Earth orbiting systems. Solar radiation pressure (SRP) is typically treated as a perturbing effect. However, owing to the lower station keeping requirements of Lagrange point missions, appropriate manipulations of a solar sail's orientation would provide resultant force inputs adequate for orbit control and station keeping purposes. This type of propellantless control system can reduce the system's dependency on onboard fuel, thereby reducing the onboard fuel mass requirements and costs. Furthermore, using SRP presents a viable means to retain or regain control if primary control methods were to fail.

Although all Lagrange point missions as of now have been deployed at the Sun-Earth L1 or L2 points, the reasons for choosing these points have been rooted in mission requirements, or the avoidance of the higher costs and engineering challenges associated with traveling much greater distances to reach the other Lagrange points in the Sun-Earth [5]. However, with advances in technology, the size and weight of satellites can be greatly reduced. This in turn results in mass savings for the launch vehicle and ultimately leads to lower overall costs. Missions to the triangular Lagrange points in the Sun-Earth system and even other Lagrange points in the Solar system will become feasible in the near future; allowing missions to take advantage of the stable properties near the triangular libration points.

Lagrange points exist in the Earth-Moon system as well. These points are reasonably accessible and have similar advantages to those offered by the Sun-Earth/Moon Lagrange points. Farquhar [6] presented some uses of libration points in the Earth-Moon system and studied the control of single satellites about them. With recent renewed efforts to return to the Moon, it is likely that these points will be used for lunar mission support purposes. In the CR3BP, motion about these points are bounded, making them ideal

locations for a variety of applications, including imaging interferometry, communication relay satellites and space stations. However, this model neglects the effect of the Sun's gravitational pull and the eccentricity of the Earth-Moon orbit. The value of these points to future space missions necessitates the study and development of effective control strategies to counter these perturbations.

In this thesis, strategies for controlling a spacecraft formation system at the Earth-Moon L4 point are developed. Specifically, the issue of relative control in the presence of strong perturbing effects from the Sun's gravity is addressed. The use of thrusters is the most popular choice for satellite control actuation and hence is investigated in this study. Solar sails are also examined in order to assess the feasibility of using this propellantless method for control.

1.2 Literature Review

Research related to Lagrange points has been ongoing since their discovery, reflecting the complexity as well as the interest in these points. The research covers a broad range of topics, including studies into the motion of objects near these points, conditions for their existence, the effect of perturbing forces on their existence, stability of the points, the search for natural orbits about them, and control of spacecraft in the vicinity of them, just to name a few. Given the vast amount of research available that directly pertains to this thesis, it was necessary to organize the literature review based on the main research areas.

This literature review will be organized as three subsections. The first deals with dynamics, stability and the search for periodic orbits for the triangular libration points. Next, published results pertaining to formation flying and control at Lagrangian points will be reviewed. Finally, selected publications regarding the use of SRP for spacecraft control will be briefly summarized.

1.2.1 Dynamics, Stability and Periodic Orbits

The majority of research regarding Lagrange points has been focused on the natural motions of an object placed near them. More specifically, they examined whether or not objects with non zero initial velocities would remain in the region of these points. Much emphasis has also been placed on finding initial conditions that would allow for closed, periodic trajectories to be observed. Numerous texts briefly discuss the restricted three body problem; [7,8,9] are but a couple of them. Few authors, however, go into as much depth and discuss the intricacies of the problem as Szebehely did [10]. In it, he presents the fundamentals of the problem and also applied complex analytical methods to support discussions regarding the motion and stability of objects near the Lagrangian points. Most of his work, however, was based on linear analysis, and only covered research up to 1967.

Gomez, Jorba, Masdemont and Simo [11] presented more recent findings in their four volume text covering the dynamics near libration points. Separate volumes are dedicated to the discussions of motion around the triangular and collinear points. They cover the fundamentals of the problem, summarize more recent findings and discuss the station-keeping strategies for missions about these points. Heavy emphasis is placed on numerical analysis and simulation of motions near the Earth-Sun Lagrange points.

In spite decades of research into the stability of the Earth-Moon triangular libration points, uncertainty regarding the stability and the conditions necessary for bounded motions to be observed in the nonlinear system continue to persist. It was generally agreed upon that a projected spacecraft's trajectory could be greatly altered with only slight variations to initial conditions, and that stability within the orbital plane of the primaries was heavily dependent on their respective masses [12,13]. Motion perpendicular to the plane of orbit of the primaries were found to be stable [14] and is generally not disputed. Differences in opinion emerge regarding what particular mass values could give rise to bounded motions, and if the triangular points of the Earth-Moon system are naturally stable.

Findings of mass ratios allowing stable motions to occur within the orbital plane of the two primaries were often contradictory. Studies to find the critical mass ratio, that is, the maximum ratio of the masses of the two primary bodies for which bounded motions about the triangular points could exist, were often contradictory. One study found that only mass ratios less than a critical value of 0.03852 could allow stable motions [15]. Yet, another study found that the critical mass ratios deduced using linear stability analysis on the classical model did not hold in the relativistic model, concluding that only a mass ratio greater than 0.5 could attain truly stable motions [16]. However, simulations of satellite motion about the Sun-Jupiter and Earth-Moon L4 point, both of which have mass ratios below 0.5, implied otherwise, demonstrating that bounded motions sufficiently stable for practical applications could exist in these systems [17].

With regards to the stability of the triangular points in the Earth-Moon system, linear analysis implies bounded motions in the orbital plane. The motion itself can be described as a superposition of two natural periodic orbits; one that is 28.6 days and another that is approximately 3 months. The ratio of these two periods is approximately 3:1, which was the commensurability ratio studied in [18]. It was found that motions with a 3:1 commensurability ratio were unstable, despite the absence of external perturbations. This was counter to the argument put forth in [19] and several other texts that nonlinearities do not destabilize the motion at the Earth-Moon L4 point, but perturbing forces would. The motion is naturally bounded but only in the absence of solar gravitational forces, which acts as the destabilizing factor in the real system. In fact, it is stressed in several preliminary studies of motion in the Earth-Moon system that results cannot be considered accurate without inclusion of the Sun's perturbing effect on the system.

Recognizing the inability of the CR3BP model to accurately describe motion in the disturbed system, several authors conducted studies into the existence of stable points in a perturbed environment. Danby [20] studied the effects of non-spherical primary bodies and the addition of a fourth body to the CR3BP, finding that stable motion was attainable near the L4 point, but stressed that his linear analysis was an oversimplification of a real system. Treating the Sun as the fourth body, de Vries studied its effect on the motion of

objects near the Earth-Moon L4 point in [21]. His results were deduced using a coplanar model with zero eccentricity and varied greatly from simulations using ephemeris positions. Breakwell, Pringle and others used advanced perturbation analysis techniques in [22 – 24] and found that the perturbed system was generally unstable.

The sensitivities of the nonlinear, Sun perturbed system was highlighted in [25], where Schechter, using a model that neglected the inclination of the Earth-Moon system relative to the ecliptic, determined that even small deviations from the L4 point would grow large over time. This is in agreement with Tapley, Lewellan and Schutz results in [26] and [27], which also showed an increasing amplitude in the out of plane motion when the Earth-Moon inclination was factored into the analysis. A trajectory that expanded and contracted until approximately 3900 days before leaving the Earth-Moon system was observed in their simulations. The amplitude of the motion was approximately 220,000 km, and the period of motion was determined to be approximately 1500 days. The sensitivities of this system's dynamics were clearly demonstrated in a later study by the same authors [28]. In this work, it was shown that small changes to the constants in the equations of motion was found to have drastically increased the duration by which the spacecraft remained in the region of the L4/L5 points of the Earth-Moon system.

Solar radiation pressure, the shape of the primaries and eccentricity of their orbits also affects the stability of the L4 point, although not in the same capacitance that a fourth attractive body would. The effect of radiation pressure from one primary body on the stability and location of the L4 point was studied in [29-32]. The position of the equilibrium point was found to shift under the effect of solar radiation, but the adjusted L4 point remained generally stable for all L4 points in the solar system. The analysis was extended in [33] and [34] to include oblate and eccentricity effects, drawing similar conclusions regarding stability so long as the eccentricity values were small. Considering only the eccentricity Earth-Moon orbit, Colombo [35] found that the L4 point remained stable, but that its degree of stability decreased.

Since analytical studies could not bring about consensus over the issue of the Earth-Moon L4 point's stability, experimental and numerical studies using ephemeris models were required. A famous experiment conducted by Francisco and Freitas involved a visual search for objects in the region, which would imply that sufficiently stable conditions existed for practical purposes. The results of this photographic search for objects in the vicinity of the Earth-Moon L4 point were presented in [36]. In that study, no objects were found, implying unstable conditions. However, the search was limited by the resolution of the imaging system, which could only detect objects that were at least several metres in diameter. Numerical simulations using ephemeris models were conducted in [37] and [38]. These simulations found quasi stable regions outside of the Earth-Moon plane and generally unstable motions over large time scales, save for a few select initial conditions. This highlights the sensitivities of the dynamics to initial states and epochs. Ephemeris models were also used by Schutz to assess the possibility of space colonies located at the L4 point [39]. His results showed that an object would leave the Earth-Moon system within 1300 days, but he stressed that more favorable initial conditions could extend that period. Munoz numerically searched for such initial conditions [40]. He limited his search by focusing on conditions that would result in periodic motions, and motions with minimal deviations from the L4 point using ephemeredes models. He found several instances in which libration amplitudes near the L4 point would be small, but that the existence of such scenarios were heavily dependent upon the initial positions of the primary bodies in the system.

Several articles pertaining to the search for periodic and bounded motions using analytical methods predate Munoz's numerical study. Of particular interest was the existence of such motions in the presence of the Sun's gravitational perturbations. In [25], Schechter predicted the existence of coplanar periodic orbits in the Sun perturbed system which was later verified by the analysis of Kolenkiewicz and Carpenter [41]. More specifically, he predicted that such an orbit could exist for the L4 point, but that its stability would be marginal. Rand and Podgorski [42] suggested a time independent method of finding approximate periodic orbits using geometrical dynamics and Fourier transforms. In [43], mechanisms causing the termination of short and long period motion

was investigated. These studies focused on using analytical methods to obtain results. Advances in computational capabilities have allowed researchers to find numerous periodic orbits about the L4 point, but only a few are considered to be applicable to practical missions [44].

1.2.2 Formation Flight Dynamics and Control

Most research into spacecraft formation flight about Lagrangian points has been focused on the Sun-Earth/Moon or Earth-Moon L1 and L2 collinear points. Segerman and Zedd's [45] preliminary dynamics analysis for formation flight about the Sun-Earth L2 point made use of the CR3BP model to derive planar relative equations and were able to find analytical solutions to them. Luquette [46] linearized the relative equations of motion and applied a linear control scheme to the system and found that linear control was generally validated for formation flight. Howell and Marchand [47] provide a summary of prior research done regarding formation flight at the Sun-Earth/Moon L1 and L2 collinear points. In this, they discuss different control strategies for formation control of natural and non-natural formations. They also developed optimal feedback control laws for the reconfiguration of satellites at the Sun-Earth/Moon L2 point in [48]. Li [49] developed open and closed loop control methods for formation reconfiguration using SRP forces at the Sun-Earth/Moon and Earth-Moon L2 points.

With regard to formation flying at the Earth-Moon triangular libration points, there has not been much emphasis in the literature. Catlin and Mclaughlin completed preliminary formation flight analysis at these points in [5,50]. They build upon previous work in [10] to derive linearized, relative equations of motion for a formation-flying pair of spacecraft for various formation flying configurations. They determined that the largest source of errors in their model was the neglect of solar gravitational effects on the system, followed by neglecting solar radiation pressure effects and the Earth's oblateness. Their analysis showed that not accounting for the Sun's gravity resulted in relative errors that were 2 orders of magnitude greater than that of the unperturbed case. This helps to illustrate the

need to incorporate solar gravitational effects for a more accurate representation of the system's dynamics.

1.2.3 Solar Radiation Pressure Modeling and Control

The subject of solar sails has been covered extensively by McInnes in [51] where he discusses modeling, applications, construction and the history of solar sails, among other topics. In [52], he and other researchers propose the use of solar sails for stabilizing motions at the Sun-Earth/Moon and Earth-Moon Lagrange points. Smirnov, Ovchinnikov and Guerman [53] extended this further to using solar sails to maintain a satellite formation in heliocentric orbit. Baoyin and McInnes [54] showed that artificial out of plane Lagrange point orbits could be achieved using sails. Although the orbit was dynamically unstable, they showed that the system was controllable using solar sails.

1.3 Motivation

From the literature survey, it is clear that the dynamics of the Earth-Moon L4 point are difficult to accurately model. In the presence of modeling simplifications and uncertainties, the applicability of a controller developed using such models to the real Earth-Moon system is difficult to assess. However, these points are accessible and are stable according to the CR3BP analysis. This makes them ideal locations for a wide range of formation flight applications, such as imaging interferometry missions and automated spacecraft or space station servicing missions. Due to the destabilizing effect of perturbing forces and the precision requirements of some proposed formation flying missions, disturbances to the system must be effectively countered by a control system. A robust controller could accomplish this task. In addition, SRP, traditionally seen as a source of perturbation, has emerged as a potential control input for Lagrange point orbits. Thus, the development of innovative control schemes could make formation flight missions possible about the Earth-Moon triangular libration points.

1.4 Scope of Thesis and Research Objectives

The aim of this research is to develop preliminary control algorithms that will accomplish spacecraft formation-keeping tasks and relative orbit corrections for missions at the Earth-Moon L4 point. Dynamic models will include the effects of Earth-Moon orbital plane inclinations relative to the ecliptic and solar gravitational perturbations. All other sources of perturbations will be considered minor and out of the scope of the present research.

1.5 Contribution of Thesis

This thesis presents the following contributions to the field of satellite control:

1) Development of closed-loop linear and nonlinear control algorithms for spacecraft formation control near the Earth-Moon L4 point;
2) Analyzing the use of thrusters in fully and underactuated configurations for the control of in-plane elliptical and circular formation configurations
3) Studying the use of solar sails as a means of providing control accelerations, and;
4) Proposing the use of a hybrid propulsion system to maintain natural formation trajectories.

1.6 Thesis Organization

This thesis will be presented in the following order. In Chapter 2, the dynamic modeling of the system is developed. Here, the CR3BP is discussed, including its use in determining the various Lagrange points, the stability properties about these points, and how this model can be applied to this present research. Modifications necessary for the inclusion of the Sun's gravitational effect will be shown, forming a system more accurately described by the very restricted four body problem (VR4BP). Equations of relative motion for a formation flying pair of spacecraft are then derived for satellites flying about the Earth-Moon L4 point and discussed in depth. A simplified model for solar radiation pressure will also be briefly discussed in this chapter.

Chapter 3 will focus on providing background information regarding the various control methods applied in this research, including linear quadratic regulator and variable structure control techniques. Control laws for the formation system controlled using thrusters and solar sails will also be developed in this chapter. Simplifications which helped facilitate the development of the control laws will be discussed.

The results of the thruster controlled scenario are presented and discussed in depth in Chapter 4. The need for control is first established through some simple open-loop simulations of the systems dynamics in the linear and nonlinear systems. Both linear and nonlinear techniques are applied to progressively complicated models of the system, culminating in the relative control of the solar gravitationally-perturbed system using thrusters in an underactuated configuration. Comparisons between the performances of various controllers will be discussed and their fuel consumption requirements will be analyzed.

Chapter 5 presents the simulation results for a system controlled using solar sails. The efficacy of the closed loop controllers applied here will be discussed under various scenarios, including for initial state errors and for control under a strong perturbing force. These results are compared to the thruster-controlled scenario to assess the effectiveness of the solar-sail-controlled system.

A hybrid propulsion system using both solar sails and thrusters simultaneously for control is proposed in Chapter 6. This approach is applied directly to the solar gravitationally perturbed system, and the controller's performance is analyzed. Comparisons will be made to the performance of similar controllers in the thruster and solar sail controlled systems.

Finally, Chapter 7 presents some suggestions for future research, and offers some concluding remarks regarding the validity of this research.

Chapter 2

Motion Near Earth-Moon Triangular Libration Points

2.1 Introduction

In this chapter, the dynamic model describing the natural motions near the Earth-Moon L4 point is developed. Since the circular restricted three body problem forms the foundation of the dynamic model, it is discussed in some detail here. Discussions will include expressing the nonlinear equations of motion in non-dimensional and linearized form, the determination of the Lagrange points, and the stability of these points in the absence of perturbations.

The motion in the Earth-Moon system can be described by the circular restricted three-body model. However, this model does not represent a true model; mainly, because it does not account for the perturbing effect of the Sun. To partially remedy this, solar gravitational effects are modelled and added to the system to form a more accurate system model, as was done in [26]. Although still not a perfect system model, this model is sufficiently accurate over short time intervals of a few months for practical purposes.

Solar radiation pressure (SRP) is also modelled in this chapter. However, in this thesis, SRP is not considered as a disturbance to the system. Rather, it is to be manipulated through changes to a sail's orientation to provide desired control accelerations. This is

followed by derivations of the relative equations of motion for a formation flying pair of satellites, which is the last topic of this chapter.

2.2 Assumptions and Simplifications

Some assumptions were made to simplify the model and analysis. They are listed as follows:

1) Perturbations from Earth's oblateness (J2) and other planetary perturbations were considered minor, and were not taken into account.
2) Shadowing effects are neglected since the time span in which a satellite is shadowed by the primary bodies is small.
3) Attitude is assumed to be controlled by a separate attitude control system.
4) Torques due to the resultant input forces is assumed negligible; this is equivalent to assuming control forces act through the system's centre of mass.
5) The Sun perturbs the motion of the satellites only, and does not affect the assumed circular motions of the Earth and Moon.
6) The equilibrium points of the three-body system are assumed to remain fixed in the presence of disturbances due to solar gravity and eccentricity of the primaries.

2.3 Restricted Three-Body Problem

The circular restricted three-body problem can be seen as a simplified model of the generalized three-body problem in which three bodies in space mutually exert gravitational influence over the motion of the each other. The challenge is to find a solution describing the motion of each body. In the circular restricted three-body problem, it is assumed that the mass of one of the objects is small and has negligible effects on the motion of the other two larger, primary bodies. Furthermore, it is assumed that the two larger bodies move about their gravitational mass centres in a circular orbit,

thereby reducing the problem to one of determining the motion of the small mass only. Even with such simplifications, finding a solution to this problem has proven difficult.

One complicating factor is the lack of constants of motion in the three body problem. Henri Poincare proved near the end of the 19th century that the lack of constants in the motion rendered it impossible for a closed form solution to this problem to be found. The advent of computers and the rapid improvements in processing power has allowed for the numerical integration of the equations. However, this system is very sensitive to initial conditions; that is, small variations in initial states can drastically affect the system behaviour over time, and even small integration errors can hamper the numerical accuracy of the results over time. As such, simulation time frames should be limited to shorter time frames where possible. The following is a formulation of the restricted three-body problem found in [7].

Consider a system of two large masses, M_1 and M_2, orbiting about their common barycentre, as shown in Figure 2.1. The XYZ frame is a rotating frame with its origins at the barycentre. Its angular velocity is equal to the mean motion, n, of the two larger masses and is directed out of the page, in the Z direction. The unit direction vectors are $\hat{i}, \hat{j}, \hat{k}$, with the $\hat{k}$ vector pointing out of the page.

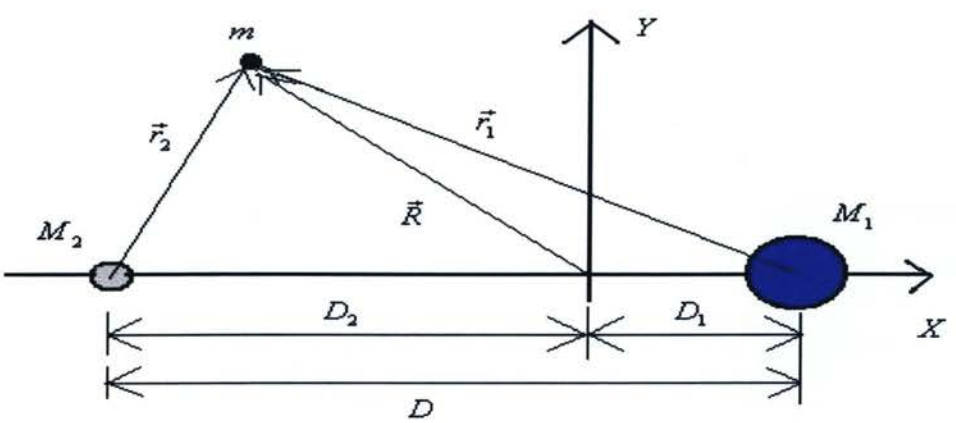

Figure 2.1 Rotating frame with origins at system barycentre

A small mass, m, is added to this model. Its position is defined by the vector **R** and its position relative to M_1 and M_2 are denoted as vectors $\vec{r}_1$ and $\vec{r}_2$, respectively. The distances between the masses and the barycentre are defined as $D_{1,2}$ and are shown in Figure 2.1.

The position of m can be broken into directional components as

$$\vec{\mathbf{R}} = X\hat{i} + Y\hat{j} + Z\hat{k} \tag{2-1}$$

Note that the derivatives of i and j are not zero because of the rotation relative to the inertial frame. The derivatives of $\hat{i}, \hat{j}, \hat{k}$ can be summarized as follows:

$$\begin{aligned} \dot{\hat{i}} &= \hat{n} \times \hat{i} = n(\hat{k} \times \hat{i}) = n\hat{j} \\ \dot{\hat{j}} &= \hat{n} \times \hat{j} = n(\hat{k} \times \hat{j}) = -n\hat{i} \\ \dot{\hat{k}} &= \hat{n} \times \hat{k} = n(\hat{k} \times \hat{k}) = 0 \end{aligned} \tag{2-2}$$

Here, the angular velocity vector $\hat{n}$ points in the direction of the Z axis and its magnitude can be found from

$$n = \sqrt{\frac{G(M_1 + M_2)}{D^3}} \tag{2-3}$$

Taking the second derivative of Eq. (2-1) and substituting in Eq. (2-2), the inertial acceleration of m can be found to be

$$\ddot{\vec{\mathbf{R}}} = \left(\ddot{X} - 2n\dot{Y} - n^2 X \right)\hat{i} + \left(\ddot{Y} + 2n\dot{X} - n^2 Y \right)\hat{j} + \ddot{Z}\hat{k} \tag{2-4}$$

A force function can be found using Newton's second law and the theory of universal gravitation:

$$\vec{\mathbf{F}} = m\ddot{\vec{\mathbf{R}}} = -\frac{GM_1 m}{r_1^3}\vec{\mathbf{r}}_1 - \frac{GM_2 m}{r_2^3}\vec{\mathbf{r}}_2 \tag{2-5}$$

The vectors $\vec{\mathbf{r}}_1$ and $\vec{\mathbf{r}}_2$ can be deduced from Figure 2.1 as being:

$$\vec{\mathbf{r}}_1 = \left(X - D_1\right)\hat{i} + Y\hat{j} + Z\hat{k} \tag{2-6a}$$

$$\vec{\mathbf{r}}_2 = \left(X + D_2\right)\hat{i} + Y\hat{j} + Z\hat{k} \tag{2-6b}$$

Substituting Equation (2-6) into Equation (2-5) and equating the directional components of Equation (2-4) and Equation (2-5), the equations of motion for m can be expressed as

$$\ddot{X} - 2n\dot{Y} - n^2 X = -\frac{\mu_1(X - D_1)}{r_1^3} - \frac{\mu_2(X + D_2)}{r_2^3} \tag{2-7a}$$

$$\ddot{Y} + 2n\dot{X} - n^2 Y = -\frac{\mu_1 Y}{r_1^3} - \frac{\mu_2 Y}{r_2^3} \tag{2-7b}$$

$$\ddot{Z} = -\frac{\mu_1 Z}{r_1^3} - \frac{\mu_2 Z}{r_2^3} \tag{2-7c}$$

where constant values of GM_1 and GM_2 have been expressed as μ_1 and μ_2 to simplify the equations.

The equations of motion can be expressed in non dimensional form through the substitutions described in [10]. Setting the unit of distance equal to D, the unit of mass equal to $M_1 + M_2$, $\rho = \frac{M_2}{M_1 + M_2}$, and the unit of time equal to n^{-1}, substitution into equations (2-7a,b,c) yields

$$\ddot{\bar{X}} - 2\dot{\bar{Y}} - \bar{X} = -\frac{(1-\rho)(\bar{X}-\rho)}{\bar{r}_1^3} - \frac{\rho(\bar{X}+1-\rho)}{\bar{r}_2^3} \tag{2-8a}$$

$$\ddot{\bar{Y}} + 2\dot{\bar{X}} - \bar{Y} = -\frac{(1-\rho)\bar{Y}}{\bar{r}_1^3} - \frac{\rho\bar{Y}}{\bar{r}_2^3} \tag{2-8b}$$

$$\ddot{\bar{Z}} = -\frac{(1-\rho)\bar{Z}}{\bar{r}_1^3} - \frac{\rho\bar{Z}}{\bar{r}_2^3} \tag{2-8c}$$

where bar represents nondimensional quantities. It should be noted that the period of the orbit is equal to 2π in this representation. The distances $\bar{r}_1$ and $\bar{r}_2$ can be expressed as

$$\bar{r}_1 = \sqrt{\left(\bar{X}-\rho\right)^2 + \bar{Y}^2 + \bar{Z}^2} \tag{2-9a}$$

$$\bar{r}_2 = \sqrt{\left(\bar{X}+1-\rho\right)^2 + \bar{Y}^2 + \bar{Z}^2} \tag{2-9b}$$

2.4 Equilibrium Points

It is well known that five stationary points exist in the CR3BP. These equilibrium points were discovered by Euler and Lagrange in the mid-18th century, and have garnered much interest since the mid-20th century with the development of satellites. Such points could be ideal locations for placing communications relay satellites, space research satellites, mission support satellites, and even space stations. Understanding how these points are determined is useful to the study of satellite orbits about these points. The determination of the five equilibrium points' locations was shown in [8] using the nondimensionalized equations of motion and briefly summarized in this section.

Collinear Equilibrium Points

At the equilibrium points, the velocity and acceleration relative to the two larger bodies is zero. Substituting this into Equations (2-8), we have

$$-\bar{X} = -\frac{(1-\rho)(\bar{X}-\rho)}{\bar{r}_1^3} - \frac{\rho(\bar{X}+1-\rho)}{\bar{r}_2^3} \tag{2-10a}$$

$$-\bar{Y} = -\frac{(1-\rho)\bar{Y}}{\bar{r}_1^3} - \frac{\rho\bar{Y}}{\bar{r}_2^3} \tag{2-10b}$$

$$0 = -\frac{(1-\rho)\bar{Z}}{\bar{r}_1^3} - \frac{\rho\bar{Z}}{\bar{r}_2^3} \tag{2-10c}$$

From Equation (2-10c), it can immediately be deduced that the Z components of the equilibrium positions are zero. Hence, all equilibrium points of a restricted three body system lie in the XY plane.

If $\bar{Y}$ is set to zero in Equation (2-10b), then the only equation of significance left is Equation (2-10a). Substituting Equation (2-9) into Equation (2-10a) as well as the result $\bar{Y} = \bar{Z} = 0$, we obtain

$$\bar{X} = \frac{(1-\rho)(\bar{X}-\rho)}{\left((\bar{X}-\rho)^2\right)^{3/2}} + \frac{\rho(\bar{X}+1-\rho)}{\left((\bar{X}+1-\rho)^2\right)^{3/2}}, \qquad 0<\rho<1 \tag{2-11a}$$

Equation (2-11a) can be solved numerically for the three real roots that satisfy the condition of $\rho < 1$. Alternatively, when the sign of the square root terms are accounted for, Equation (2-11a) can be expressed as three 5th-order equations valid only in the ranges specified:

$$\bar{X} = -\frac{(1-\rho)}{(\bar{X}-\rho)^2} + \frac{\rho}{(\bar{X}+1-\rho)^2}, \qquad -1+\rho < \bar{X} < \rho \tag{2-11b}$$

$$\bar{X} = -\frac{(1-\rho)}{(\bar{X}-\rho)^2} - \frac{\rho}{(\bar{X}+1-)^2}, \qquad -1+\rho > \bar{X} \tag{2-11c}$$

$$\bar{X} = \frac{(1-\rho)}{(\bar{X}-\rho)^2} + \frac{\rho}{(\bar{X}+1-\rho)^2}, \qquad 1-\rho < \bar{X} \tag{2-11d}$$

These roots represent the positions of the first 3 equilibrium points, known as the collinear equilibrium points because they lie on the line joining the primary bodies. For the Earth-Moon system, $\rho \approx 0.012151$. Solving the above equation, the nondimensionalized coordinates of the collinear points in the Earth-Moon system are [9]:

$$L_1 \rightarrow \bar{X} = -0.8369$$
$$L_2 \rightarrow \bar{X} = -1.1560$$
$$L_3 \rightarrow \bar{X} = 1.005$$

Triangular Equilibrium Points

In the collinear case, it was assumed that the Y component of the equilibrium points were zero. If Y does not equal zero, then Equation (2-10b) can be expressed as

$$1 = \frac{(1-\rho)}{\bar{r}_1^3} + \frac{\rho}{\bar{r}_2^3} \tag{2-12}$$

Substituting Equation (2-12) into Equation (2-10a), we have

$$\bar{X} = \left(1 - \frac{\rho}{\bar{r}_2^3}\right)(\bar{X} - \rho) + \frac{\rho(\bar{X} + 1 - \rho)}{\bar{r}_2^3} \tag{2-13}$$

Simplifying Equation (2-13), we find the result $\bar{r}_2 = 1$. Substituting this back into Equation (2-12), and solving, we find that $\bar{r}_1 = 1$ as well. Therefore, with $\bar{r}_1 = \bar{r}_2 = 1$, we can equate Equations (2-9a) and (2-9b) to find the X component of the triangular equilibrium points. Bearing in mind that Z was found to be zero in all cases, we have

$$\left(\bar{X} - \rho\right)^2 = \left(\bar{X} + 1 - \rho\right)^2 \tag{2-14}$$

Solving Equation (2-14) yields $X = \rho - \frac{1}{2}$. Substituting this result into Equation (2-9a) or (2-9b) and solving for Y gives $Y = \pm\frac{\sqrt{3}}{2}$. Figure 2.2 shows the equilibrium points in a general restricted three body system.

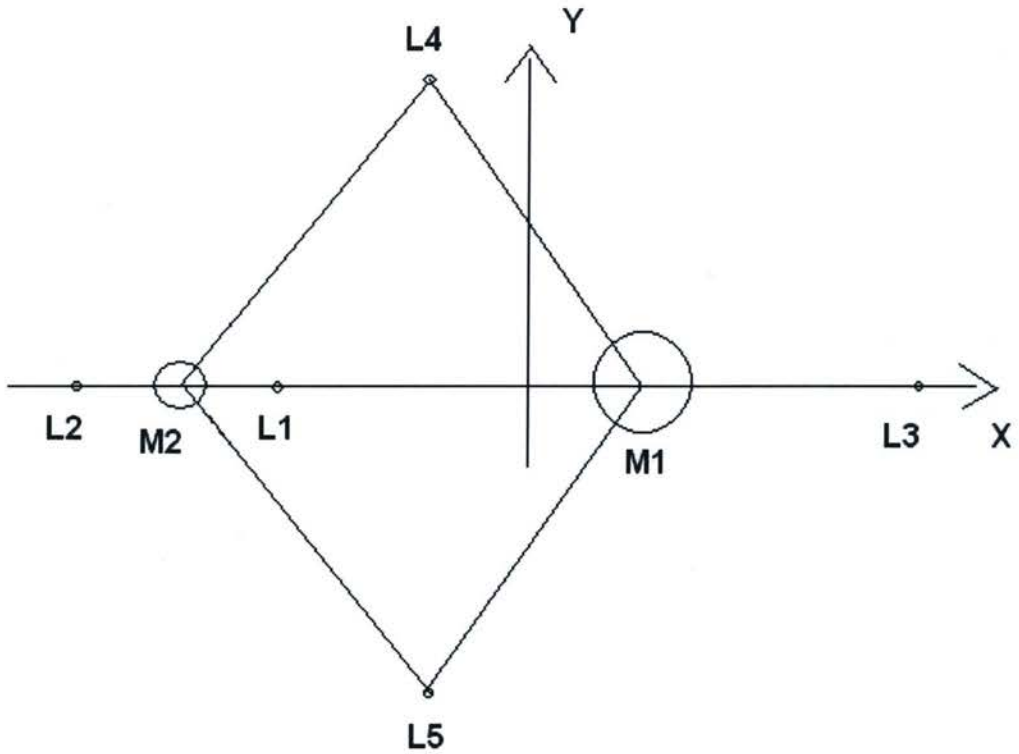

Figure 2.2 Positions of the equilibrium points in a general three body system

2.5 Motion About The L4 Point

If the motion of an object in the vicinity of the Lagrange points remain bounded with time or tends to come to rest at the points themselves, then these points are stable. Linear stability analysis for the stability of each point was developed in [7] and [8], and is briefly summarized here.

Linearized Equations of Motion

Equation (2-8) can be linearized using the procedure described in [8]. Consider an object in the vicinity of an equilibrium point. The co-ordinates of such an object can be expressed as

$$\bar{X} = \bar{X}_e + \bar{x} \tag{2-15a}$$

$$\bar{Y} = \bar{Y}_e + \bar{y} \tag{2-15b}$$

$$\bar{Z} = \bar{z} \tag{2-15c}$$

where the co-ordinates of the equilibrium point are $\left(\bar{X}_e, \bar{Y}_e, 0\right)$, and $\bar{x}, \bar{y}, \bar{z}$ represent small displacements from the equilibrium point. The values $\bar{r}_1^{-3}$ and $\bar{r}_2^{-3}$ appearing in Equation (2-8) can be expanded using Equation (2-9).

$$\bar{r}_1^{-3} = \left[\left(\bar{X}_e + \bar{x} - \rho\right)^2 + \left(\bar{Y}_e + \bar{y}\right)^2 + \bar{z}^2\right]^{-\frac{3}{2}} \tag{2-16a}$$

$$\bar{r}_2^{-3} = \left[\left(\bar{X}_e + \bar{x} + 1 - \rho\right)^2 + \left(\bar{Y}_e + \bar{y}\right)^2 + \bar{z}^2\right]^{-\frac{3}{2}} \tag{2-16b}$$

Expanding out Equations (2-16a) and (2-16b),

$$\bar{r}_1^{-3} = \left(\left(\bar{X}_e^{\,2} + \bar{Y}_e^2 - 2\rho\bar{X}_e + \rho^2\right) + 2\left(\bar{x}\bar{X}_e - \rho\bar{x} + \bar{Y}_e\bar{y}\right)\right)^{-\frac{3}{2}} \tag{2-17a}$$

$$\bar{r}_2^{-3} = \left(\left(\bar{X}_e^{\,2} + \bar{Y}_e^2 - 2\rho\bar{X}_e - 2\rho + 2\bar{X}_e + \rho^2 + 1\right) + 2\left(\bar{x}\bar{X}_e - \rho\bar{x} + \bar{x} + \bar{Y}_e\bar{y}\right)\right)^{-\frac{3}{2}} \tag{2-17b}$$

The first bracketed term of Equations (2-17a) and (2-17b) are constants. The higher order terms $\bar{x}^2, \bar{y}^2$ and $\bar{z}^2$ have been neglected. Expressing them in an alternative form,

$$\bar{r}_1^{-3} = \left(\left(\bar{X}_e - \rho\right)^2 + \bar{Y}_e^2 + 2\left(\left(\bar{X}_e - \rho\right)\bar{x} + \bar{Y}_e\bar{y}\right)\right)^{-\frac{3}{2}} \tag{2-17c}$$

$$\bar{r}_2^{-3} = \left(\left(\bar{X}_e + 1 - \rho\right)^2 + \bar{Y}_e^2 + 2\left(\left(\bar{X}_e - \rho + 1\right)\bar{x} + \bar{Y}_e y\right)\right)^{-\frac{3}{2}} \tag{2-17d}$$

Assuming that $x << \bar{r}_{1,2}$ and $y << \bar{r}_{1,2}$, a first order approximation can be made by expanding using the binomial theorem and neglecting higher order terms. The binomial theorem is given as

$$(a+x)^n \approx a^n + na^{n-1}x + \frac{n(n-1)}{2}a^{n-2}x^2 + \ldots + x^n \tag{2-18}$$

where a is a constant. Treating $\left(\bar{X}_e + 1 - \rho\right)^2 + \bar{Y}_e^2$ as the a term, $2\left(\left(\bar{X}_e - \rho + 1\right)\bar{x} + \bar{Y}_e y\right)$ as the x term, applying the binomial theorem to Equation (2-17) and neglecting higher order terms yields

$$\begin{aligned} \bar{r}_1^{-3} \approx & \left[\left(\bar{X}_e - \rho\right)^2 + \bar{Y}_e^2\right]^{-\frac{3}{2}} \\ & -3\cdot\left[\left(\bar{X}_e - \rho\right)^2 + \bar{Y}_e^2\right]^{-\frac{5}{2}}\cdot\left(\left(\bar{X}_e - \rho\right)\bar{x} + \bar{Y}_e\bar{y}\right) \end{aligned} \tag{2-19a}$$

$$\begin{aligned} \bar{r}_2^{-3} \approx & \left[\left(\bar{X}_e + 1 - \rho\right)^2 + \bar{Y}_e^2\right]^{-\frac{3}{2}} \\ & -3\cdot\left[\left(\bar{X}_e + 1 - \rho\right)^2 + \bar{Y}_e^2\right]^{-\frac{5}{2}}\cdot\left(\left(\bar{X}_e - \rho + 1\right)\bar{x} + \bar{Y}_e\bar{y}\right) \end{aligned} \tag{2-19b}$$

The terms $\left[\left(\bar{X}_e + \rho\right)^2 + \bar{Y}_e^2\right]^{\frac{1}{2}}$ and $\left[\left(\bar{X}_e + 1 - \rho\right)^2 + \bar{Y}_e^2\right]^{\frac{1}{2}}$ represent the distances from the equilibrium point to each of the larger bodies, which are constant. Let these two terms be represented by $\bar{R}_1$ and $\bar{R}_2$, respectively. Substituting into Equation (2-8) and simplifying gives Equations (2-20a,b,c). These equations represent a linear approximation of motion and are valid only in the vicinity of the equilibrium points.

$$\ddot{\bar{x}} - 2\dot{\bar{y}} - \bar{x} = -\left[(1-\rho)\left(\frac{1}{\bar{R}_1^{\,3}} - 3\frac{\left(\bar{X}_e - \rho\right)^2}{\bar{R}_1^{\,5}}\right) + \rho\left(\frac{1}{\bar{R}_2^{\,3}} - 3\frac{\left(\bar{X}_e + 1 - \rho\right)^2}{\bar{R}_2^{\,5}}\right)\right]\bar{x} + \left[3(1-\rho)\frac{\left(\bar{X}_e - \rho\right)\bar{Y}_e}{\bar{R}_1^{\,5}} + 3\rho\frac{\left(\bar{X}_e + 1 - \rho\right)\bar{Y}_e}{\bar{R}_2^{\,5}}\right]\bar{y} \tag{2-20a}$$

$$\ddot{\bar{y}} + 2\dot{\bar{x}} - y = \left[3(1-\rho)\frac{\left(\bar{X}_e - \rho\right)\bar{Y}_e}{\bar{R}_1^{\,5}} + 3\rho\frac{\left(\bar{X}_e + 1 - \rho\right)\bar{Y}_e}{\bar{R}_2^{\,5}}\right]\bar{x} - \left[(1-\rho)\left(\frac{1}{\bar{R}_1^{\,3}} - 3\frac{\bar{Y}_e^{\,2}}{\bar{R}_1^{\,5}}\right) + \rho\left(\frac{1}{\bar{R}_2^{\,3}} - 3\frac{\bar{Y}_e^{\,2}}{\bar{R}_2^{\,5}}\right)\right]\bar{y} \tag{2-20b}$$

$$\ddot{\bar{z}} = -\left[\frac{(1-\rho)}{\bar{R}_1^{\,3}} + \frac{\rho}{\bar{R}_2^{\,3}}\right]\bar{z} \tag{2-20c}$$

Note that linearization has decoupled the motion along the z axis from the motion along the x and y axes, implying that actuation along z is required for full 3 axis control.

Stability Analysis for the Earth-Moon Lagrange Points

The derivations and equations presented thus far are general in nature, and are valid for any three-body system. In this thesis, the focus is on the dynamics about the L4 point of the Earth-Moon system, where the value of ρ is approximately 0.012151, as previously noted. The analysis presented henceforth will make use of this mass ratio, with the results therefore being specific to the Earth-Moon system. The following linear stability analysis of the Earth-Moon Lagrange points is also described in [7].

Consider the L4 point of the Earth-Moon system where the co-ordinate of this point was previously found to be $\left(\rho - \frac{1}{2}, \frac{\sqrt{3}}{2}\right)$ and $\bar{R}_1 = \bar{R}_2 = 1$. Substituting this into Equations (2-20a,b) and expressing the resultant planar equations of motion in state space, we get the linearized equations of motion about the L4 point as

$$\begin{bmatrix} \dot{\bar{x}} \\ \dot{\bar{y}} \\ \ddot{\bar{x}} \\ \ddot{\bar{y}} \end{bmatrix} = \begin{bmatrix} 0 & 0 & 1 & 0 \\ 0 & 0 & 0 & 1 \\ \frac{3}{4} & \frac{3\sqrt{3}}{2}\left(\rho - \frac{1}{2}\right) & 0 & 2 \\ \frac{3\sqrt{3}}{2}\left(\rho - \frac{1}{2}\right) & \frac{9}{4} & -2 & 0 \end{bmatrix} \begin{bmatrix} \bar{x} \\ \bar{y} \\ \dot{\bar{x}} \\ \dot{\bar{y}} \end{bmatrix} \tag{2-21}$$

The characteristic equation for this system is

$$\lambda^4 + \lambda^2 + \left(\frac{27}{4}\right)\rho(1-\rho) = 0 \tag{2-22a}$$

This can be solved to find the eigenvalues,

$$\lambda = \pm\sqrt{\frac{-1 \pm \sqrt{1 - 27\rho(1-\rho)}}{2}} \tag{2-22b}$$

Note that the nature of the solutions to Equation (2-22) is dependent only on the mass ratio ρ, which is unique to a given system. So long as the mass ratio for a given system results in imaginary roots, motion about the triangular equilibrium points for that particular system would be bounded. For the solutions to be purely imaginary, the conditions $\rho \leq 0.03852$ or $\rho \geq 0.96148$ must be true. This condition is satisfied for both the Sun-Earth ($\rho = 3.0155 \times 10^{-6}$) and Earth-Moon ($\rho = 0.012151$) systems. Therefore, the four roots as given by Equation (2-22c) can be expressed as

$$\begin{aligned} \lambda_{1,2} &= 0 \pm is_1 \\ \lambda_{3,4} &= 0 \pm is_2 \end{aligned} \tag{2-22c}$$

where s_1 and s_2 are the imaginary parts. They also represent the long and short period frequencies of the bounded motions. Hence, natural motion about L4 point can be

conceptualized as being a superposition of the long and short period motions. In the Earth-Moon system, $s_1 \approx 0.297931$ and $s_2 \approx 0.954587$, resulting in a long period of 92 days and a short period of approximately 28.6 days, respectively.

The stability of the collinear points can be analyzed in a similar manner. Once again, substituting Equation (2-15a) into the non-dimensionalized equations of motion, and noting that $\overline{Y}_e$ and $\overline{Z}_e$ components are zero for the collinear case, after simplification, the equations become

$$\ddot{\overline{x}} - 2\dot{\overline{y}} - (2\sigma + 1)\overline{x} = 0 \tag{2-23a}$$

$$\ddot{\overline{y}} + 2\dot{\overline{x}} + (\sigma - 1)\overline{y} = 0 \tag{2-23b}$$

$$\ddot{\overline{z}} + \sigma\overline{z} = 0 \tag{2-23c}$$

where

$$\sigma = \frac{(1-\rho)}{\left|\overline{X}_e - \rho\right|^3} + \frac{\rho}{\left|\overline{X}_e + 1 - \rho\right|^3} \tag{2-24}$$

The characteristic equation in this case can be expressed as

$$\lambda^4 - (\sigma - 2)\lambda^2 - (2\sigma + 1)(\sigma - 1) = 0 \tag{2-25}$$

Substitution of values of σ for the Sun-Earth and Earth-Moon system and solving Equation (2-25) for the eigenvalues shows that there are two real and two imaginary roots in each case, indicating instability.

Closed Form Solutions

The in-plane Equations (2-21) are a set of linear, homogeneous differential equations. The general solution of these equations can be expressed as

$$\begin{aligned}\overline{x} &= c_1 e^{\lambda_1 t} + c_2 e^{\lambda_2 t} + c_3 e^{\lambda_3 t} + c_4 e^{\lambda_4 t} \\ \overline{y} &= c_1' e^{\lambda_1 t} + c_2' e^{\lambda_2 t} + c_3' e^{\lambda_3 t} + c_4' e^{\lambda_4 t}\end{aligned} \tag{2-26a}$$

where c_i and c_i' are constants, and t is time. This can be expanded using Euler's equation, $e^{i\theta} = \cos\theta + i\sin\theta$. Noting that for the Earth-Moon system the four in-plane eigenvalues are purely imaginary, substitution into equation (2-26a) gives [10]

$$\begin{aligned}\overline{x} &= C_1 \cos(s_1 t) + E_1 \sin(s_1 t) + C_2 \cos(s_2 t) + E_2 \sin(s_2 t) \\ \overline{y} &= C_1' \cos(s_1 t) + E_1' \sin(s_1 t) + C_2' \cos(s_2 t) + E_2' \sin(s_2 t)\end{aligned} \tag{2-26b}$$

where C_i, E_i, C_i', and E_i' are constants of the motion. The relation between C_i, E_i, C_i', E_i' as described in [10], is

$$C_i' = \kappa_i \left(2 s_i E_i - \frac{3\sqrt{3}}{2}\left(\rho - \frac{1}{2}\right) C_i \right) \tag{2-27a}$$

$$E_i' = -\kappa_i \left(2 s_i C_i + \frac{3\sqrt{3}}{2}\left(\rho - \frac{1}{2}\right) E_i \right) \tag{2-27b}$$

where

$$\kappa_i = \frac{1}{s_i^{\,2} + \frac{9}{4}} \tag{2-27c}$$

Furthermore, the relation between the initial states and the constants are [10]

$$\overline{x}_0 = C_1 + C_2 \qquad \overline{y}_0 = C_1' + C_2' \tag{2-28a}$$

$$\dot{\overline{x}}_0 = E_1 s_1 + E_2 s_2 \qquad \dot{\overline{y}}_0 = E_1' s_1 + E_2' s_2 \tag{2-28b}$$

From these relations, it can be readily seen that by setting the appropriate constants equal to zero, the long or short period could be eliminated from Equation (2-26).

The out-of-plane motion can be readily solved for as well. Substituting a trial solution of $\bar{z} = e^{\lambda t}$ into Equation (2-29a) and solving for λ, we find that $\lambda = \pm 1i$. This is a purely imaginary number, so the motion along the z axis is stable and, analogous to the in-plane motion, its frequency (s_z) is equal to 1 in this case. The general form of the solution therefore is

$$\bar{z} = J_1 \cos s_z t + J_2 \sin s_z t \tag{2-29a}$$

where J_i are constants of the motion. Letting the initial conditions in the z axis motion be $\bar{z}_0$ and $\dot{\bar{z}}_0$, solving for the constants and substitution into Equation (2-29a) yields

$$\bar{z} = \bar{z}_0 \cos s_z t + \frac{\dot{\bar{z}}_0}{s_z} \sin s_z t \tag{2-29b}$$

Two Periods of Motion

As determined previously, the two frequencies of motion are $s_1 \approx 0.297931$ and $s_2 \approx 0.954587$. Overall motion about the L4 point can be viewed as a superposition of these two frequencies, resulting in a complex trajectory path. The planar trajectory of an object about the L4 point is shown in Figure 2.3 and the out-of-plane motion is shown in Figure 2.4. Recall that in the derivation of the CR3BP model, the mass of the object is assumed to be insignificant compared to the two larger primaries and does not appear in the equations of motion. Thus, knowledge of an object's initial position and velocity is all that is required to determine its motion in this system. Figures 2.3 and 2.4 were generated using zero initial displacements from the L4 point and velocities of 10 m/s in all axes. Note that the ratio between the long and short period frequencies is irrational; this indicates that motion about the L4 point when both long and short periods are present is not closed. Instead, there is a recursion error in the motion as is clearly evidenced in Figure 2.3. Motion along the z axis is bounded and oscillatory. Although elegant, these

trajectories are too complex for preliminary spacecraft formation control development purposes and will not be considered further here.

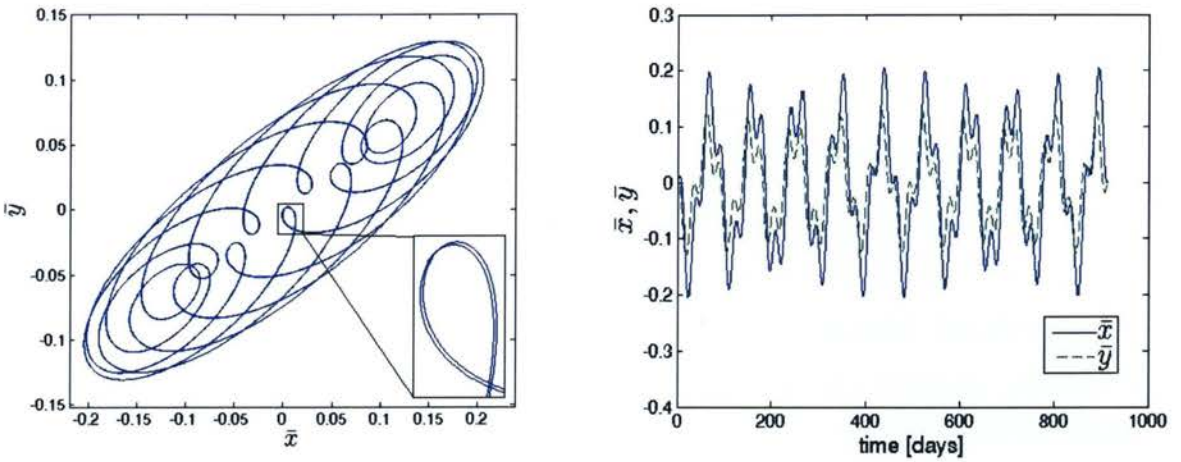

Figure 2.3 Planar trajectory when both the short and long period motions are present

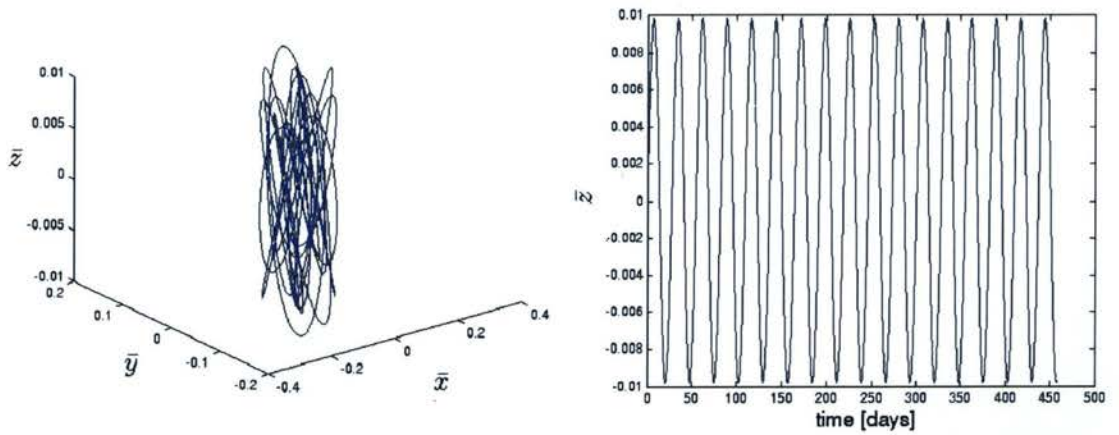

Figure 2.4 Out-of-plane motions when both the short and long period motions are present

Elimination of either the long or short period of motion is described in [10] and yields a more reasonable trajectory. In Equation (2-26a), to eliminate the long period of motion, the constants with subscripts '1' are set to zero. Equation (2-27) can then be used to solve for the constants in Equation (2-26b) and the initial conditions can be found from Equation (2-28). The same procedure can be done to eliminate the short period of motion. In that case, constants with subscript '2' are set to zero in Equation (2-26a) and

the above procedure is repeated. One only needs to input arbitrary initial states along the x axis when using this procedure. The long period is approximately 92 days (3 months) whereas the short period is approximately 28.6 days. For the plots of the short and long period trajectories shown in Figure 2.5 and Figure 2.6, the initial position and velocity along the x axis is set to zero and 10 m/s.

The trajectory of the leader satellite is assumed to be in a known reference orbit. In general, for a given mission, an appropriate closed trajectory for the leader satellite would need to be determined numerically based on anticipated initial epoch conditions, as was done in [40]. In that way, relative control could be achieved through control actuations on the follower satellite only. However, the focus of this study is to examine the plausibility of using various control strategies to accomplish relative control, and the numerical search for such closed trajectories is not within the scope of this present research. In this study, to facilitate the design of control laws and to assess the plausibility of different control schemes, it is assumed that the leader satellite is in a short period orbit about the L4 point. The short period is chosen since the Moon's orbital period of about 27.3 days is close to that of the short period. The control algorithms developed are general in nature and should be applicable for formations with alternate leader satellite trajectories.

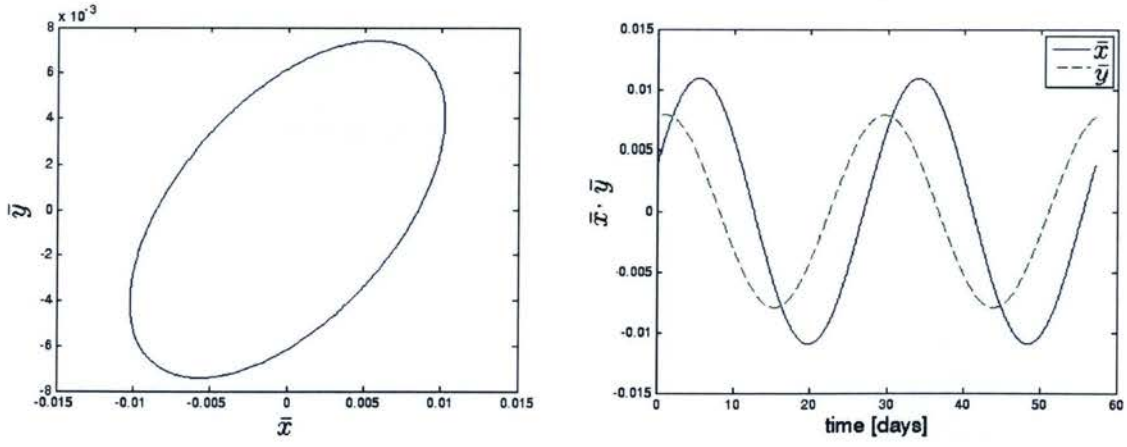

Figure 2.5 In-plane short period motion trajectory, period of ~28.6 days

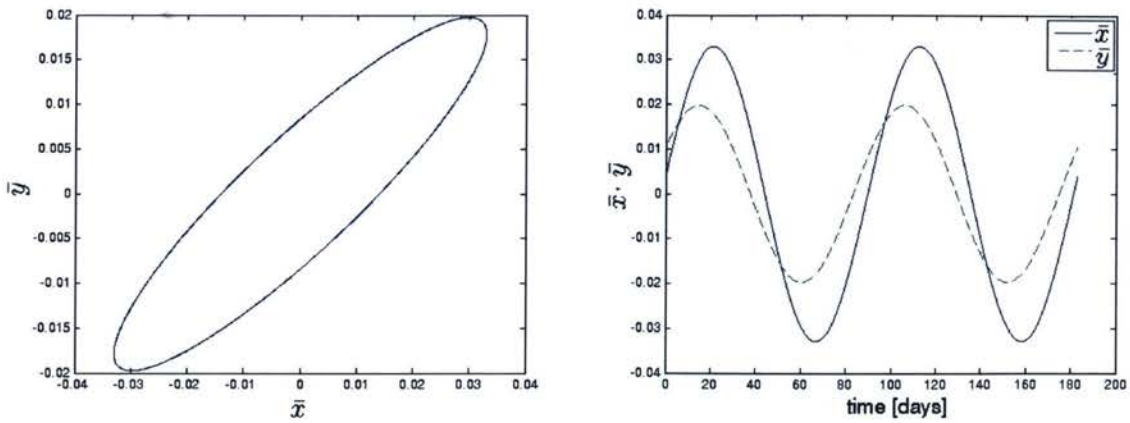

Figure 2.6 In-plane long period motion trajectory, period of ~92 days

2.6 Solar Gravitation Modelling

To model the Sun's perturbing force, the direction of the Sun needs to be expressed in the rotating frame of reference. This problem has been studied extensively by Tapley, Lewallen and Schutz [26-28], and by de Vries [21]. The Solar gravitation model presented here was first described in [26].

The gravitational potential of the Sun expressed in the rotating frame with origins at the Earth-Moon barycentre is

$$U_s = GM_3\left(\frac{1}{r_3} - \frac{X \cdot X_3 + Y \cdot Y_3 + Z \cdot Z_3}{D_3^{\,3}}\right) \tag{2-30}$$

where subscript '3' denotes values pertaining to the Sun. It can be shown that the Sun's perturbing force can be expressed in the rotating frame as

$$\frac{\partial U_s}{\partial X} = -\frac{GM_3}{r_3^{\,3}}(x - x_3) - \frac{GM_3}{D_3^{\,3}}(x_3 + X_e) \tag{2-31a}$$

$$\frac{\partial U_s}{\partial Y} = -\frac{GM_3}{r_3^{\,3}}(y - y_3) - \frac{GM_3}{D_3^{\,3}}(y_3 + Y_e) \tag{2-31b}$$

$$\frac{\partial U_s}{\partial Z} = -\frac{GM_3}{r_3^3}(z - z_3) - \frac{GM_3}{D_3^3} z_3 \tag{2-31c}$$

Note here that the transformations specified in Equations (2-15a,b,c) have been applied. The values of x_3, y_3, z_3 were found from a series of frame of reference rotations deduced from Figure 2.7, and can be expressed as

$$x_3 = D_3(\cos\psi\cos\theta + \cos i \sin\psi \sin\theta) - X_e \tag{2-32a}$$

$$y_3 = -D_3(\cos\psi\sin\theta - \cos i \sin\psi \sin\theta) - Y_e \tag{2-32b}$$

$$z_3 = D_3 \sin\psi \sin i \tag{2-32c}$$

where the inclination of the Earth-Moon orbit plane relative to the ecliptic is expressed as i here. The angle ψ is measured in the ecliptic and is the angular position of the Sun-Earth/Moon barycentre line. The angle θ is measured in the Earth-Moon orbit plane and represents the position of the Earth-Moon line. Both ψ and θ are measured relative to the Earth-Moon line of nodes and are functions of time, and are defined by

$$\psi = n_e t + \psi_0 \tag{2-33a}$$

$$\theta = nt + \theta_0 \tag{2-33b}$$

Here, n_e is the mean motion of the Earth-Moon barycentre about the Sun, which is equivalent to the angular rate of change of the Sun vector in the inertial frame. The angles ψ_0 and θ_0 are the initial angles. Equation (2-7) can be transformed into the L4 point centred frame of reference using Equation (2-15). Equation (2-31) can then be added to this result to form the solar-gravitationally-perturbed equations of motion.

$$\ddot{x}-2n\dot{y}-n^2\left(X_e+x\right)=-\frac{\mu_1(X_e+x-D_1)}{r_1^3}-\frac{\mu_2(X_e+x+D_2)}{r_2^3}-\frac{\mu_3\left(x-x_3\right)}{r_3^3}-\left(x_3+X_e\right)n_e^{\,2} \tag{2-34a}$$

$$\ddot{y}+2n\dot{x}-n^2\left(Y_e+y\right)=-\frac{\mu_1\left(Y_e+y\right)}{r_1^3}-\frac{\mu_2\left(Y_e+y\right)}{r_2^3}-\frac{\mu_3\left(y-y_3\right)}{r_3^3}-\left(y_3+Y_e\right)n_e^{\,2} \tag{2-34b}$$

$$\ddot{z}=-\frac{\mu_1 z}{r_1^3}-\frac{\mu_2 z}{r_2^3}-\frac{\mu_3\left(z-z_3\right)}{r_3^3}-z_3 n_e^{\,2} \tag{2-34c}$$

where the relations $n_e=\sqrt{\frac{GM_3}{D_3^{\,3}}}$ and $\mu_3=GM_3$ have been substituted. It should be noted that the problem is now more accurately described as a restricted four-body problem.

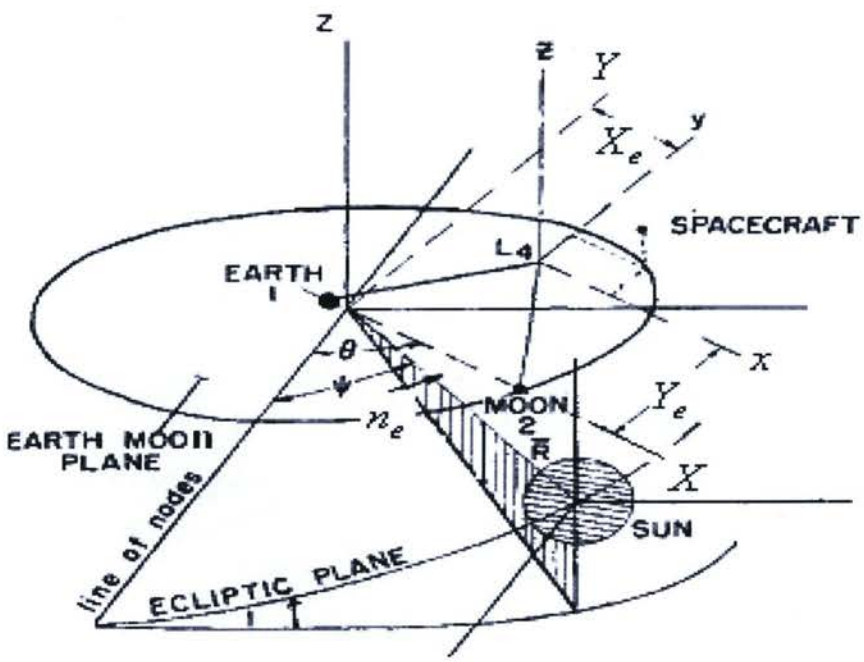

Figure 2.7 Illustration of the frames of references used to determine the Sun's direction vector [26]

Figure 2.8 and Figure 2.9 shows the effect of solar gravity on the motion of an object initially at rest at the L4 point over the course of 700 days. These results match those presented in [26-28]. It can be seen that the in-plane motion grows dramatically over this period, with the widest part of its trajectory being over 500,000 km. The motion also appears to begin contracting, as evidenced by the plots of the axial motions. However, practical applications that require or can tolerate such large deviations from the equilibrium point are rarely discussed. As such, even if the motion of the object is theoretically bounded, it is not considered stable enough for practical applications and control would still be necessary in order to restrict the object's motion to stay within useful regions only. The Sun's direction vector has a component in the out of plane direction as a result of the inclination of the Earth-Moon orbital plane relative to the ecliptic, which in turn perturbs motion along the z axis.

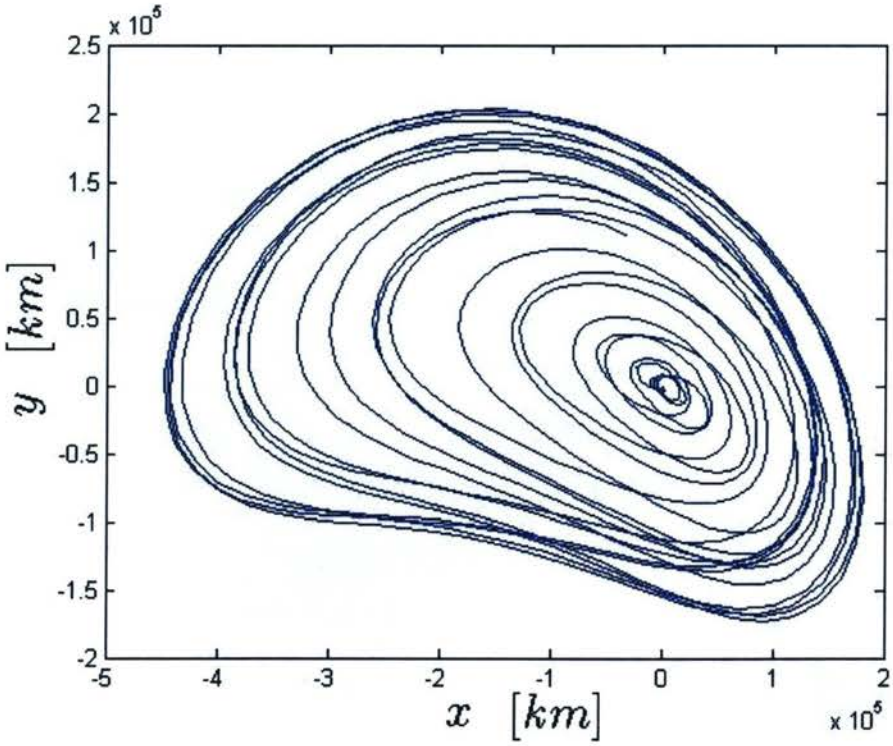

Figure 2.8 Trajectory of an object initially at rest at the L4 point under the influence of the Sun over the course of 700 days.

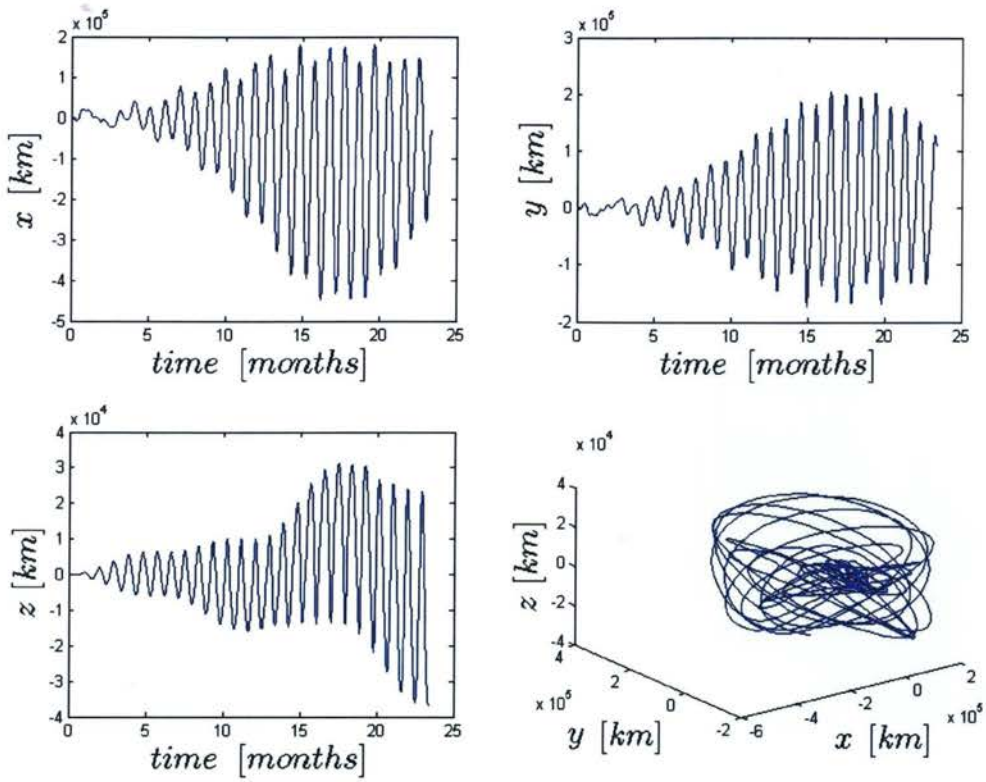

Figure 2.9 Motion along each axis of an object initially at rest at the L4 point, perturbed by the Sun over a period of 700 days

Solar Gravitation Model Limitations

The simplified model of Solar gravitation discussed previously requires some cautionary notes. In this restricted four-body system, only the motion of the satellite is assumed to be perturbed by the Sun's gravity. However, it is well known that that Sun also perturbs the motion of the Moon, which is unaccounted for in this model.

Limitations must also be placed on simulation time frames. Aside from cumulative numerical integration errors, this model assumes that the primary bodies are point masses and also does not accurately account for an object's motion when it is very close to either the Earth or the Moon. As a result, long term simulation results are rendered meaningless. To demonstrate this, suppose the simulations shown in Figures 2.8 and 2.9 are repeated with a time frame of 1000 months. These results are shown in Figure 2.10. The immediate assumption would be that the motion of an object placed into this system would remain bounded, with continual expanding and contracting trends. However,

numerical studies done in [37] and [38] show that the object would cross paths with either the Earth or Moon or experience close lunar encounters within several months, which leads to its ejection from the Earth-Moon system. Thus, long term analytical simulations using this model should be viewed critically in light of the results of these numerical studies.

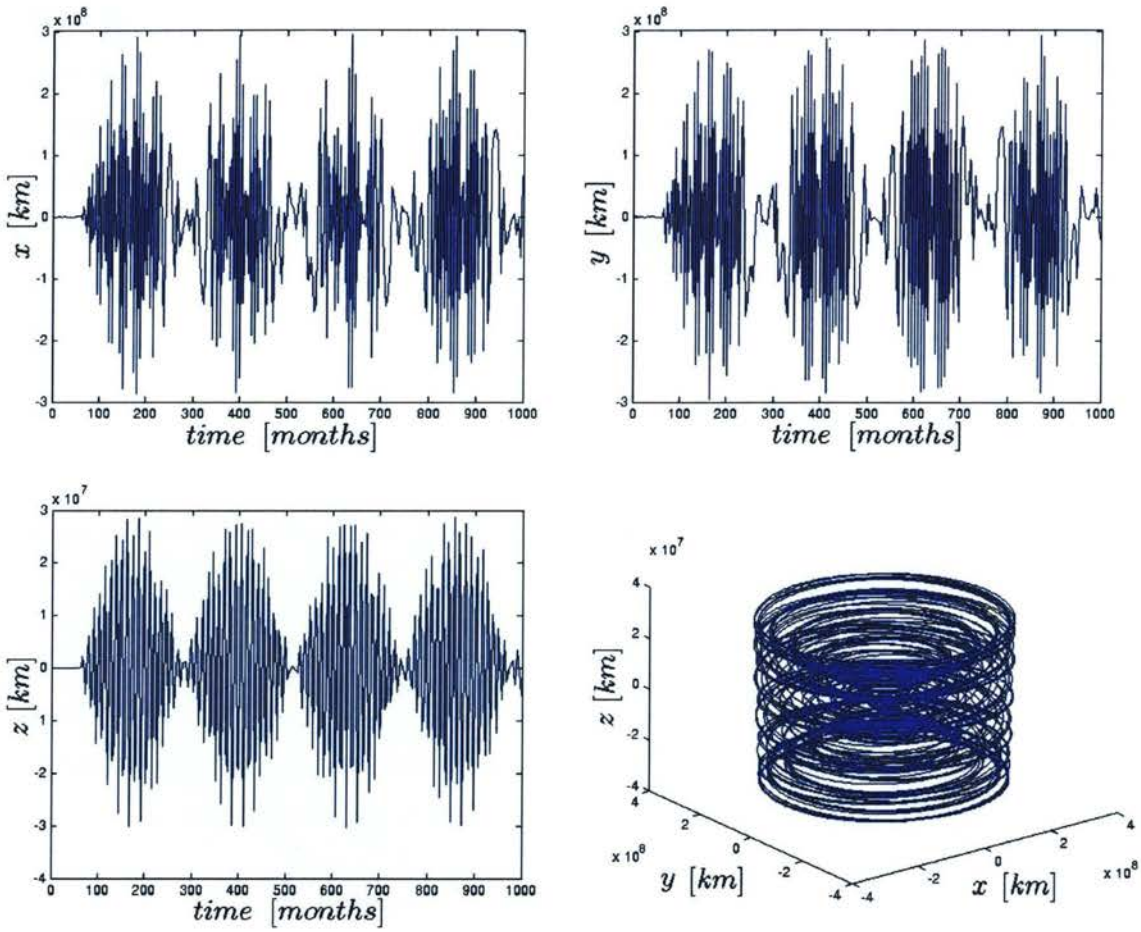

Figure 2.10 Long term simulation results showing bounded motions under Solar gravitational perturbations

2.7 Solar Radiation Influence

In addition to solar gravitation, solar radiation pressure (SRP) is also a source of disturbance. The magnitude of acceleration caused by SRP is typically small; often times, on the order of ~10^{-6} N or less. However, the degree to which this acceleration can

affect the motion of a system is also largely dependent on the ratio of surface area exposed to the Sun to the mass of the object. In this study, an attempt to exploit SRP in order to control the relative motion of two satellites is made. Recently, the study of reconfiguration at one of the collinear libration points was completed in [49]. Modelling of SRP can be found in more detail in [51] and [52 - 54]. This section provides a brief overview of the SRP model used in this study, which is similar to that used in [49].

Solar radiation pressure force can be expressed as the sum of three components: force due to specular reflection, F_{rs}, diffuse reflection, F_{rd}, and absorption, F_a. These three components can be expressed by the following set of equations.

$$\mathbf{F}_{rs} = 2\rho_{rs} P A_s (\hat{\mathbf{N}} \cdot \hat{\mathbf{L}})^2 \hat{\mathbf{N}} \tag{2-35a}$$

$$\mathbf{F}_{rd} = \rho_{rd} P A_s (\hat{\mathbf{N}} \cdot \hat{\mathbf{L}})(\hat{\mathbf{L}} + 2\hat{\mathbf{N}}/3) \tag{2-35b}$$

$$\mathbf{F}_a = \rho_a P A_s (\hat{\mathbf{N}} \cdot \hat{\mathbf{L}})\hat{\mathbf{L}} \tag{2-35c}$$

where ρ_{rs}, ρ_{rd} and ρ_a above are the solar specular, diffuse and absorption coefficients, the sum of which is equal to 1. $\hat{\mathbf{N}}$ is the unit vector normal to the illuminated surface, $\hat{\mathbf{L}}$ is the unit vector in the direction of incoming solar radiation, A_s is the exposed effective area and P is the mean flux, which is approximately equal to 4.5×10^{-6} N/m^2 in the region this study concerns. If it is assumed that an ideal reflective surface is used, then ρ_{rd} and ρ_d would be equal to zero, leaving only Equation (2-35a). Noting that $\mathbf{F}_{rs} = m\mathbf{a}_{srp}$, then the acceleration due to SRP can be expressed as

$$\mathbf{a}_{srp} = 2P(A_s/m)\cos^2\gamma\hat{\mathbf{N}} = a_{\max}\cos^2\gamma\hat{\mathbf{N}} \tag{2-36}$$

where γ is the angle between $\hat{\mathbf{N}}$ and $\hat{\mathbf{L}}$ and $a_{\max} = 2P(A/m)$ is the maximum acceleration due to SRP.

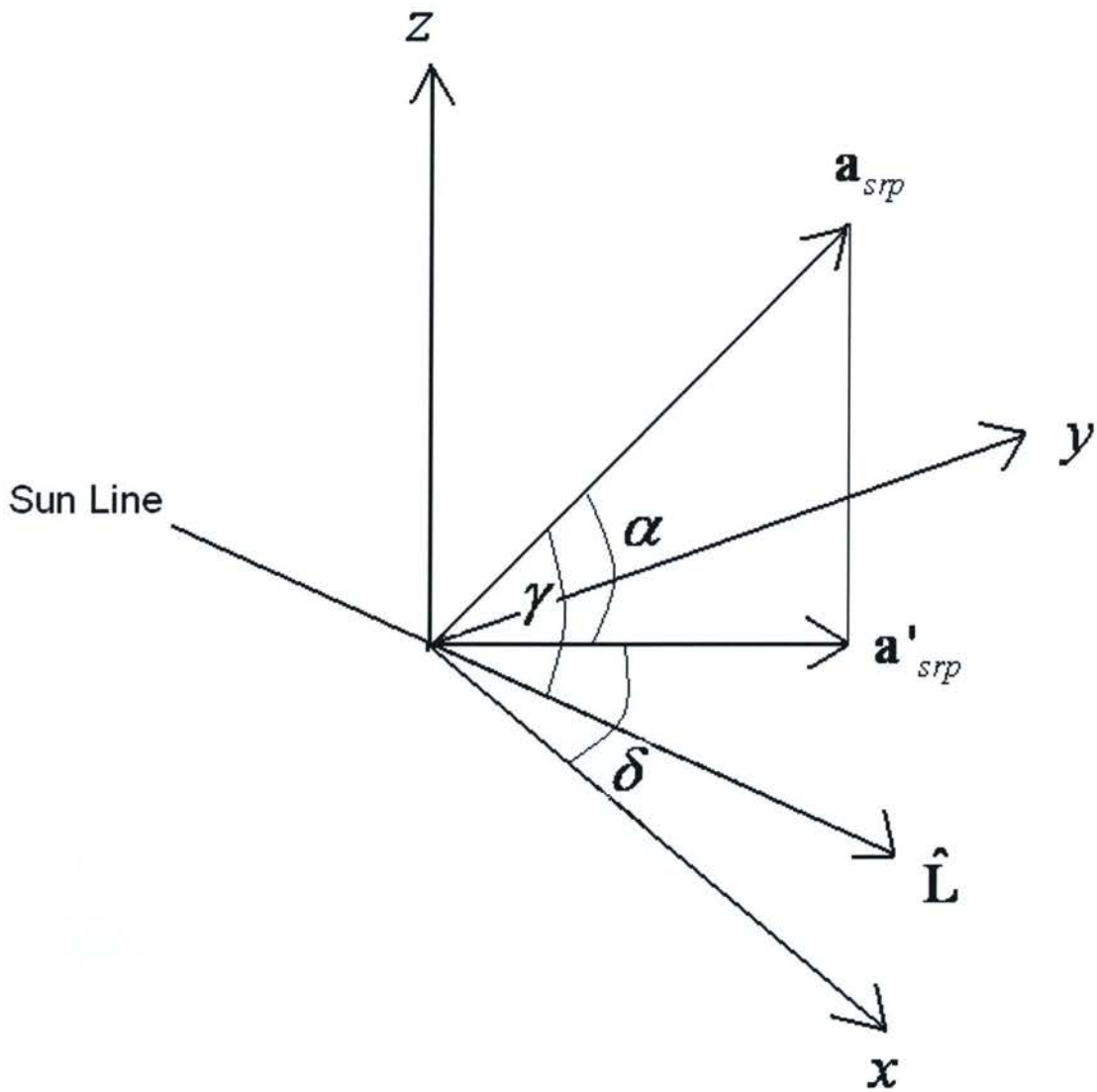

Figure 2.11 Frame of reference used to determine $\mathbf{a}_{srp}$ expressions

Referring to Figure 2.11, the $\mathbf{a}_{srp}$ vector can be expressed as a function of two angles α and δ, which are the angles between $\mathbf{a}_{srp}$ and the $x-y$ plane and it's projection $\mathbf{a}'_{srp}$ and the x axis. Note that α and γ are not necessarily equal since $\hat{\mathbf{L}}$ is not restricted to act only in the $x-y$ plane. The projection $\mathbf{a}'_{srp}$ can be expressed as

$$\mathbf{a}'_{srp} = a_{srp} \cos\alpha \tag{2-37}$$

where a_{srp} is the magnitude of vector $\mathbf{a}_{srp}$. The $\mathbf{a}_{srp}$ vector can then be described as follows after substitution

$$\mathbf{a}_{srp} = a_{srp}\cos\alpha\cos\delta\hat{\mathbf{x}} + a_{srp}\cos\alpha\sin\delta\hat{\mathbf{y}} + a_{srp}\sin\alpha\hat{\mathbf{z}} \tag{2-38}$$

From Equation (2-36), it can be seen that $a_{srp} = 2P(A_s/m)\cos^2\gamma$. Substitution of this into (2-38) gives

$$a_x = a_{\max}\cos^2\gamma\cos\alpha\cos\delta \tag{2-39a}$$

$$a_y = a_{\max}\cos^2\gamma\cos\alpha\sin\delta \tag{2-39b}$$

$$a_z = a_{\max}\cos^2\gamma\sin\alpha \tag{2-39c}$$

from which $\hat{\mathbf{N}} = [\cos\alpha\cos\delta \quad \cos\alpha\sin\delta \quad \sin\alpha]^T$ can be deduced.

2.8 Formation-Flying Pair of Spacecraft

The equations of motion developed thus far represent the motion of an object in the vicinity of the L4 point. For formation flying studies, it is convenient to work with the relative equations of motion between two satellites. In this section, the relative equations will be developed.

Relative Equations of Motion

The nonlinear relative equations of motion can be determined by differencing the equations of motion for each satellite in a formation relative to the leader. In this study, a formation-flying pair of spacecraft will be considered. This technique can be extended to a formation with an arbitrary number of spacecraft in different configurations. Equations (2-34a,b,c) are rewritten here for each satellite.

$$\ddot{x}_i - 2n\dot{y}_i - n^2\left(X_e + x_i\right) = -\frac{\mu_1(X_e + x_i - D_1)}{r_{1i}^{\ 3}} - \frac{\mu_2(X_e + x_i + D_2)}{r_{2i}^{\ 3}} - \frac{\mu_3\left(x_i - x_3\right)}{r_{3i}^{\ 3}} - \left(x_3 + X_e\right)n_e^{\ 2} \tag{2-40a}$$

$$\ddot{y}_i + 2n\dot{x}_i - n^2\left(Y_e + y_i\right) = -\frac{\mu_1\left(Y_e + y_i\right)}{r_{1i}^{\ 3}} - \frac{\mu_2\left(Y_e + y_i\right)}{r_{2i}^{\ 3}} - \frac{\mu_3\left(y_i - y_3\right)}{r_{3i}^{\ 3}} - \left(y_3 + Y_e\right)n_e^{\ 2} \tag{2-40b}$$

$$\ddot{z}_i = -\frac{\mu_1 z_i}{r_{1i}^{\ 3}} - \frac{\mu_2 z_i}{r_{2i}^{\ 3}} - \frac{\mu_3\left(z_i - z_3\right)}{r_{3i}^{\ 3}} - z_3 n_e^{\ 2} \tag{2-40c}$$

Subscript $i = F, L$ here, and represents the follower and leader satellite, respectively. Subtracting the leader satellite's motion from the follower gives

$$\ddot{x}_r = 2n\dot{y}_r + x_r n^2 + \mu_1\left(\frac{\left(x_1 - x_F\right)}{r_{1F}^{\ 3}} - \frac{(x_1 - x_L)}{r_{1L}^{\ 3}}\right) + \mu_2\left(\frac{\left(x_2 - x_F\right)}{r_{2F}^{\ 3}} - \frac{(x_2 - x_L)}{r_{2L}^{\ 3}}\right) + \mu_3\left(\frac{\left(x_3 - x_F\right)}{r_{3F}^{\ 3}} - \frac{\left(x_3 - x_L\right)}{r_{3L}^{\ 3}}\right) \tag{2-41a}$$

$$\ddot{y}_r = -2n\dot{x}_r + y_r n^2 + \mu_1\left(\frac{\left(y_1 - y_F\right)}{r_{1F}^{\ 3}} - \frac{(y_1 - y_L)}{r_{1L}^{\ 3}}\right) + \mu_2\left(\frac{\left(y_2 - y_F\right)}{r_{2F}^{\ 3}} - \frac{(y_2 - y_L)}{r_{2L}^{\ 3}}\right) + \mu_3\left(\frac{\left(y_3 - y_F\right)}{r_{3F}^{\ 3}} - \frac{\left(y_3 - y_L\right)}{r_{3L}^{\ 3}}\right) \tag{2-41b}$$

$$\ddot{z}_r = \mu_1\left(\frac{-z_F}{r_{1F}^{\ 3}} + \frac{z_L}{r_{1L}^{\ 3}}\right) + \mu_2\left(\frac{-z_F}{r_{2F}^{\ 3}} + \frac{z_L}{r_{2L}^{\ 3}}\right) + \mu_3\left(\frac{-\left(z_F - z_3\right)}{r_{3F}^{\ 3}} + \frac{\left(z_L - z_3\right)}{r_{3L}^{\ 3}}\right) \tag{2-41c}$$

where the relations $x_1 = -\left(X_e - D_1\right)$, $x_2 = -\left(X_e + D_2\right)$ and $y_1 = y_2 = -Y_e$ have been substituted to simplify the equations and subscript 'r' refers to relative motion. The motion of the follower satellite relative to the leader is given in Equations (2-41a,b,c), which are functions of the leader, follower and relative states. The relations $x_F = x_L + x_r$, $y_F = y_L + y_r$ and $z_F = z_L + z_r$ can be substituted in order to express the

relative motion as functions of the relative and leader satellite's states only. When this substitution is made, Equation (2-41) can be expressed as follows after some simplification:

$$\begin{aligned}\ddot{x}_r = 2n\dot{y}_r + x_r n^2 &+ \mu_1\left(-\frac{x_r}{r_{1F}^{\ 3}} + (x_1 - x_L)\left(\frac{1}{r_{1F}^{\ 3}} - \frac{1}{r_{1L}^{\ 3}}\right)\right) \\ &+ \mu_2\left(-\frac{x_r}{r_{2F}^{\ 3}} + (x_2 - x_L)\left(\frac{1}{r_{2F}^{\ 3}} - \frac{1}{r_{2L}^{\ 3}}\right)\right) \\ &+ \mu_3\left(-\frac{x_r}{r_{3F}^{\ 3}} + (x_3 - x_L)\left(\frac{1}{r_{3F}^{\ 3}} - \frac{1}{r_{3L}^{\ 3}}\right)\right)\end{aligned} \tag{2-42a}$$

$$\begin{aligned}\ddot{y}_r = -2n\dot{x}_r + y_r n^2 &+ \mu_1\left(-\frac{y_r}{r_{1F}^{\ 3}} + (y_1 - y_L)\left(\frac{1}{r_{1F}^{\ 3}} - \frac{1}{r_{1L}^{\ 3}}\right)\right) \\ &+ \mu_2\left(-\frac{y_r}{r_{2F}^{\ 3}} + (y_2 - y_L)\left(\frac{1}{r_{2F}^{\ 3}} - \frac{1}{r_{2L}^{\ 3}}\right)\right) \\ &+ \mu_3\left(-\frac{y_r}{r_{3F}^{\ 3}} + (y_3 - y_L)\left(\frac{1}{r_{3F}^{\ 3}} - \frac{1}{r_{3L}^{\ 3}}\right)\right)\end{aligned} \tag{2-42b}$$

$$\begin{aligned}\ddot{z}_r = \mu_1\left(\frac{-z_r}{r_{1F}^{\ 3}} - z_L\left(\frac{1}{r_{1F}^{\ 3}} - \frac{1}{r_{1L}^{\ 3}}\right)\right) + \mu_2\left(-\frac{z_r}{r_{2F}^{\ 3}} - z_L\left(\frac{1}{r_{2F}^{\ 3}} - \frac{1}{r_{2L}^{\ 3}}\right)\right) \\ + \mu_3\left(-\frac{z_r}{r_{3F}^{\ 3}} - (z_L - z_3)\left(\frac{1}{r_{3F}^{\ 3}} - \frac{1}{r_{3L}^{\ 3}}\right)\right)\end{aligned} \tag{2-42c}$$

where the distances from the leader and follower to the primary bodies are

$$r_{1L} = \sqrt{(x_L - x_1)^2 + (y_L - y_1)^2 + (z_L)^2} \tag{2-43a}$$

$$r_{2L} = \sqrt{(x_L - x_2)^2 + (y_L - y_2)^2 + z_L^{\ 2}} \tag{2-43b}$$

$$r_{3L} = \sqrt{(x_L - x_3)^2 + (y_L - y_3)^2 + (z_L - z_3)^2} \tag{2-43c}$$

$$r_{1F} = \sqrt{((x_L + x_r) - x_1)^2 + ((y_L + y_r) - y_1)^2 + (z_L + z_r)^2} \tag{2-43d}$$

$$r_{2F} = \sqrt{((x_L + x_r) - x_2)^2 + ((y_L + y_r) - y_2)^2 + (z_L + z_r)^2} \tag{2-43e}$$

$$r_{3F} = \sqrt{\left((x_L + x_r) - x_3\right)^2 + \left((y_L + y_r) - y_3\right)^2 + \left((z_L + z_r) - z_3\right)^2} \tag{2-43f}$$

Figure 2.12 illustrates the various vector quantities in the relative equations of motion.

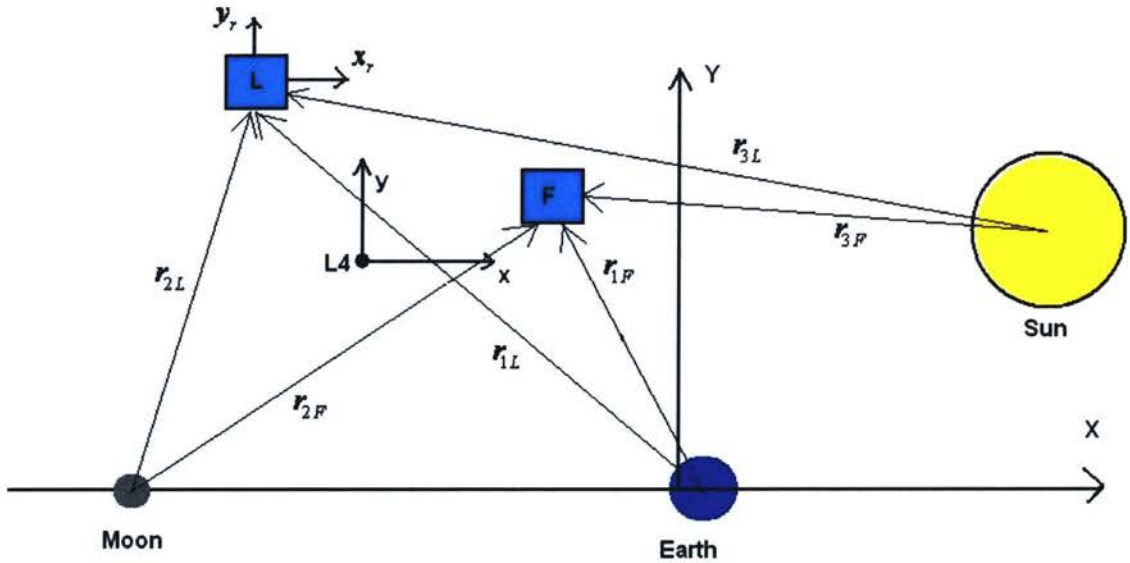

Figure 2.12 Schematic showing the vector quantities required in the relative equations of motion

Linearized Relative Equations

The linearized equations of relative motion are derived in much the same way as Equations (2-42a,b,c) were derived. Rewriting Equation (2-21) for the follower and leader satellites and differencing, we find the linearized relative equations of motion to be

$$\ddot{\bar{x}}_r = 2\dot{\bar{y}}_r + \frac{3}{4}\bar{x}_r + \frac{3\sqrt{3}}{2}\left(\rho - \frac{1}{2}\right)\bar{y}_r \tag{2-44a}$$

$$\ddot{\bar{y}}_r = -2\dot{\bar{x}}_r + \frac{3\sqrt{3}}{2}\left(\rho - \frac{1}{2}\right)\bar{x}_r + \frac{9}{4}\bar{y}_r \tag{2-44b}$$

$$\ddot{\bar{z}}_r = -\bar{z}_r \tag{2-44c}$$

These equations are of the same form as the linearized equations for a single satellite's motion without the Sun's gravitational influence. Since the Sun's gravity will be treated

as a disturbance to the system, it is not necessary to linearize its effects. The relative Solar gravitational effect can be extracted from Equation (2-42), expressed in non-dimensional form and added to Equation (2-44) to form

$$\begin{aligned}\ddot{\bar{x}}_r &= 2\dot{\bar{y}}_r + \frac{3}{4}\bar{x}_r + \frac{3\sqrt{3}}{2}\left(\rho - \frac{1}{2}\right)\bar{y}_r \\ &\quad + \rho'\rho\left(-\frac{\bar{x}_r}{\bar{r}_{3F}^{\,3}} + (\bar{x}_3 - \bar{x}_L)\left(\frac{1}{\bar{r}_{3F}^{\,3}} - \frac{1}{\bar{r}_{3L}^{\,3}}\right)\right)\end{aligned} \tag{2-45a}$$

$$\begin{aligned}\ddot{\bar{y}}_r &= -2\dot{\bar{x}}_r + \frac{3\sqrt{3}}{2}\left(\rho - \frac{1}{2}\right)\bar{x}_r + \frac{9}{4}\bar{y}_r \\ &\quad + \rho'\rho\left(-\frac{\bar{y}_r}{\bar{r}_{3F}^{\,3}} + (\bar{y}_3 - \bar{y}_L)\left(\frac{1}{\bar{r}_{3F}^{\,3}} - \frac{1}{\bar{r}_{3L}^{\,3}}\right)\right)\end{aligned} \tag{2-45b}$$

$$\ddot{\bar{z}}_r = -\bar{z}_r + \rho'\rho\left(-\frac{\bar{z}_r}{\bar{r}_{3F}^{\,3}} - (\bar{z}_L - \bar{z}_3)\left(\frac{1}{\bar{r}_{3F}^{\,3}} - \frac{1}{\bar{r}_{3L}^{\,3}}\right)\right) \tag{2-45c}$$

where $\rho' = 2.7066\times10^7$ is the Sun-Moon mass ratio.

Relative Reference Trajectory

The unperturbed linearized equations of relative motion have the same form as that for a single satellite. Its closed form solution can be shown as

$$\begin{aligned}\bar{x}_r &= (C_{1F} - C_{1L})\cos(s_1 t) + (E_{1F} - E_{1L})\sin(s_1 t) \\ &\quad + (C_{2F} - C_{2L})\cos(s_2 t) + (E_{2F} - E_{2L})\sin(s_2 t)\end{aligned} \tag{2-46a}$$

$$\begin{aligned}\bar{y}_r &= (C'_{1F} - C'_{1L})\cos(s_1 t) + (E'_{1F} - E'_{1L})\sin(s_1 t) \\ &\quad + (C'_{2F} - C'_{2L})\cos(s_2 t) + (E'_{2F} - E'_{2L})\sin(s_2 t)\end{aligned} \tag{2-46b}$$

$$\bar{z}_r = (\bar{z}_{0F} - \bar{z}_{0L})\cos s_z t + \frac{(\dot{\bar{z}}_{0F} - \dot{\bar{z}}_{0L})}{s_z}\sin s_z t \tag{2-46c}$$

The leader satellite reference motion's period was selected be equal to that of the short period. Extending this requirement to that of the relative reference trajectory would

imply that the constants $C_{1F} = C_{1L} = E_{1F} = E_{1L} = 0$ and $C'_{1F} = C'_{1L} = E'_{1F} = E'_{1L} = 0$. For a planar reference trajectory, the relative z axis positions and velocities are set equal to zero as well. With these requirements, the reference relative motion can be expressed as

$$\overline{x}_r = \overline{x}_{0r}\cos(s_2 t) + \frac{\dot{\overline{x}}_{0r}}{s_2}\sin(s_2 t) \tag{2-47a}$$

$$\overline{y}_r = \overline{y}_{0r}\cos(s_2 t) + \frac{\dot{\overline{y}}_{0r}}{s_2}\sin(s_2 t) \tag{2-47b}$$

$$\overline{z}_r = 0 \tag{2-47c}$$

where Equation (2-28) was substituted to express the equations as functions of the initial relative conditions.

Chapter 3

Design of Control Algorithms

3.1 Introduction

In this study, attempts are made to achieve formation-keeping control in the fully actuated and underactuated system configurations. A fully actuated system is one in which the number of control inputs is equal to the degrees of freedom (DoF) of the system. An underactuated system will have fewer control inputs than its DoF. In this chapter, the design of controllers for the fully actuated system and the underactuated system is presented. Controllers are developed for the system controlled by thrusters, solar sails and a combination of those two referred to as a hybrid system. It is assumed that all states are measureable, no sensor noise is present and that the leader satellite is in the reference orbit described in Chapter 2 so that relative control is applied only to the follower. First, a linear controller using Linear Quadratic Regulator (LQR) control is developed for a linear, time invariant system (LTI). This is followed by an overview of sliding mode control (SMC), and the development of sliding mode controllers for the fully actuated and underactuated systems. Finally, a bang-bang controller will be developed for the underactuated system.

3.2 Linear Control Method (LQR)

LQR control method was applied to every scenario investigated in this thesis. A brief summary of the LQR control scheme is provided in [55] and summarized here, followed by the development of linear control laws for the fully actuated and underactuated spacecraft-formation system.

3.2.1 The Linear Quadratic Regulator

For a linear time invariant system expressed as

$$\dot{x} = Ax + Bu \tag{3-1}$$

where x represents the system states, A is the state matrix and B the control input matrix, LQR can be used to find an optimal control law for this system. The goal is to find control inputs that will minimize the cost function, J over some time interval $t_0 \le t \le t_1$.

$$J = \int_{t_0}^{t_1} (x^T Q x + u^T R u) dt \tag{3-2}$$

Here, Q and R are square and symmetric weighting matrices; Q and R respectively weigh the tracking error and the magnitude of the control input. The control input, u, can be found as

$$u = -Kx \tag{3-3}$$

where

$$K = R^{-1} B^T H \tag{3-4}$$

and matrix H is found by solving the matrix Riccati Equations,

$$\dot{H} = -HA - A^T H - Q + HBR^{-1} B^T H \tag{3-5}$$

If the time t_1 approaches infinity or is sufficiently far removed from time t_0, it can be shown that Equation (3-5) reduces to

$$HA + A^T H + Q - HBR^{-1}B^T H = 0 \tag{3-6}$$

and H becomes constant.

3.2.2 LQR Control of the Thruster-Controlled System

Linear control methods can be developed provided the linearized formation system is controllable. The controllability matrix of the linearized, unperturbed system described in Chapter 2 is first confirmed to be of full rank. LQR control can then be applied to the linear system to find the constant control parameters.

Controllability of the System

A linear time invariant system is said to be controllable if a control input u is able to bring a system from an initial state $x(t_0)$ to some defined desired state $x(t_d)$ within a finite amount of time. It is well known that for the $n \times n$ state matrix A, the matrix formed by

$$M = \left[B : AB : \ldots : A^{n-1}B \right]^T \tag{3-7}$$

is known as the controllability matrix. If M is of full rank (rank n), then the system is said to be controllable. Checking the controllability of the unperturbed system, it can be confirmed that the system is of full rank and therefore controllable.

LQR Control using Thrusters

From the overview of the LQR method, it is seen that the state and control weighting matrices Q and R are selected based on the state and control input responses. From these, the gain matrix K is determined through solving the Ricatti Equation. In the case of using thrusters for the control input, the control matrix B is constant and the control input

u represent relative accelerations along the corresponding axes. As will be shown in Chapter 4, it appears that only an electric propulsion system is currently capable of imparting the minute accelerations required for formation control. For the fully actuated system, letting I represent the identity matrix, the matrices' dimensions are $Q \in \mathbb{R}^{6\times6}$, $R \in \mathbb{R}^{3\times3}$ and $B = \begin{bmatrix} 0_{3\times3} & I_{3\times3} \end{bmatrix}^T$.

For the case of the underactuated scenario, the dimensions were $Q \in \mathbb{R}^{6\times6}$, $R \in \mathbb{R}^{2\times2}$ and $B = \begin{bmatrix} 0_{4\times2} & I_{2\times2} \end{bmatrix}^T$.

Solving for the gain matrix, the control input can then be specified by

$$u = -K\tilde{x} \tag{3-8}$$

where $\tilde{x}$ is the state error vector. Note that K is determined using linear plant dynamics while u is the control input for the nonlinear plant model. Q and R are determined through trial and error until reasonable system responses are obtained.

3.2.3 LQR Control of the Solar Sail Controlled System

In many cases, linearized system models provide good approximations of a nonlinear system's motion, provided system states remain within the realm where linear approximations are valid. It is therefore reasonable to hypothesize that a linear controller may be able to stabilize a nonlinear system to within tolerable error ranges. However, since the SRP control input function is nonaffine in the input u, and the LQR method requires the system dynamics to be expressible in the form of Equation (3-1), some simplifications to the SRP model will be necessary. Using small angle approximations the expressions for SRP can be simplified. These approximations will allow the system to be expressed in the appropriate form so that the LQR control development scheme outlined previously can be followed.

Angle Approximations

The SRP model used in this study for a single satellite was previously given in Chapter 2 and is reproduced here for convenience.

$$
\begin{aligned}
a_x &= a_{\max} \cos^2 \gamma \cos\alpha \cos\delta \\
a_y &= a_{\max} \cos^2 \gamma \cos\alpha \sin\delta \\
a_z &= a_{\max} \cos^2 \gamma \sin\alpha
\end{aligned}
\tag{3-9}
$$

By differencing the SRP acceleration effect on each satellite, the relative SRP acceleration can be found as

$$
\begin{aligned}
a_{xr} &= a_{\max}\left(\cos^2 \gamma_F \cos\alpha_F \cos\delta_F - \cos^2 \gamma_L \cos\alpha_L \cos\delta_L\right) \\
a_{yr} &= a_{\max}\left(\cos^2 \gamma_F \cos\alpha_F \sin\delta_F - \cos^2 \gamma_L \cos\alpha_L \sin\delta_L\right) \\
a_{zr} &= a_{\max}\left(\cos^2 \gamma_F \sin\alpha_F - \cos^2 \gamma_L \sin\alpha_L\right)
\end{aligned}
\tag{3-10}
$$

where subscripts F, L denote the leader and follower satellites, r represents relative motion. If it is assumed that the solar sails on the follower and leader satellite are oriented in a symmetric fashion, then $\gamma_F \approx \gamma_L$. It can then be seen that $\cos^2 \gamma_F = \cos^2 \gamma_L = \cos^2 \gamma$. Equation (3-10) can then be expressed as

$$
\begin{aligned}
a_{xr} &= a_{\max} \cos^2 \gamma\left(\cos\alpha_F \cos\delta_F - \cos\alpha_L \cos\delta_L\right) \\
a_{yr} &= a_{\max} \cos^2 \gamma\left(\cos\alpha_F \sin\delta_F - \cos\alpha_L \sin\delta_L\right) \\
a_{zr} &= a_{\max} \cos^2 \gamma\left(\sin\alpha_F - \sin\alpha_L\right)
\end{aligned}
\tag{3-11}
$$

If $\delta_{F,L}$ and $\alpha_{F,L}$ are restricted to be small angles, then $\cos\alpha_{F,L} \approx 1$, $\cos\delta_{F,L} \approx 1$, $\sin\delta_{F,L} \approx \delta_{F,L}$ and $\sin\alpha_{F,L} \approx \alpha_{F,L}$. With these simplifications, the SRP model can be expressed as

$$
\begin{aligned}
a_{xr} &\approx 0 \\
a_{yr} &\approx a_{\max} \cos^2 \gamma \cdot \delta_r \\
a_{zr} &\approx a_{\max} \cos^2 \gamma \cdot \alpha_r
\end{aligned}
\tag{3-12}
$$

From these simplified expressions, it can be clearly seen that the relative input angles δ_r and α_r are now simply products of the control matrix, and hence easily extractible to form the linear system described by Equation (3-1). For the formation system described in this thesis, the A, B, x and u matrix are expressed as

$$
\begin{aligned}
A &= \begin{bmatrix} 0 & 0 & 0 & 1 & 0 & 0 \\ 0 & 0 & 0 & 0 & 1 & 0 \\ 0 & 0 & 0 & 0 & 0 & 1 \\ \frac{3}{4} & C & 0 & 0 & 2 & 0 \\ C & \frac{9}{4} & 0 & -2 & 0 & 0 \\ 0 & 0 & -1 & 0 & 0 & 0 \end{bmatrix}, \qquad x = \begin{bmatrix} x_r \\ y_r \\ z_r \\ \dot{x}_r \\ \dot{y}_r \\ \dot{z}_r \end{bmatrix} \\
B &= a_{\max} \cos^2 \gamma \cdot \begin{bmatrix} 0 & 0 & 0 & 0 & 1 & 0 \\ 0 & 0 & 0 & 0 & 0 & 1 \end{bmatrix}, \qquad u = \begin{bmatrix} \delta_r \\ \alpha_r \end{bmatrix}
\end{aligned}
\tag{3-13}
$$

The constant C equals $\frac{3\sqrt{3}}{2}\left(\rho - \frac{1}{2}\right)$ here. The relation between $\delta_{F,L}$ and $\alpha_{F,L}$ can be expressed as

$$
\begin{aligned}
\delta_{F,L} &= \delta_0 \pm \frac{\delta_r}{2} \\
\alpha_{F,L} &= \alpha_0 \pm \frac{\alpha_r}{2}
\end{aligned}
\tag{3-14}
$$

where δ_0 and α_0 are the initial reference angles.

LQR Control Using Solar Sails

For the formation system, the differential accelerations imparted by SRP can be approximated by Equation (3-12) assuming the angles defining sail orientations remain small. From this, it can be seen that the relative angles, δ_r and α_r determines the effect SRP has on the formation system. The simplifications presented above are applied to approximate the system as an affine system with the control inputs u being the relative angles δ_r and α_r. As there are only two control inputs for a system with three degrees of freedom, the solar sail controlled system is underactuated. In a similar approach as to how the Q and R matrices were selected for the underactuated thrusters controlled scenario, reasonable responses were observed when the Q and R matrices for the SRP control scenario were selected as

$$Q = 10^6 \begin{bmatrix} 1 & 0 & 0 & 0 & 0 & 0 \\ 0 & 1 & 0 & 0 & 0 & 0 \\ 0 & 0 & 1 & 0 & 0 & 0 \\ 0 & 0 & 0 & 1 & 0 & 0 \\ 0 & 0 & 0 & 0 & 1 & 0 \\ 0 & 0 & 0 & 0 & 0 & 1 \end{bmatrix}, \quad R = \begin{bmatrix} 1 & 0 \\ 0 & 1 \end{bmatrix} \tag{3-15}$$

In this case, B was assumed to be constant evaluated at $\gamma = 0$, we find it would only be the optimal values for the instant in which its values were determined.

$$B = \begin{bmatrix} 0 & 0 \\ 0 & 0 \\ 0 & 0 \\ 0 & 0 \\ a_{\max} & 0 \\ 0 & a_{\max} \end{bmatrix} \tag{3-16}$$

The gain matrix K is solved from Equation (3-4), and the relative control angles can be described by

$$u = -K\tilde{x} = \begin{bmatrix} \delta_r & \alpha_r \end{bmatrix}^T \tag{3-17}$$

where $\tilde{x}$ is the state error vector. This can then be substituted into the Equations (3-14) and (3-11) to yield more accurate simulation results. It should be noted that the assumption of a constant B matrix was only necessary to determine the constant K matrix. The time varying nature of B is accounted for in the simulation of the linearized system's response.

3.2.4 LQR Control of the Hybrid Propulsion System

There are benefits and shortcomings associated with the use of thrusters or solar sails for control. A thruster-controlled system can have much shorter settling times. However, solar-sail control negates the need for fuel expenditure. It is proposed that a hybrid system, with thrusters augmenting the control efforts from SRP, could attain desired system dynamics with comparatively low fuel requirements and reasonable settling times. Relative motion along the x axis is least influenced by SRP if small relative angles are to be assumed; thus, it is sensible to place thrusters to support control efforts along this axis. The state and control weighting matrices are of a similar form to those used for the fully actuated thruster-controlled scenario. The B matrix can be modified and expressed as

$$B = \begin{bmatrix} 0 & 0 & 0 \\ 0 & 0 & 0 \\ 0 & 0 & 0 \\ 1 & 0 & 0 \\ 0 & a_{\max} & 0 \\ 0 & 0 & a_{\max} \end{bmatrix} \tag{3-18}$$

where $a_{\max}$ is evaluated at $\gamma = 0$. The relative acceleration and angles derived using this method will be of the form

$$u = -K\tilde{x} = \begin{bmatrix} u_{xthr} & \delta_r & \alpha_r \end{bmatrix}^T \tag{3-19}$$

where u_{xthr} is the required relative thruster control acceleration along the x axis. The control acceleration input can then be expressed as

$$U = U_{srp} + U_{thr} \tag{3-20}$$

where U_{srp} and U_{thr} are the required SRP and thrusters accelerations. U_{srp} is given by Equation (3-11) and U_{thr} for this hybrid control scenario can be expressed as

$$U_{thr} = \begin{bmatrix} u_{xthr} \\ 0 \\ 0 \end{bmatrix} \tag{3-21}$$

3.3 Nonlinear Control Methods

For highly nonlinear systems, a linear control method may not be able to perform adequately, especially if a high degree of precision is required. This is as a direct result of the linear approximations made in developing the controller. Variable structure control (VSC) techniques are robust (can handle parametric uncertainties) and thus should be able to perform better than a linear control scheme when applied to the nonlinear system.

The basic premise of VSC is to bring the system states to defined surfaces (reaching phase) and then constraining them to the surfaces, forcing the states to converge to the desired states (sliding phase). The surfaces, called sliding surfaces, are chosen such that state trajectories are assured asymptotic stability when their motion is confined to them. This requires the control law to constantly vary or switch depending on what side of the sliding surface the trajectories are on, thereby forcing the system states to move toward it. This is shown graphically in Figure 3.1.

One subset of VSC is sliding mode control (SMC). The design of a sliding mode controller for a given n^{th} order system involves a methodical approach to defining the sliding surfaces and designing the reaching laws while maintaining stable trajectories. SMC will be the main focus of the following discussions.

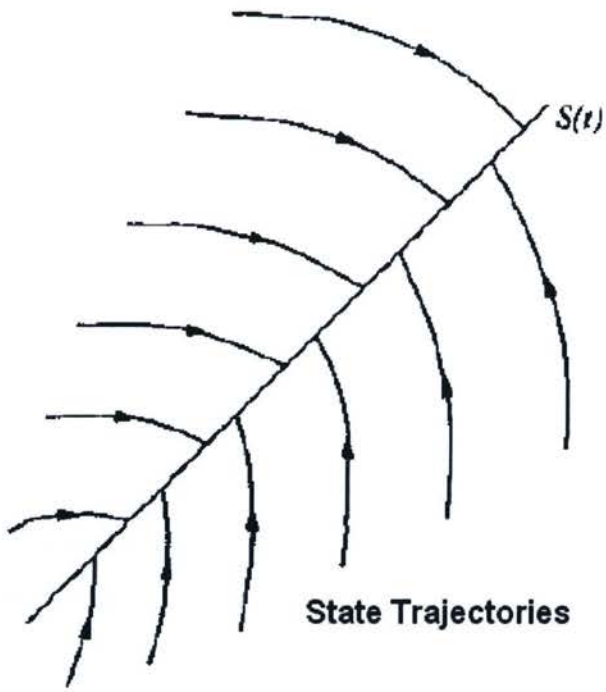

Figure 3.1 State trajectories reaching the sliding surface and sliding condition [56]

3.3.1 Conventional Sliding Mode Control

SMC provides an approach to designing the sliding surfaces. From this, the reaching laws can be derived. However, this method requires high frequency switching of the control input, causing a chattering response to be observed after states reach the sliding plane. These will be discussed here briefly for a general system, with more detailed derivations available in [56] and [57]. The design of the sliding surface and reaching laws are discussed first. A general approach to designing the control law will then be presented, followed by a brief discussion regarding strategies to reduce chattering in the control input.

Sliding Surface

Consider an nth order system. The sliding mode surface is defined via the relation

$$S = \left(\frac{d}{dt}\right)^{n-1} \tilde{x} + P_{n-1}\left(\frac{d}{dt}\right)^{n-2} \tilde{x} + \ \ldots \ + P_2 \dot{\tilde{x}} + P_1 \tilde{x} \tag{3-22}$$

where $\tilde{x} = x - x_d$ are the state errors. The symbols x and x_d denote the states and the desired states here. The coefficients P_i must be selected such that the characteristic roots of the sliding surfaces are stable. A general approach to accomplishing this is given as

$$P_{n-i} = \frac{(n-1)!}{(n-i-1)! \cdot i!} \lambda_d^{\ i} \tag{3-23}$$

where index $i = 1, 2, 3 \ldots n-2, n-1$, and symbol λ_d is the absolute value of the desired closed loop pole. Note that the sliding surface S is a function of the state errors and that $S = 0$ when $\tilde{x} = 0$. Therefore, elimination of state errors can be attained by driving S towards zero.

Lyapunov stability theory is used to evaluate the stability of a nonlinear system. Assuming a positive definite Lyapunov candidate function can be found, and its time derivative can be shown to be negative definite, then the sliding surface can be considered stable in the Lyapunov sense. For the sliding surface described by Equation (3-22), one can choose the Lyapunov candidate function as

$$V\left(S(t)\right) = \frac{1}{2} S^T S \tag{3-24}$$

Taking the derivative with respect to time, if

$$\dot{V}\left(S(t)\right) = S^T \dot{S} < 0 \tag{3-25}$$

then the sliding surface S will be asymptotically stable by the Lyapunov analysis. For this condition to be met, it is evident that

$$\dot{S} \begin{cases} < 0 & if\ S^T > 0 \\ = 0 & if\ S^T = 0 \\ > 0 & if\ S^T < 0 \end{cases} \tag{3-26}$$

Reaching Laws

Reaching laws are conditions that will bring state trajectories to the sliding surface and then confine them to it so that state errors will converge to zero. A constant rate reaching law can be found to be

$$\dot{S} = -\eta \operatorname{sgn}\left(S\right) \tag{3-27}$$

where η is a positive diagonal gain matrix and $\operatorname{sgn}\left(S\right)$ is the signum function of the column matrix S. This can be written for each element of matrix S as

$$\operatorname{sgn}(S_i) = \begin{cases} 1 & if\ S_i > 0 \\ 0 & if\ S_i = 0 \\ -1 & if\ S_i < 0 \end{cases} \tag{3-28}$$

where subscript $i = 1, 2, 3...$ denotes the ith term of the column matrix S. If we substitute Equation (3-27) into Equation (3-25), we find

$$\dot{V}\left(S(t)\right) = -\eta |S| \leq 0 \tag{3-29}$$

which is a negative semi-definite function. Asymptotic stability can only be ascertained if the Lyapunov candidate function has a negative definite derivative. Making use of Barbalat's lemma, however, we can still draw conclusions regarding the system's stability. Barbalat's lemma states that:

If a scalar function $V(x,t)$ satisfies the following conditions

- *$V(x,t)$ is lower bounded*
- *$\dot{V}(x,t)$ is negative semi-definite*
- *$\dot{V}(x,t)$ is uniformly continuous in time*

Then $\dot{V}(x,t) \to 0$ as $t \to 0$

Letting $W(t) = \eta|S|$, we have from Equation (3-29)

$$W(t) \leq -\dot{V}\left(S(t)\right) \tag{3-30}$$

Integrating,

$$\int_0^t W(t)dt \leq V\left(S(0)\right) - V\left(S(t)\right) \tag{3-31}$$

From this, it can readily be seen that $V\left(S(0)\right)$ is bounded. Since $\dot{V}\left(S(t)\right)$ is negative semi-definite and $V\left(S(t)\right)$ is positive definite, $V\left(S(t)\right)$ is always less than $V\left(S(0)\right)$ and is bounded as well. Taking the limit as $t \to \infty$, we have

$$\lim_{t\to\infty} \int_0^t W(t) < \infty \tag{3-32}$$

$\dot{W}(t)$ is bounded, and by Barbalat's lemma $S(t) \to 0$ as $t \to \infty$, showing that the sliding surface is stable.

Control Law Design

For a general nonlinear system with control input u,

$$\left(\frac{d}{dt}\right)^n x = f(x) + g(x)u \tag{3-33}$$

substitution into the time derivative of Equation (3-22) for $\left(\frac{d}{dt}\right)^n \tilde{x}$ yields

$$\dot{S} = f(x) + g(x)u - x_d^{(n)} + P_{n-1}\left(\frac{d}{dt}\right)^{n-1} \tilde{x} + \ \dots \ + P_2\ddot{\tilde{x}} + P_1\dot{\tilde{x}} \tag{3-34}$$

where $\dot{x}_d$ denotes the desired state derivatives. Comparing Equation (3-34) with Equation (3-26), it can be shown that u can be expressed as

$$u \begin{cases} < \beta & if \ S^T > 0 \\ = \beta & if \ S^T = 0 \\ > \beta & if \ S^T < 0 \end{cases} \tag{3-35}$$

where

$$\beta = \frac{-1}{g(x)}\left[f(x) - x_d^{(n)} + P_{n-1}\left(\frac{d}{dt}\right)^{n-1} \tilde{x} + \ \dots \ + P_2\ddot{\tilde{x}} + P_1\dot{\tilde{x}} \right] \tag{3-36}$$

Now if Equation (3-34) is substituted into Equation (3-27), the control law can be found as

$$u = \beta - \frac{1}{g(x)} \eta \operatorname{sgn}(S) \tag{3-37}$$

Chattering

The switching control input described in Equation (3-37) constrains state trajectories to constantly be pointed towards the sliding surface. The strategy is effective since state trajectories moving along the sliding surface are guaranteed to reach a zero error state. However, the high frequency control switching results in a great degree of control activity to maintain state trajectories on the sliding surface. This results in the chattering phenomenon which is shown in Figure 3.2. Chattering is undesirable because it is fuel inefficient and rapidly wears down actuation devices.

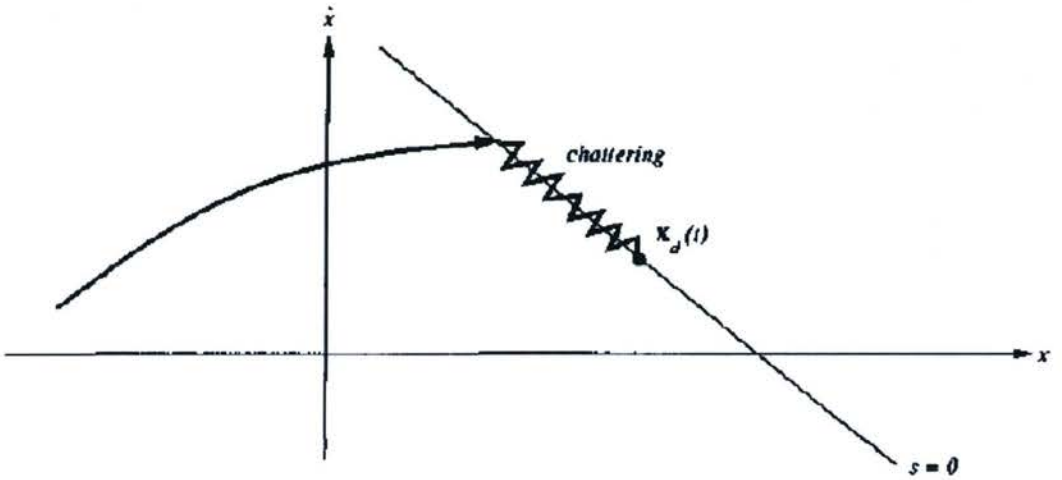

Figure 3.2 Chattering effect due to constant control switching [56]

In practice, a trade-off must be made between attaining ideal sliding mode performance and reducing input activity to more realistically attainable profiles. As such, modification of the control law shown in Equation (3-37) is necessary. One method of doing so is to implement a boundary layer region in the immediate vicinity of the sliding surfaces. Then, by modifying the control inputs when state trajectories are in this region, the chattering effect can be reduced.

Letting Φ represent the boundary layer thickness, replacing the sign function in Equation (3-27) with a saturation function, defined as [56]

$$\operatorname{sgn}(S) = sat\left(\frac{S}{\Phi}\right) = \begin{cases} \dfrac{S}{\Phi} & if \left|\dfrac{S}{\Phi}\right| \le 1 \\ \operatorname{sgn}\left(\dfrac{S}{\Phi}\right) & otherwise \end{cases} \tag{3-38}$$

will result in the modified control law

$$u = \beta - \frac{1}{g(x)} \eta sat\left(\frac{S}{\Phi}\right) \tag{3-39}$$

Alternatively, a smoother control input profile can be achieved through using a hyperbolic tangent function instead of the saturation function. In that case, the control law could be expressed as

$$u = \beta - \frac{1}{g(x)} \eta \tanh\left(\frac{S}{\Phi}\right) \tag{3-40}$$

3.3.2 Integral Augmented Sliding Mode Control

In conventional SMC, the sliding surface is defined as a function of the state errors $\tilde{x}$ and its derivatives, yet this does not necessarily prevent the occurrence of steady state errors. To eliminate steady state errors, an integral augmented sliding mode controller can be used, as described in [58].

Consider the sliding surface described by Equation (3-22). We now modify this definition with the addition of integral control action. The sliding surface and its derivative now becomes

$$S = \left(\frac{d}{dt}\right)^{n-1} \tilde{x} + P_{n-1}\left(\frac{d}{dt}\right)^{n-2} \tilde{x} + \ldots + P_2\dot{\tilde{x}} + P_1\tilde{x} + K_i \int_0^t \tilde{x} \tag{3-41}$$

$$\dot{S} = \left(\frac{d}{dt}\right)^{n} \tilde{x} + P_{n-1}\left(\frac{d}{dt}\right)^{n-1} \tilde{x} + \ldots + P_2\ddot{\tilde{x}} + P_1\dot{\tilde{x}} + K_i\tilde{x} \tag{3-42}$$

where K_i represents the integral gain.

3.3.3 Sliding Mode Control for the Underactuated System

The sliding surface definitions discussed thus far are applicable to fully actuated cases. In underactuated circumstances, such as in the event of the failure of control actuation along one of the axes, the inability of the conventional SMC method to overcome mismatched disturbances and uncertainties becomes evident, as will be shown in Chapter 4. Due to the coupled nature of the formation system in this study, it may be possible to exploit this aspect to gain control of in-plane motions using actuators along one of it's axis of motion only. Modifications to the conventional SMC scheme are necessary to accomplish this task.

A method for dealing with the underactuated scenario through modifications to the conventional SMC design methodology was proposed by Godard and Kumar [59]. The sliding surface for the in-plane motion is redefined as a linear combination of the in-plane state errors. This method is applied to the underactuated system of this study as follows.

Consider the error dynamics of the linearized in-plane formation system expressed as

$$\begin{bmatrix} \dot{\tilde{x}} \\ \dot{\tilde{y}} \\ \ddot{\tilde{x}} \\ \ddot{\tilde{y}} \end{bmatrix} = \begin{bmatrix} 0 & 0 & 1 & 0 \\ 0 & 0 & 0 & 1 \\ \frac{3}{4} & C & 0 & 2 \\ C & \frac{9}{4} & -2 & 0 \end{bmatrix} \begin{bmatrix} \tilde{x} \\ \tilde{y} \\ \dot{\tilde{x}} \\ \dot{\tilde{y}} \end{bmatrix} + \begin{bmatrix} 0 & 0 \\ 0 & 0 \\ b_1 & 0 \\ 0 & b_2 \end{bmatrix} \begin{bmatrix} u_{xr} \\ u_{yr} \end{bmatrix} \tag{3-43}$$

which is of the form

$$\dot{\tilde{x}} = A\tilde{x} + Bu_r \tag{3-44}$$

where the constant $C = \frac{3\sqrt{3}}{2}\left(\nu - \frac{1}{2}\right)$. In this study, the system will be assumed to be underactuated in x. This is modeled by setting $b_1 = 0$ in the control matrix. Motions along the x axis will now be indirectly controlled through control efforts along y only. Partitioning the system into the actuated and underactuated parts, one has

$$\begin{bmatrix} \dot{\tilde{X}}_1 \\ \dot{\tilde{X}}_2 \end{bmatrix} = \begin{bmatrix} A_{11} & A_{12} \\ A_{21} & A_{22} \end{bmatrix} \begin{bmatrix} \tilde{X}_1 \\ \tilde{X}_2 \end{bmatrix} + \begin{bmatrix} 0 \\ B_2 \end{bmatrix} u_r \tag{3-45}$$

where

$$A_{11} = \begin{bmatrix} 0 & 0 & 1 \\ 0 & 0 & 0 \\ \frac{3}{4} & C & 0 \end{bmatrix} \quad A_{12} = \begin{bmatrix} 0 \\ 1 \\ 2 \end{bmatrix} \quad B_2 = \begin{bmatrix} 0 & b_2 \end{bmatrix}$$

$$A_{21} = \begin{bmatrix} C & \frac{9}{4} & -2 \end{bmatrix} \quad A_{22} = [0] \quad \tilde{X}_1 = \begin{bmatrix} \tilde{x}_r \\ \tilde{y}_r \\ \dot{\tilde{x}}_r \end{bmatrix} \quad \tilde{X}_2 = \begin{bmatrix} \dot{\tilde{y}}_r \end{bmatrix} \tag{3-46}$$

The sliding surface for the in-plane motion is defined here as

$$S_{xy} = \Lambda_1 \tilde{X}_1 + \Lambda_2 \tilde{X}_2 \tag{3-47}$$

Where $\Lambda_1 \in \mathbb{R}^{1\times 3}$ and $\Lambda_2 \in \mathbb{R}^{1\times 1}$ are the state weighting matrices. If errors are to remain on the sliding surface, the condition $S = 0$ after the system reaches it must be true.

Imposing this condition on the sliding surface and isolating the error states that can be directly compensated for with actuation, one has

$$\tilde{X}_2 = -\Lambda_2^{-1}\Lambda_1\tilde{X}_1 \tag{3-48}$$

Substitution of this expression into the partitioned matrix of Equation (3-45), one obtains

$$\dot{\tilde{X}}_1 = \left(A_{11} - A_{12}K\right)\tilde{X}_1 \tag{3-49}$$

where the constant design gain matrix K dictates the behaviour of the system and is defined by

$$K = \Lambda_2^{-1}\Lambda_1 = \begin{bmatrix} K_1 & K_2 & K_3 \end{bmatrix} \tag{3-50}$$

Since the system is coupled and underactuated in x, $\tilde{X}_2 = \left[\dot{\tilde{y}}_r\right]$ may be viewed as the control effort that drives the underactuated state to the desired trajectory. Setting $\Lambda_2 = 1$, the sliding surface for the in-plane motions can be expressed as follows after substitution

$$S_{xy} = \dot{\tilde{y}}_r + K_1\tilde{x}_r + K_2\tilde{y}_r + K_3\tilde{z}_r \tag{3-51}$$

The sliding surface definition pertaining to the out of plane motion is determined through the conventional approach.

3.3.4 Sliding Mode Control of the Thruster-Controlled System

SMC Using Thrusters in a Fully Actuated Configuration

Recall that the general nonlinear system is of the form

$$\left(\frac{d}{dt}\right)^n x = f(x) + g(x)u \tag{3-52}$$

The function $f(x)$ represents the equations of motion previously defined in Chapter 2 and $g(x)$ is equal to the 3x3 identity matrix for a fully actuated thruster-controlled system. Stability of the general fully actuated system was shown using the conventional SMC method. Applying conventional SMC to the fully actuated thruster-controlled system, the sliding surfaces can be found to be

$$S = \begin{bmatrix} S_x \\ S_y \\ S_z \end{bmatrix} = \begin{bmatrix} \dot{\tilde{x}}_r + K_1\tilde{x}_r \\ \dot{\tilde{y}}_r + K_2\tilde{y}_r \\ \dot{\tilde{z}}_r + K_3\tilde{z}_r \end{bmatrix} \tag{3-53}$$

The constant rate reaching laws are equated to the derivative of the sliding surface definitions,

$$-\eta\,\mathrm{sgn}(S) = \begin{bmatrix} (\ddot{x}_r - \ddot{x}_d) + K_1(\dot{x}_r - \dot{x}_d) + u_x \\ (\ddot{y}_r - \ddot{y}_d) + K_2(\dot{y}_r - \dot{y}_d) + u_y \\ (\ddot{z}_r - \ddot{z}_d) + K_3(\dot{z}_r - \dot{z}_d) + u_z \end{bmatrix} \tag{3-54}$$

where the constant rate reaching matrix η is selected as a 3x3 positive diagonal matrix expressed as

$$\eta = \begin{bmatrix} \eta_1 & 0 & 0 \\ 0 & \eta_2 & 0 \\ 0 & 0 & \eta_3 \end{bmatrix} \tag{3-55}$$

By rearranging, the SMC law for the fully actuated thrusters-controlled system can be expressed as

$$\begin{aligned} u_x &= -(\ddot{x}_r - \ddot{x}_d) - K_1(\dot{x}_r - \dot{x}_d) - \eta_1 \operatorname{sgn}(S_x) \\ u_y &= -(\ddot{y}_r - \ddot{y}_d) - K_2(\dot{y}_r - \dot{y}_d) - \eta_2 \operatorname{sgn}(S_y) \\ u_z &= -(\ddot{z}_r - \ddot{z}_d) - K_3(\dot{z}_r - \dot{z}_d) - \eta_3 \operatorname{sgn}(S_z) \end{aligned} \tag{3-56}$$

SMC Using Thrusters in an Underactuated Configuration

With thruster acceleration being the control input for the underactuated scenario, $g(x)$ is equal to the 2x2 identity matrix. For the underactuated scenarios of this study, it is assumed the system has control inputs along the relative y and z axes only. The integral augmented sliding surfaces can be defined as

$$S = \begin{bmatrix} S_{xy} \\ S_z \end{bmatrix} = \begin{bmatrix} \dot{\tilde{y}} + K_1\tilde{x} + K_2\dot{\tilde{x}} + K_3\tilde{y} + K_4\int_0^t \tilde{y}\, d\tau \\ \dot{\tilde{z}} + K_z\tilde{z} \end{bmatrix} \tag{3-57}$$

where K_i are the gains, $\tilde{x}, \tilde{y}, \tilde{z}$ are the state errors and S_{xy} and S_z are the sliding surfaces for the in-plane and out-of-plane motions, respectively. Equating $\dot{S}$ to the constant rate reaching law described by Equation (3-27),

$$-\eta \operatorname{sgn}(S) = \begin{bmatrix} (\ddot{y}_r - \ddot{y}_d + u_y) + K_1(\dot{x}_r - \dot{x}_d) + K_2(\ddot{x}_r - \ddot{x}_d) + K_3(\dot{y}_r - \dot{y}_d) + K_4(y_r - y_d) \\ (\ddot{z}_r - \ddot{z}_d + u_z) + K_z(\dot{z}_r - \dot{z}_d) \end{bmatrix} \tag{3-58}$$

where subscript 'd' denotes the desired states; subscript 'r' denotes the relative states determined through integration of the relative equations of motion shown in Chapter 2; u_y and u_z are the control accelerations, and η is the positive constant rate reaching matrix

$$\eta = \begin{bmatrix} \eta_1 & 0 \\ 0 & \eta_2 \end{bmatrix} \tag{3-59}$$

Solving for the control inputs, the control law can be expressed as

$$\begin{aligned} u_y &= -\left(\ddot{y}_r - \ddot{y}_d\right) - K_1\left(\dot{x}_r - \dot{x}_d\right) - K_2\left(\ddot{x}_r - \ddot{x}_d\right) \\ &\quad -K_3\left(\dot{y}_r - \dot{y}_d\right) - K_4\left(y_r - y_d\right) - \eta_1 \operatorname{sgn}\left(S_{xy}\right) \\ u_z &= -\left(\left(\ddot{z}_r - \ddot{z}_d\right) + K_z\left(\dot{z}_r - \dot{z}_d\right)\right) - \eta_2 \operatorname{sgn}\left(S_z\right) \end{aligned} \tag{3-60}$$

To reduce the chattering effect, the control laws are modified to be

$$\begin{aligned} u_y &= -\left(\ddot{y}_r - \ddot{y}_d\right) - K_1\left(\dot{x}_r - \dot{x}_d\right) - K_2\left(\ddot{x}_r - \ddot{x}_d\right) \\ &\quad -K_3\left(\dot{y}_r - \dot{y}_d\right) - K_4\left(y_r - y_d\right) - \eta_1 \tanh\left(S_{xy}\right) \\ u_z &= -\left(\left(\ddot{z}_r - \ddot{z}_d\right) + K_z\left(\dot{z}_r - \dot{z}_d\right)\right) - \eta_2 \tanh\left(S_z\right) \end{aligned} \tag{3-61}$$

Stability for this underactuated sliding mode controlled system can be analyzed in the same way that stability is assessed in conventional SMC. Consider the Lyapunov candidate function given by Equation (3-24). Taking its derivative and substituting in for $\dot{S}$, it can be written as

$$\dot{V} = S^T \begin{bmatrix} \left(\ddot{y}_r - \ddot{y}_d + u_y\right) + K_1\left(\dot{x}_r - \dot{x}_d\right) + K_2\left(\ddot{x}_r - \ddot{x}_d\right) + K_3\left(\dot{y}_r - \dot{y}_d\right) + K_4\left(y_r - y_d\right) \\ \left(\ddot{z}_r - \ddot{z}_d + u_z\right) + K_z\left(\dot{z}_r - \dot{z}_d\right) \end{bmatrix} \tag{3-62}$$

If the control law given by Equation (3-60) is substituted into this, it can be shown that Equation (3-62) reduces to be of the same form as Equation (3-29). Since the conditions necessary for Barbalat's Lemma to hold are met, the underactuated sliding mode controlled system developed here can be considered stable in the Lyapunov sense.

3.3.5 Bang-Bang Control of the Underactuated System

Continuous control methods are suitable for preliminary analysis and may also be applicable in practice provided the motion is slow enough. Bang-bang controllers are also developed and applied to the formation system and, as will be shown in Chapter 4 and Chapter 5, this control scheme is applicable to both the thrusters and solar sail controlled scenarios.

In bang-bang control, the goal is to design the appropriate switching laws; that is, the conditions upon which the control input will switch from its minimum to maximum values and vice versa. In this study, it is assumed that a switching law can be found as a function of the sliding plane definitions. A viable control law can then be expressed as

$$\begin{aligned} u_y &= -\sigma_1 \operatorname{sgn}\left(S_{xy}\right) \\ u_z &= -\sigma_2 \operatorname{sgn}\left(S_z\right) \end{aligned} \tag{3-63}$$

where σ_i represents the magnitude of the control input. If this control law is substituted into the Lyapunov candidate function given by Equation (3-62), it is easily seen that careful selection of $\sigma_{1,2}$ can ensure that $\dot{V}$ is negative semi-definite. From this, stability in the Lyapunov sense of the bang-bang controlled system can be deduced from Barbalat's lemma.

3.4 Developed Controllers Summary

Linear and nonlinear controllers for various scenarios were developed in this chapter. The particular scenarios for which they were developed for is summarized in Figures 3.3 and 3.4.

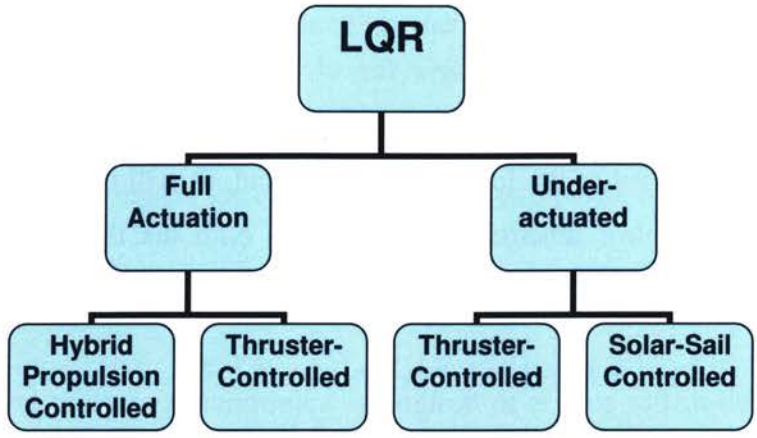

Figure 3.3 Scenarios linear controllers are developed for

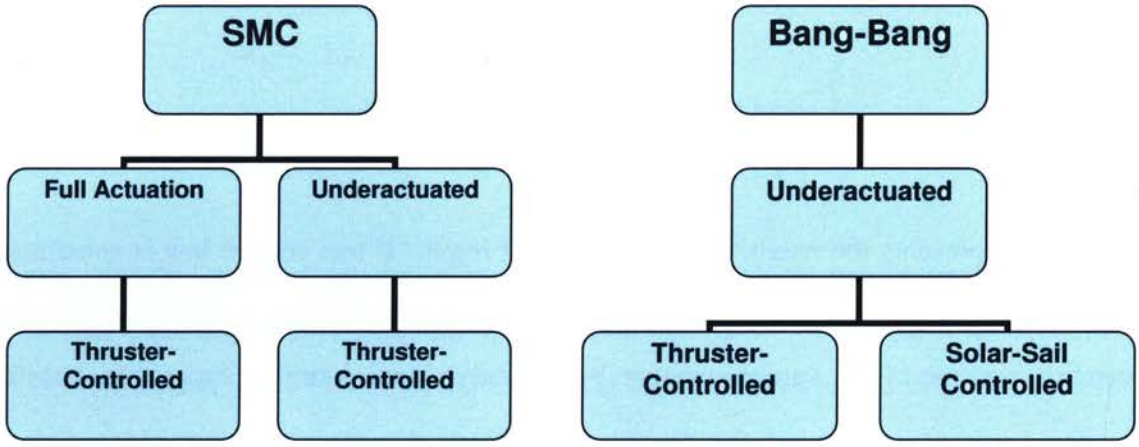

Figure 3.4 Scenarios nonlinear controllers are developed for

3.5 Numerical Solvers

Simulated results of applying the controllers developed in this chapter to the formation system are presented in the following chapters. Since simulation results can vary depending on the accuracy of the chosen solver and set tolerances, a discussion regarding the simulation set up is warranted.

The results presented in this thesis were computed using the solvers included in the MATLAB / Simulink software package. In general, an appropriately configured ODE45 solver provided reasonably accurate results using a fourth order Runge-Kutta method to solve for the relative motions [60]. However, simulation durations were lengthy when using this variable step solver. It was found that simulation times were substantially reduced using the ODE3 fixed step solver. The ODE3 solver uses a third order Runge-Kutta method [61], but when sufficiently small time step sizes were used, it's performance was comparable to that of the ODE45 solver. It was observed that using time step sizes of 5 hours or less produced results similar to those obtained using the ODE45 solver in a much shorter time frame. For this reason, ODE3 was the solver used in the majority of the simulations conducted for this study.

Chapter 4

Trajectory Tracking Using Thrusters

4.1 Introduction

In this chapter, the control methods developed in Chapter 3 for the thruster-controlled system are applied to the spacecraft-formation model described in Chapter 2. The results are presented and discussed regarding their efficacy in tracking the formation reference trajectory. First, simulations of the spacecraft formation system's dynamics without control are presented in order to firmly establish the need for system control. Elliptical trajectory tracking control scenarios using thrusters in fully actuated and underactuated configurations are then presented. This is followed by attempts to track an in-plane circular trajectory using thrusters.

4.2 Desired Trajectory and Natural Motions

The desired trajectory is shown in Figure 4.1 and has semi-major and semi-minor axes lengths of approximately 14 km and 7 km, respectively. The initial conditions for this trajectory are shown in Table 4.1. The reference was chosen to have similar initial conditions used by Catlin and McLaughlin [5] for the short period formation case, but with larger initial velocities to generate a bigger reference trajectory. Since the reference trajectory was derived using equations linearized about the L4 point, nonlinearity effects

would become more pronounced with the larger reference trajectory size. The efficacy of the developed controllers in countering these nonlinerities can therefore be more readily observed.

Table 4.1: Ideal Initial Conditions for Reference In-Plane Elliptical Relative Motion

	x_0 (km)	y_0 (km)	z_0 (km)	$\dot{x}_0$ (m/s)	$\dot{y}_0$ (m/s)	$\dot{z}_0$ (m/s)
Leader	1500	2975	0	10	1.70	0
Follower	1505	2984	0	10.03	1.71	0
Relative	5	9.13	0	0.03	0.0043	0

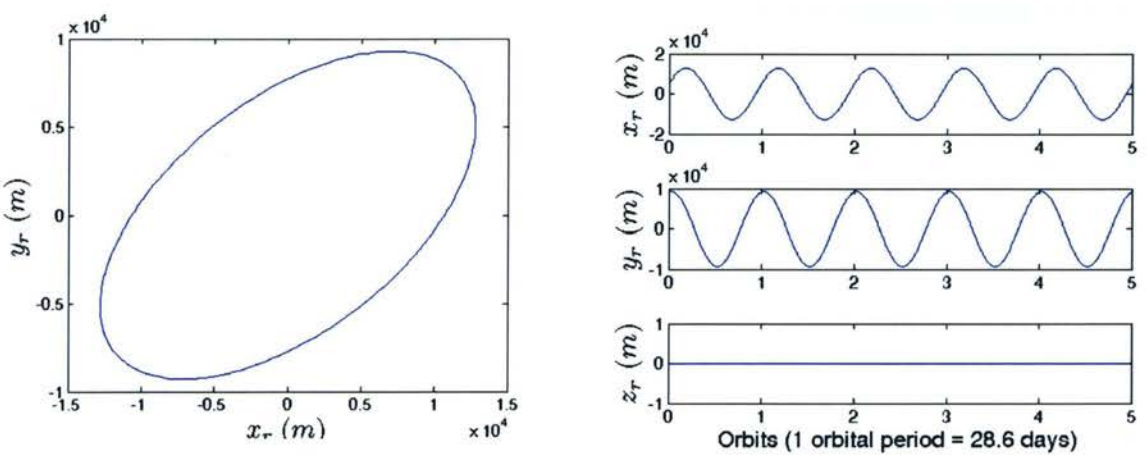

Figure 4.1 Reference in-plane elliptical relative trajectory

It is important to establish the need for control. Plots of the linearized relative motion under nonideal conditions and without control efforts are shown in Figure 4.2. It can be seen that an initial offset error of 1 km in the relative x direction has significant effects on the motion's trajectory. An offset of just 1 km in the relative x direction causes the amplitude of the bounded motion to increase from less than 1 km to several kilometers in the relative x and y directions. This is in contrast to out of plane motions, which can be described as simple harmonic. Although not shown, out of plane motion is bounded with amplitudes equal to the initial relative offset error in the z direction. Although the

motion is bounded, its trajectory is complicated and is of little use in practical applications [5].

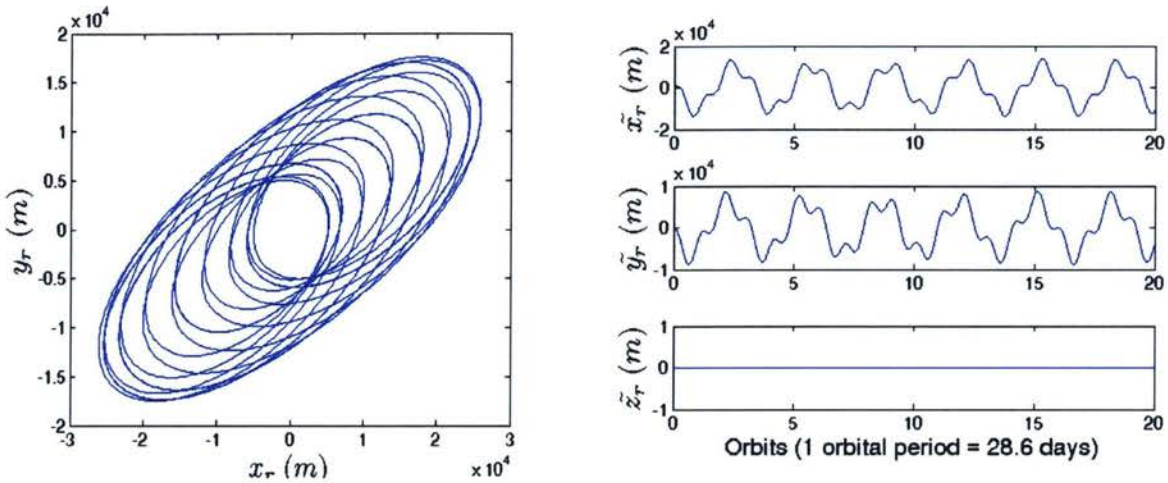

Figure 4.2 Relative motion and errors in the linearized system when initial offset error is 1 km in x_r

Effect of Nonlinearities

To examine the nonlinearity effects, motion of the nonlinear system is simulated using the ideal initial conditions (see Table 4.1) and offset initial conditions, the results of which are shown in Figures 4.3 and 4.4. The errors in the relative motion appear to oscillate over the course of the simulation time span of 20 orbital periods. However, the errors appear to remain bounded, with the slight increases over the long simulation time span attributable to accumulated numerical errors. Since the leader satellite was assumed to be in a reference orbit and the relative errors appear to remain bounded, it can therefore be reasoned that the follower satellite's motion is bounded as well.

The result of initial offset errors applied to the nonlinear system were similar to that of the linear case, further underscoring that system nonlinearities do not cause the relative motion to diverge.

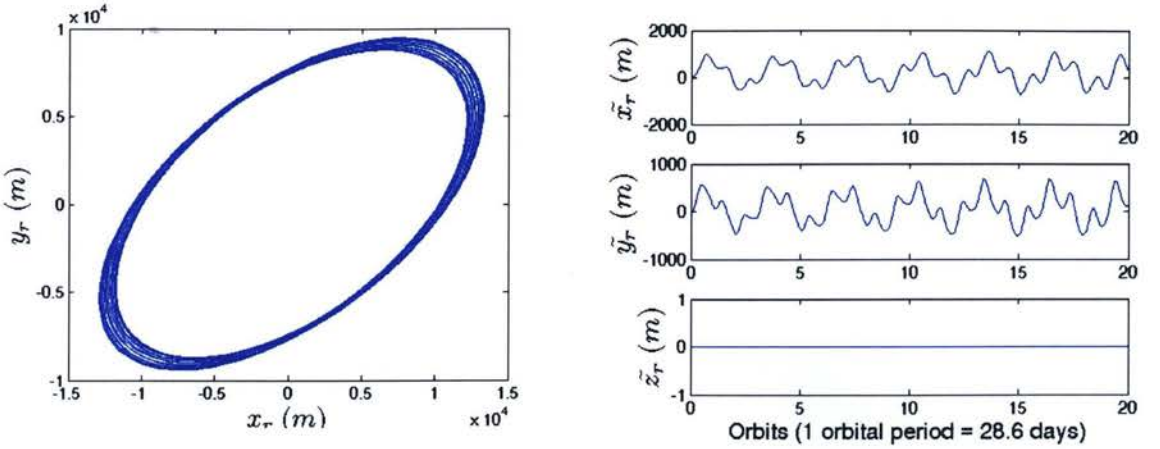

Figure 4.3 Effect of nonlinearities when ideal initial conditions are applied

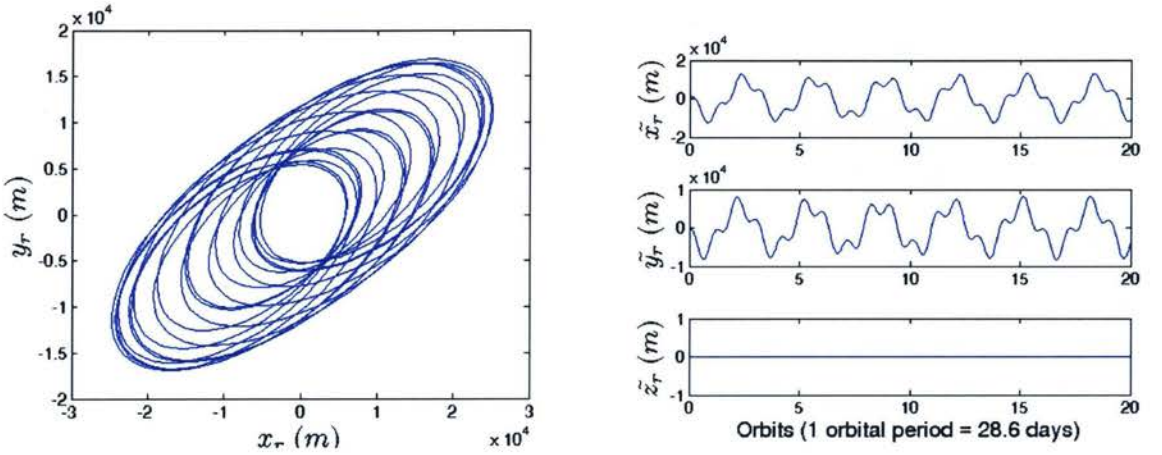

Figure 4.4 Effect of initial offset errors on the relative motion in the nonlinear system. Initial offset error is 1 km in x_r

Effect of the Sun's Gravity

From Figures 4.3 and 4.4, it is apparent that the motion remained bounded in the presence of initial offset errors and nonlinearities. This would imply that an active control scheme would only be necessary if precision tracking of the desired relative trajectory is required. However, these simulations do not consider the effect of the Sun. If the perturbing effect of the Sun's gravity is accounted for, the relative motion is no longer bounded. The effect of this perturbing force on the system is shown in Figure 4.5. From this plot, it can be observed that the tracking error increases if the spacecraft formation is left uncontrolled. This result shows the need for an active control system that can counter the

perturbing effect of the Sun. In the next section, the results of using an LQR control scheme for both the linear and nonlinear formation system are discussed.

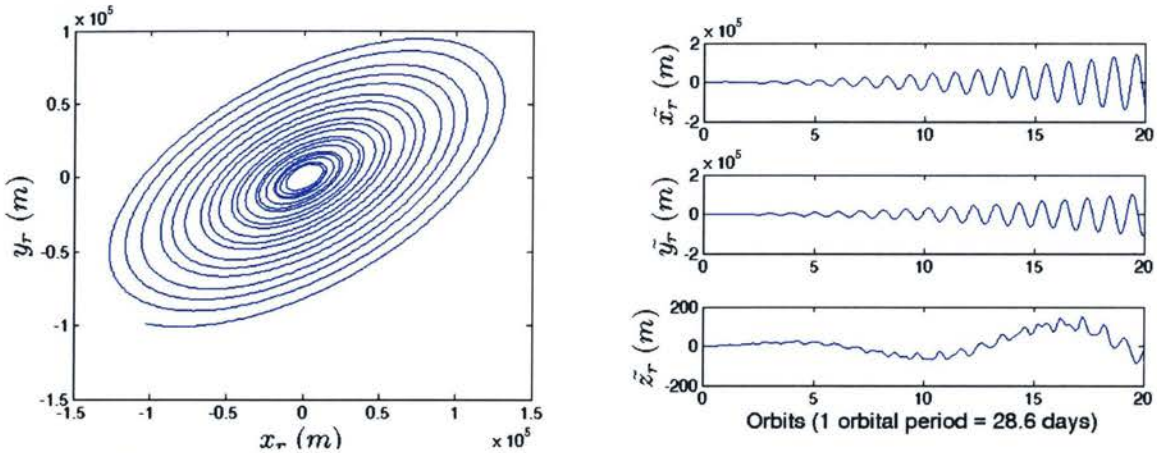

Figure 4.5 Effect of Sun's gravity on relative motion given ideal initial conditions

4.3 Results and Discussion: Elliptic Trajectory Tracking

4.3.1 Fully Actuated System

A fully actuated system using thrusters can in principle control any space system provided that the required control efforts are not unattainably large. It is reasonable to presume that control efforts along each axis in the underactuated scenario will be greater than that of the fully actuated case as a result of fewer thrusters compensating for control efforts in the unactuated axis. If trajectory tracking using a fully actuated system could only be achieved with unreasonably large control accelerations, then further studies into underactuated controls would be baseless. Therefore, before proceeding with the analysis of the underactuated system, it is sensible to examine the control efforts required in a fully actuated system first.

The results of applying the SMC controller developed in Chapter 3 on this system are now presented. Gains for the sliding planes were determined by applying LQR to the nondimensionalized equations of motion. The state and control weighting matrices used in this analysis that yielded reasonable responses were found through trial and error as

$$\bar{Q} = 10 I_{6x6} \qquad \bar{R} = I_{3x3}$$

where I is the identity matrix and the overbar signifies that these matrices are only applicable to the nondimensionalized analysis. The system is given an initial offset error of 1 km along each axis and the perturbing force of the Sun's gravity on the formation system is accounted for. As noted in Chapter 3, it is assumed all states are measurable and that no sensor noise is present. The simulation results are shown in Figure 4.6.

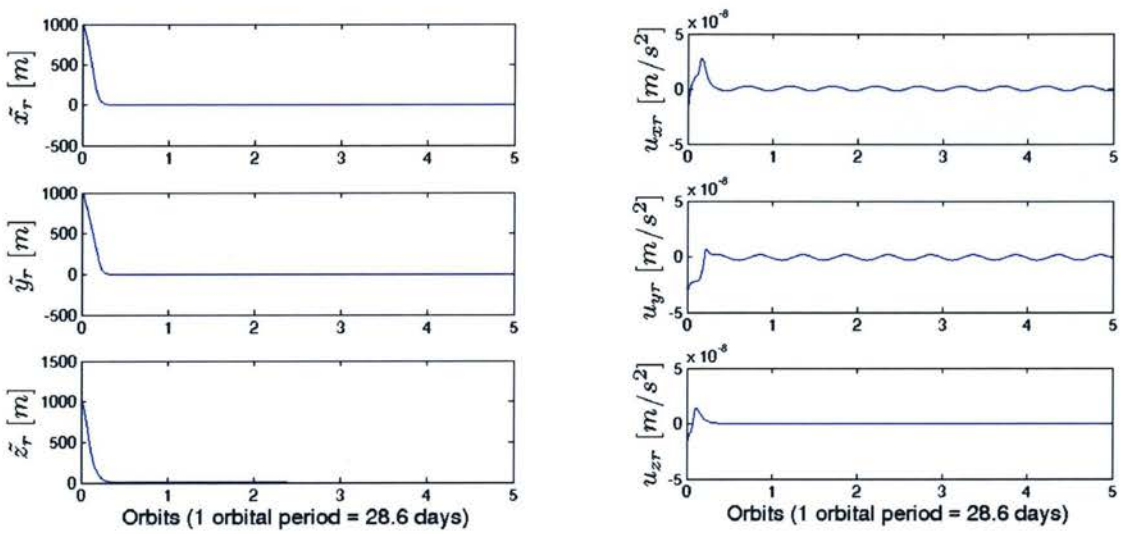

Figure 4.6 System response with full actuation in Sun gravity perturbed environment using sliding mode control

The error plots shows the settling time to be less than half an orbital period in each axis with negligible steady state errors. Control efforts are continually required to counteract the perturbing effects of the Sun. The scale of the required control input accelerations are extremely small; on the order of 10^{-9} m/s^2 during steady state. For a large satellite with a mass of a thousand kilograms or more, such small accelerations are achievable using electric propulsion systems. Since control efforts in this case are small and realizable for large satellites or spacecraft, further research into formation control in an underactuated scenario is merited.

4.3.2 Underactuated System

Analysis of the underactuated system will begin with linear analysis of the unperturbed system to help simplify the problem. This will be followed by more complex analysis of the nonlinear system in perturbed and unperturbed states controlled using linear and nonlinear techniques. Finally, a bang-bang controller is applied to the system to demonstrate that on/off control of the underactuated system is possible.

Control of the Linearized System

The unperturbed, linearized system provides a starting point for understanding the dynamics of this formation system. A LQR control scheme is applied to the dimensionalized system with offset errors of 1 km in all axes. Control efforts are limited to act along the relative y and z axes only. Reasonable responses were observed when state and control weighting matrices used to determine the LQR gains were selected to be

$$Q = 10^{-21} I_{6\times6} \qquad\qquad R = I_{2\times2}$$

The efficacy of such a control scheme is shown in Figure 4.7.

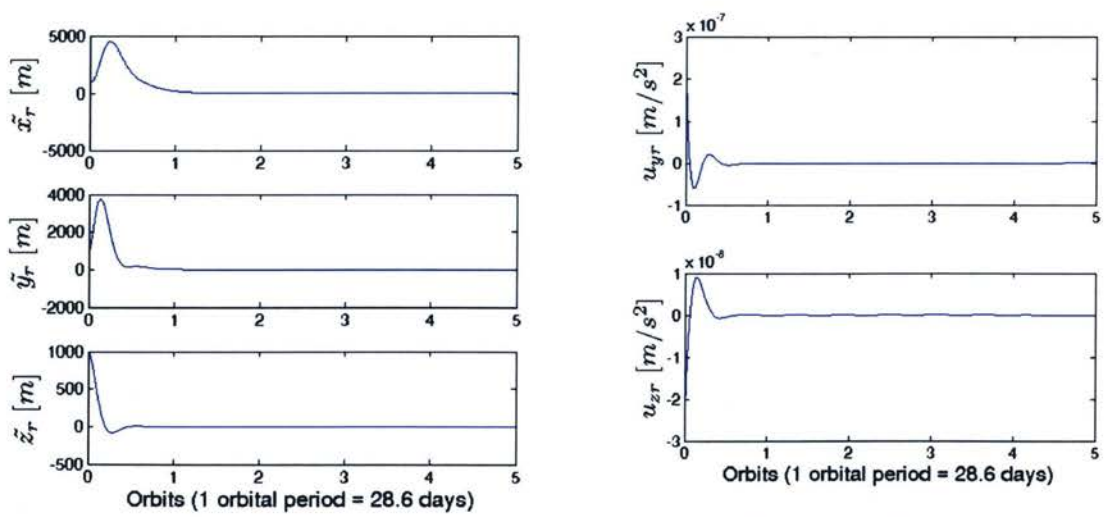

Figure 4.7 Response of the unperturbed linearized system using a linear controller

Large increases in the errors of the in-plane axes are initially observed in the error plots. This increase is attributable to the controller's inability to directly influence relative motions in the x direction, hindering its efforts to alter initial velocities that perpetuate errors. Settling times are adjusted to be similar to that of the fully actuated case.

The linear system does not exhibit steady state errors since it is tracking a natural formation trajectory derived using the linear system equations. Control efforts are greatest initially and decrease to zero as the system reaches steady state.

Application of Linear Control to the Nonlinear System

In many control problems, a linear controller is sufficient for practical applications. However, these controllers only perform well locally, in regions where linear approximations are valid. To assess how well the linear controller can perform in the nonlinear model, a linear control scheme is applied to the nonlinear system here with identical initial conditions as the linear case. The results are presented in Figure 4.8. It can be clearly seen that in this underactuated system, oscillations in the motion during steady state exist are caused by the controller attempting to counter the nonlinearities of the system. Further gain adjustments did not result in smaller oscillation amplitudes at steady state. However, the bounded motion amplitudes remained within several hundred metres, which is tolerable for a variety of potential formation flight missions. For instance, a mission involving an automated service and repair satellite that is required to remain in an orbit close to the leader satellite until servicing is required. It could also be suitable for a visual survey mission, such as a satellite orbiting a space station or spacecraft searching for signs of damage. Separation distances between spacecrafts in such missions could be on the order of a few kilometres. As such, oscillatory motions at steady state with amplitudes significantly smaller than these separation distances can still be acceptable.

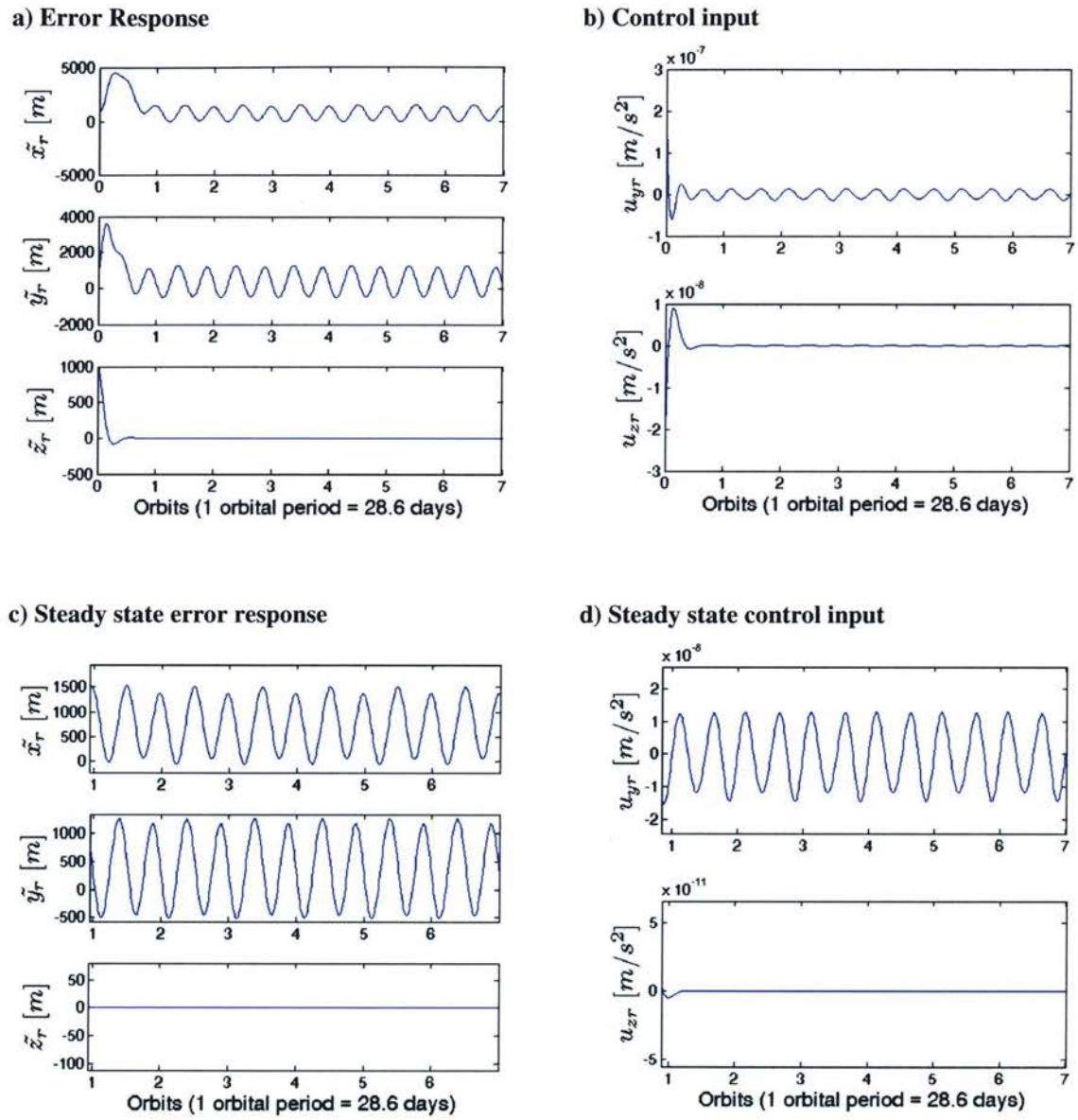

Figure 4.8 Response of the unperturbed nonlinear system using a linear controller

Unlike the linear system case, in-plane control inputs during steady state are non zero, although they are extremely small. Average steady state error in x_r direction is approximately 500 m, whereas in y_r it is about 300 m. This offset can be eliminated using an integral term in the control law as shown in Figure 4.9.

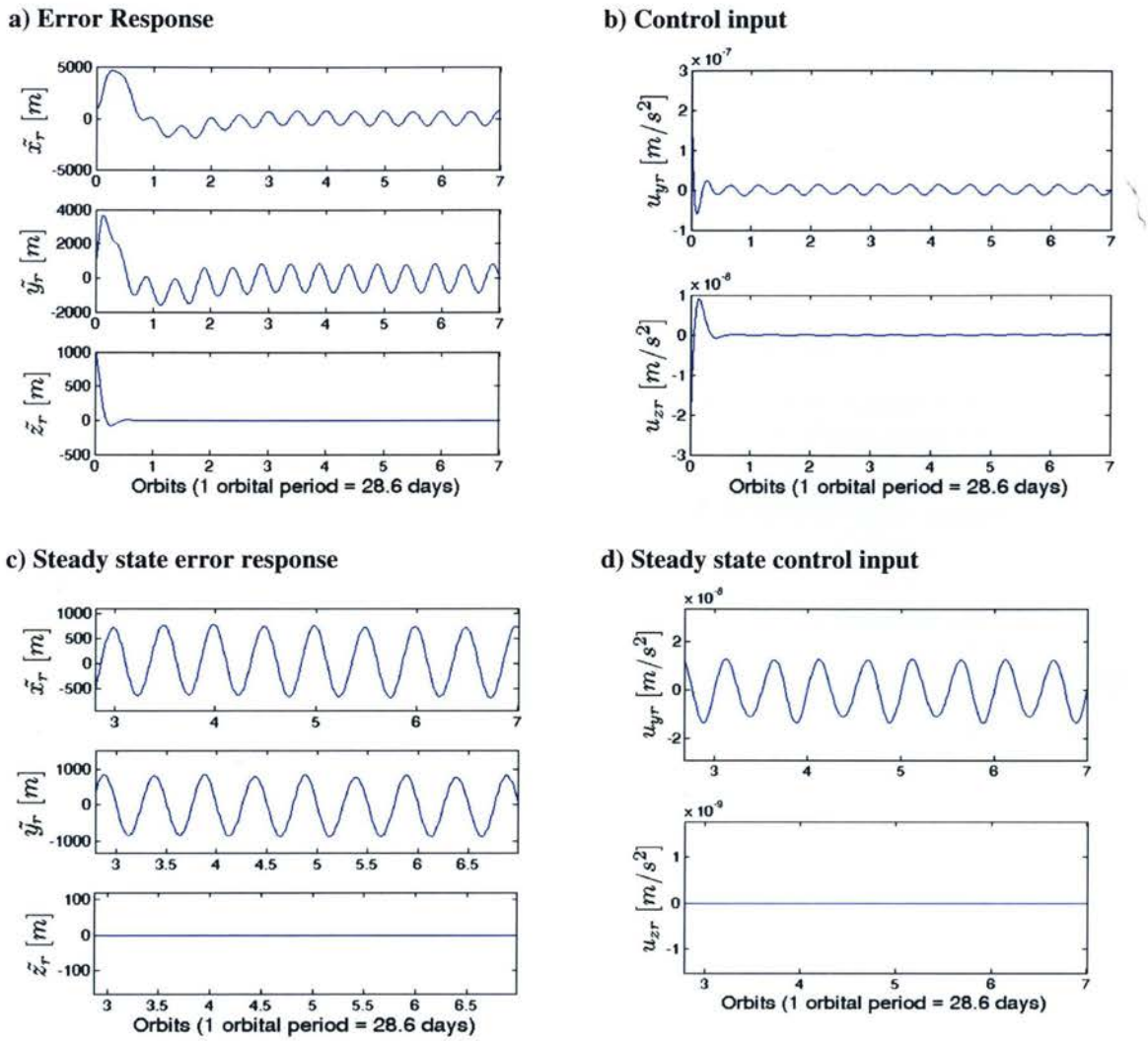

Figure 4.9 Underactuated system response using a linear controller with integral control

It is clearly seen that the average steady state error has been reduced to zero using an integral term. Oscillations during steady state remained bounded between -500 to 500 m in x_r and y_r. Since steady state offset errors only exist for in-plane motion, as seen in Figure 4.8, integral control action was only necessary for in-plane control. An appropriate gain matrix for the integral component that eliminated steady state error was found through trial and error to be

$$K_{\text{int}} = -10^{-17}\begin{bmatrix} 1 & 1 & 0 \\ 0 & 0 & 0 \end{bmatrix}$$

Nonlinear Control of the Formation System

In previous sections, linear control was applied to the unperturbed nonlinear system and was shown to keep the relative motion within tolerable ranges. In the following sections, nonlinear control techniques, namely sliding mode control, will be used. Sliding mode control is robust against external disturbances as well as parametric uncertainties [56]. As such, it is advantageous to employ a sliding mode control scheme over the linear control methods discussed thus far. In this section, the nonlinear control strategies introduced in Chapter 3 will be applied to the formation system and the resulting performance will be compared to that of the linear controllers. Differences will be discussed along with the advantages and disadvantages of using nonlinear control strategies.

Applying the sliding mode control law developed in Chapter 3 to the formation system, a bounded response with steady state offset errors is observed, as seen in Figure 4.10. Gains for the sliding surfaces were determined using LQR on the partitioned system matrix. State and control weighting matrices used were

$$Q' = 3\times10^{-6}\times I_{4\times4}$$
$$R' = I_{2\times2}$$

The reaching laws and bandwidth value used were

$$\eta_{xy} = 5\times10^{-3}$$
$$\eta_{z} = 5\times10^{-3}$$
$$\varepsilon = 10^{-2}$$

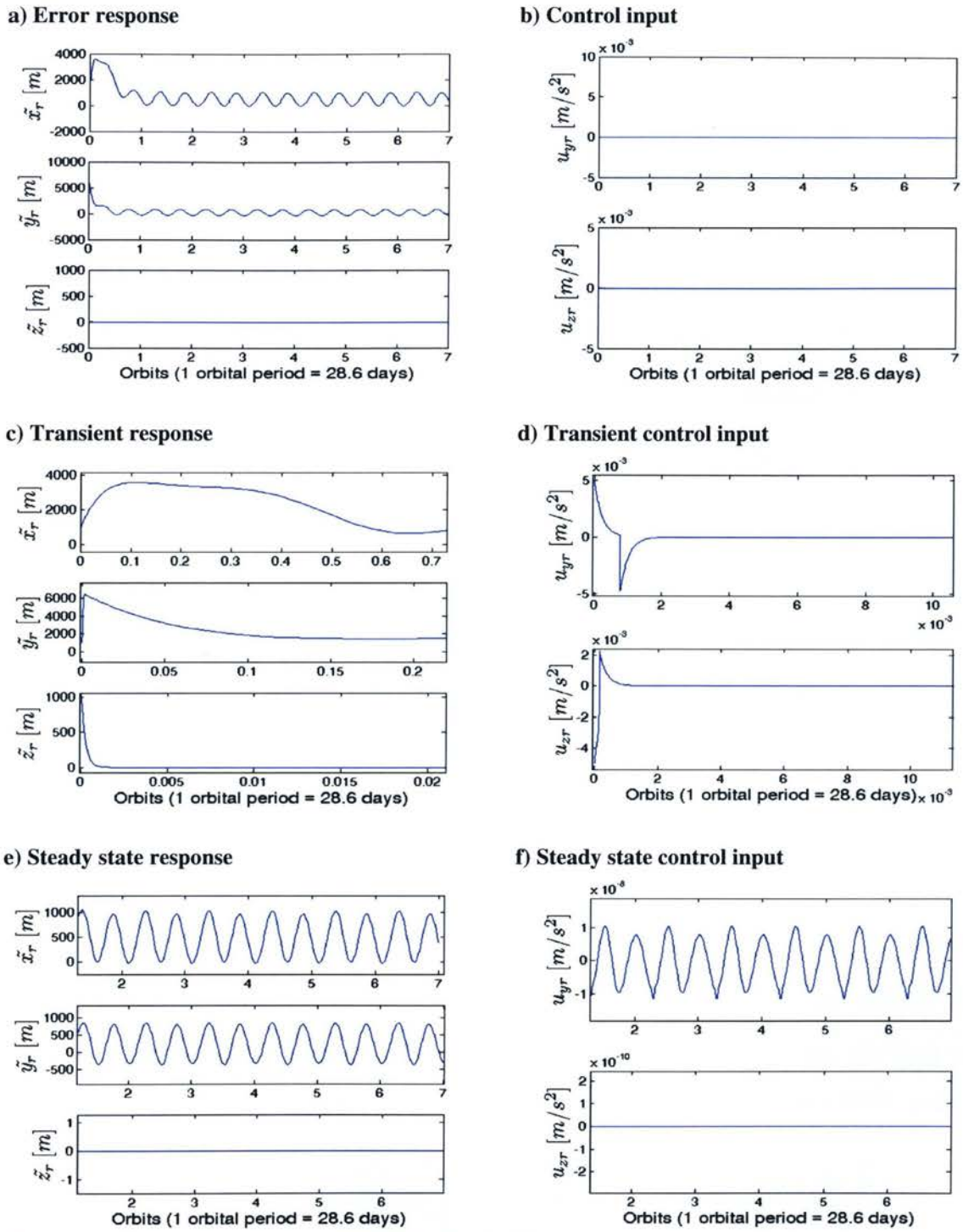

Figure 4.10 Underactuated system response using SMC

The steady state errors observed here are direct results of mismatched disturbances acting on the unactuated relative x direction. It is well known that SMC is not directly able to

handle mismatched disturbances, leading to the sliding surface values being an inadequate reflection of the state errors. The result is that the sliding surfaces are reached even though significant steady state errors exist.

It can be conceptualized that the observed errors are caused by two factors: 1) the unmatched disturbances manifesting themselves as errors to the sliding surface values, and 2) the sliding surface definitions are unable to account for errors accumulated over time. In linear control techniques, integral action can effectively eliminate steady state offset errors, although at the cost of slower system response. Eker and Akmal [58] proposed the addition of an integral term to the sliding surface definitions to improve steady state accuracy. Analogous to this, it is proposed here that an integral term be added to the underactuated sliding surface definitions in this study. As shown in Chapter 3, the sliding surfaces are redefined to be

$$S_{xy} = \dot{e}_y + K_1 e_x + K_2 e_y + K_3 \dot{e}_x + K_4 \int_t^{t+\Delta t} e_y \, dy$$
$$S_z = \dot{e}_z + K_z e_z$$

Note that integral control action was added only to the in-plane sliding surface definition. From Figure 4.10, it can be seen that there is no steady state error along the relative z axis of motion, and so integral control action is not required for the out of plane motion. K_4 here is a control design parameter. Errors in motion along the y_r rather than the x_r were integrated since actuation is along y_r. Weighting matrices and reaching laws are kept the same as that of the non integral augmented SMC scenario. With this new sliding surface definition, the in-plane control law becomes

$$\begin{aligned} u_y = &-(\ddot{y}_r - \ddot{y}_d) - K_1(\dot{x}_r - \dot{x}_d) - K_2(\ddot{x}_r - \ddot{x}_d) \\ &-K_3(\dot{y}_r - \dot{y}_d) - K_4(y_r - y_d) - \eta_1 \tanh(S_{xy}) \\ u_z = &-((\ddot{z}_r - \ddot{z}_d) + K_z(\dot{z}_r - \dot{z}_d)) - \eta_2 \tanh(S_z) \end{aligned}$$

Results for this scenario are shown in Figure 4.11.

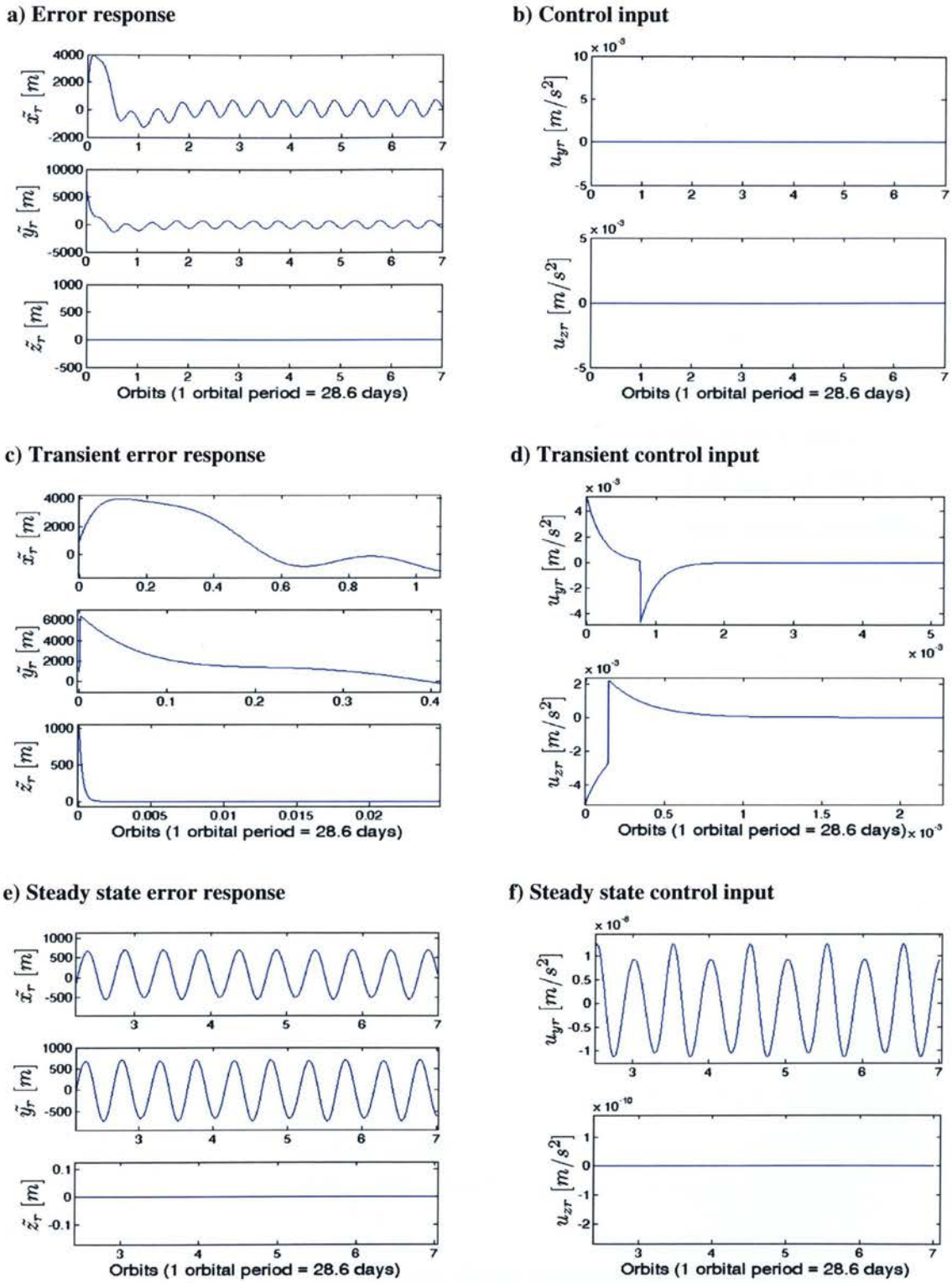

Figure 4.11: Underactuated system response using SMC with integral augmented sliding surface

The steady state behaviour is similar to that which was observed using linear controllers. Differences in system response times are due to gain selections. However, plots of the required control efforts exhibit marked differences that cannot be explained through gain selections alone. Comparing Figures 4.11 to 4.9, control inputs deduced using the linear controller appears to have the form of a smooth, continuous function, whereas with the nonlinear controller, distinct discontinuous 'peaks' are observed. This can be explained by observing the phase plots for the out of plane motion shown in Figure 4.12. The sliding surface is represented as a straight line driving the system to equilibrium state. As the system reaches the sliding surface, the controller forces the states to remain on it, resulting in the discontinuous nature of the control inputs. An analogous situation occurs for the in-plane motion. However, the coupled nature of the sliding surface definition for the in-plane motion requires a four dimensional phase plot to demonstrate the discontinuous phenomenon for in-plane control efforts; an unrealizable task.

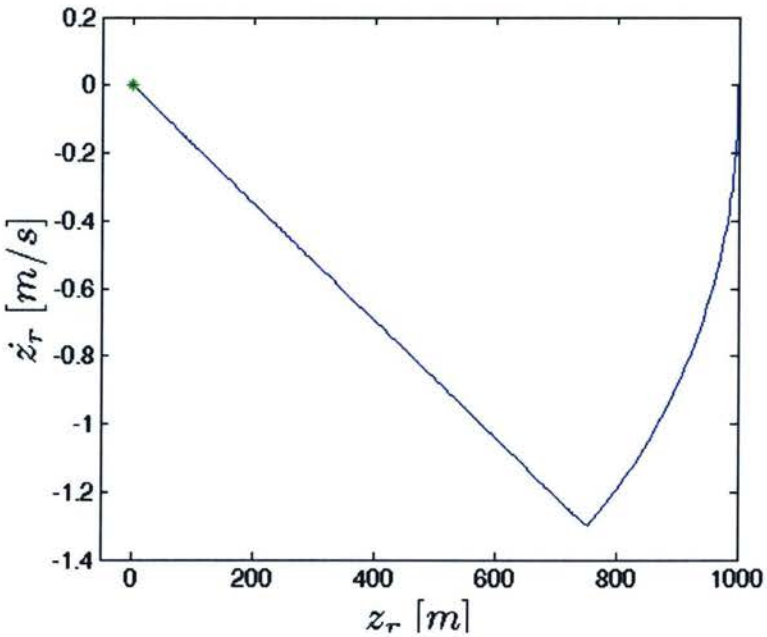

Figure 4.12 Phase plot of relative states along z axis

Continuous input is observed even after steady state was achieved. From the no control scenario described by Figure 4.3, it is readily seen that control efforts are not necessary for bounded steady state behaviour given ideal initial conditions. Hence, if the controller

is able to bring the system to a state with zero errors at some point in time, control efforts can be discontinued and bounded behaviour would still be attained. The small steady state inputs shown in Figure 4.11 serves to reduce the amplitude of the bounded motions by approximately 500 m, a small distance relative to the scale of the reference formation size. It should be restated here though that such bounded behaviour is only observed in the absence of solar gravitational disturbances.

Nonlinear Control of the Sun-Perturbed System

Thus far, control of the Sun-perturbed system has only been demonstrated using the fully actuated configuration. We now add the Sun's gravitational disturbance to the underactuated nonlinear system. The SMC with integral method was able to attain the same performance as that of a linear controller and it is assumed that it could achieve similar or better performance than a linear controller in the Sun perturbed system. Such a presumption stems from the robust properties of the SMC method which can more readily reject external disturbances.

The in-plane sliding surface definitions are augmented with integral control action to eliminate the average steady state offset error, as previously described. Initial errors are increased to 5 km along each axis so that the initial effect of the controller can be more easily distinguishable from the bounded behaviour of the system after steady state is reached. A longer simulation time period was required to illustrate the efficacy of the controller in this perturbed system. Gains are maintained to be the same values as in the unperturbed scenario. The results are shown in Figure 4.13.

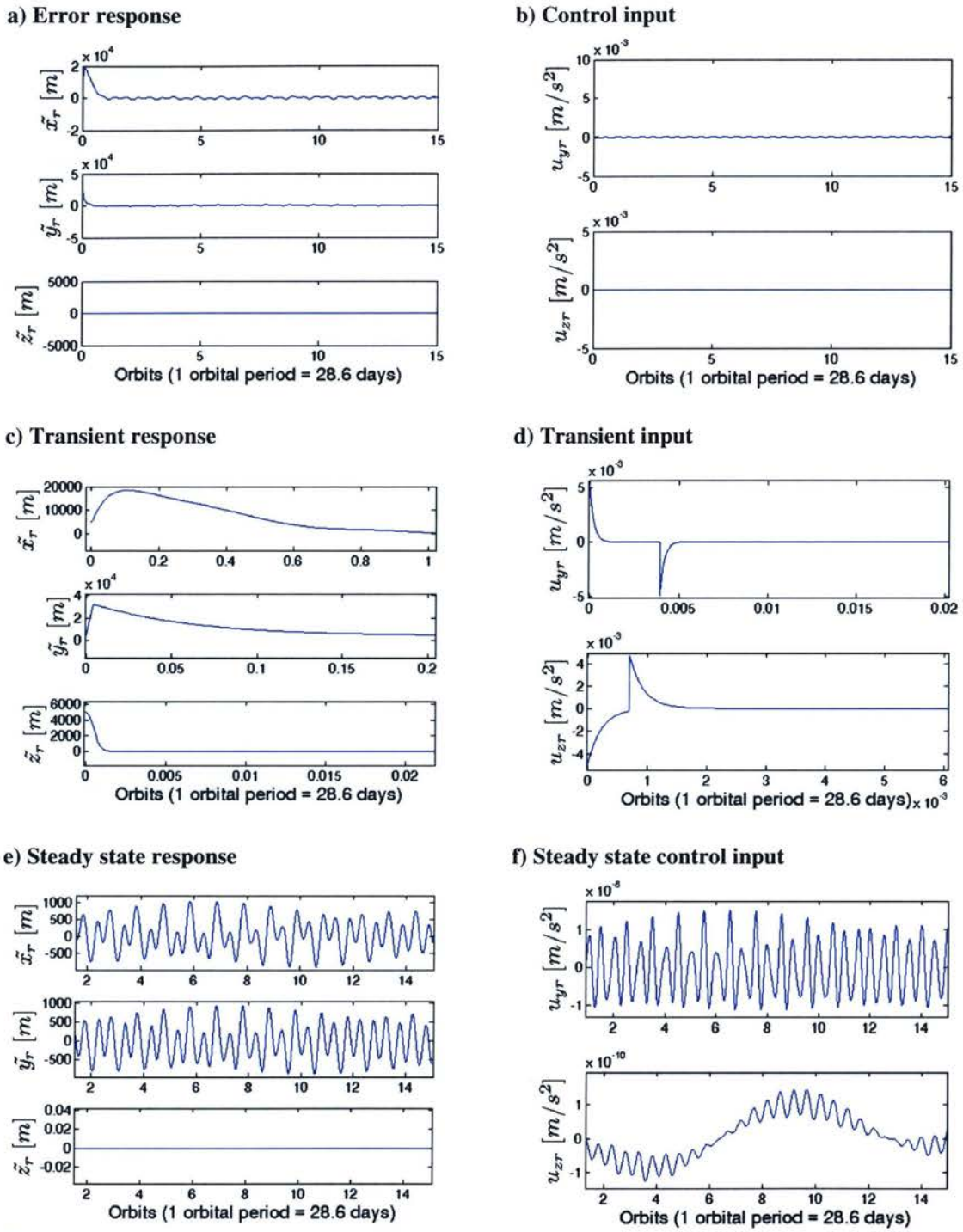

Figure 4.13 Underactuated system response in the Sun perturbed environment using SMC with integral augmented sliding surface definition

Examining the results, it can be seen that the amplitude of the bounded oscillatory motions at steady state in x_r and y_r has increased substantially under the addition of

solar gravitational disturbance. This also indicates that there may be some limitations to the ability of the sliding mode controller to rejecting unmodelled disturbances for underactuated systems. This was due to its inability to handle mismatched disturbances, as previously discussed. Solar gravity disturbance introduces additional mismatched disturbances to the system, thereby increasing the amplitude of the bounded motions. Despite this increase, the bounded nature of the motions within the ranges shown in this study can still be acceptable depending upon mission specific tolerances.

Steady state control accelerations have increased in magnitude to deal with the solar gravitational effects continually acting on the system. Due to the inclination of the Earth-Moon orbital plane relative to the ecliptic plane, the Sun's disturbing force has a component that acts in the out plane direction. However, the forces required to counter the out of plane disturbance is extremely small; accelerations on the order of 10^{-10} m/s^2. Such minute accelerations are not feasible with current propulsion technologies. Referring to Figure 4.5, it is readily seen that the Sun's perturbing force has a very minor effect on the out of plane motion; perturbing its motion by a couple hundred metres over the course of 20 orbits. As such, for station-keeping purposes, an approximate in-plane trajectory can still be achieved without relative control efforts in the out-of-plane direction.

Unlike the unperturbed case, bounded behaviour is not observed without active control since the Sun's gravity causes the system to diverge. Hence, in contrast to the unperturbed scenario, even if the controller is able to bring the system to a state of zero errors at some point in time, control is still necessary after that time to prevent the relative motion from diverging. The small scale of the control inputs required for station-keeping conflicts with the relatively larger control efforts required for formation orbit corrections. Since current propulsion technology does not permit such a diverse range of thrust outputs from one type of propulsion system, the system performance outlined in this study would necessitate a separate propulsion system to deal with formation keeping requirements.

On/Off Control of the Sun perturbed System

The control methods applied in previous sections are appropriate tools for preliminary analysis, especially since relative dynamics are generally slow. In practice, however, discontinuous control methods with tighter ranges in thruster output magnitudes could be used. To demonstrate the viability of controlling an underactuated system using discontinuous control methods, a bang-bang controller is developed and applied to the system. Bang-bang control is known to be a high frequency, discontinuous control method that is not always practical to implement. It is, however, a starting point for discontinuous control analysis and provides justification for the further development of a discrete controller for this system.

A bang-bang control law for this system is proposed as

$$u_y = -\eta_1 \operatorname{sgn}\left(S_{xy}\right)$$
$$u_z = -\eta_2 \operatorname{sgn}\left(S_z\right)$$

where the definition of the sliding surfaces previously defined are utilized here as the variable that determines the on/off nature of the controller and η_i represents the magnitude of the control acceleration. Unlike the continuous control cases, the magnitude of the control input for a bang-bang controller varies between two values only; zero and η_i for both orbital correction and formation keeping tasks. Therefore, using a bang-bang control scheme, the propulsion system used for formation keeping could also be used larger relative orbit corrections.

Figure 4.14 shows the system response using a bang-bang control scheme with $\eta_1 = 10^{-7}$ and $\eta_2 = 10^{-8}$. As with the case where a sliding mode controller was directly applied to the system, the controller's efficacy could not be immediately discerned from simulations with short simulation time spans. Although long time span simulations do not accurately represent the system's dynamics, they can serve to illustrate the controller's ability to

bring about bounded motions. Simulations are repeated with a time span of 50 orbits for this purpose and are shown in Figure 4.15.

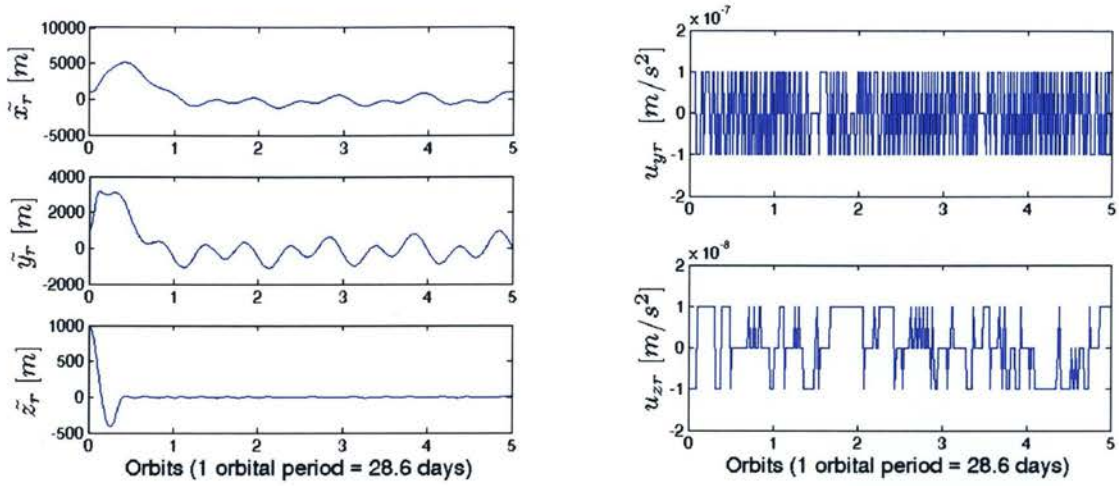

Figure 4.14 Performance of a bang-bang controller applied to the underactuated and Sun perturbed system

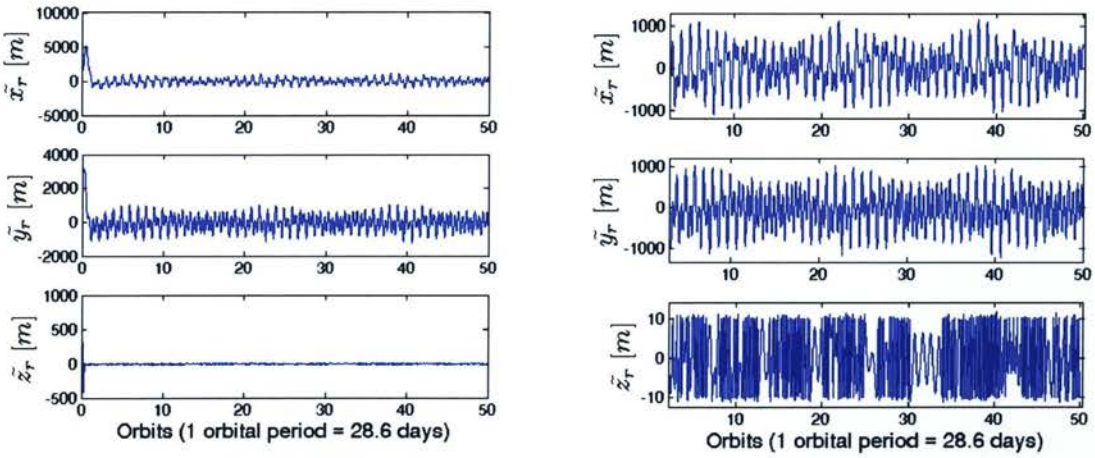

Figure 4.15 Long term simulation of the bang-bang controlled underactuated system demonstrating controller efficacy

The high frequency nature of the controller is clearly evident in the control accelerations plots. The frequency can be reduced by introducing dead zones; regions where the error state is within a specified tolerance and hence no control efforts are required. Generally, a larger dead zone results in less chattering in the control input but can increase the steady state errors. In cases where the dead zone values were too large, the controller

was unable to control the system. It was observed that using dead zone values greater than 200 m for the in-plane motions resulted in noticeable degradations in performance. Hence, the simulations here were conducted using this value for the dead zone.

The control magnitude also greatly influences the response of the system. Clearly, from previous simulations using continuous control schemes, station keeping requires much less control effort than orbital corrections. In this bang-bang control scheme, the magnitude of the control accelerations does not change, except where no control is required in which case it is zero. Large values of η_i makes station keeping difficult and also increases the amplitude of oscillatory motions at steady state.

4.4 Results and Discussion: Circular Trajectory Tracking

The elliptical relative in-plane trajectory can be considered a natural formation trajectory of the linearized three body system. The natural in-plane circular trajectory was shown by Catlin and Mclaughlin [50] to not exist. A projected circular orbit trajectory was more feasible according to their analysis, but it required the short period frequency being approximated as equal to the out of plane frequency. The control of the formation system tracking an unnatural, in-plane circular trajectory will be analyzed here.

4.4.1 Fully Actuated System

A sliding mode controller was applied to the fully actuated system tracking the relative circular trajectory. Trajectory radius was chosen to be 10 km, forming a trajectory that is comparable in size to the reference trajectory used in the elliptical cases. The simulation results are shown in Figure 4.16, from which it can be seen that station keeping control efforts have increased by 2 orders of magnitude to maintain a circular trajectory rather than an elliptical one.

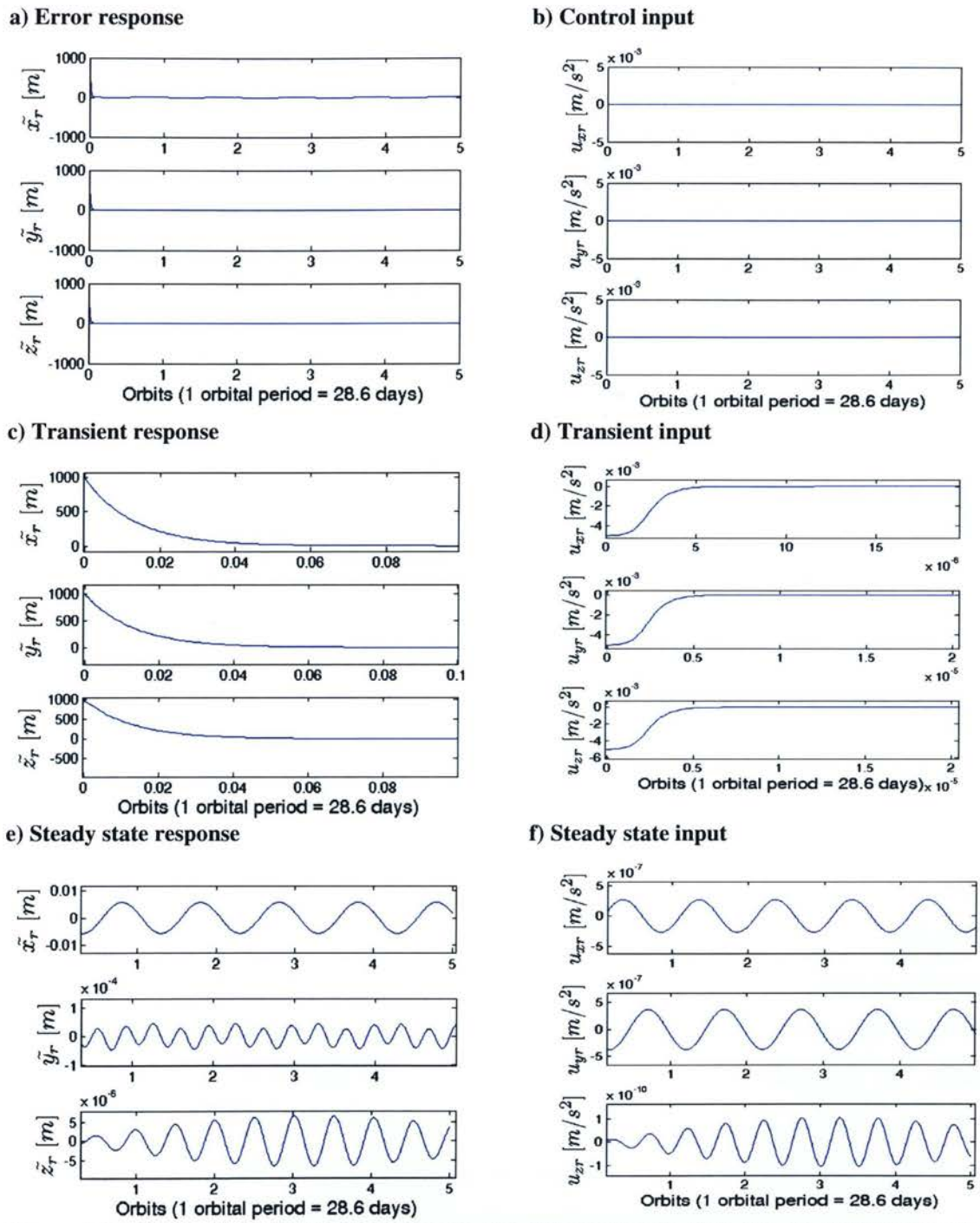

Figure 4.16 Performance of SMC applied to the fully actuated, Sun gravity perturbed system tracking a circular reference trajectory

4.4.2 Underactuated System

Applying the circular restriction to the underactuated case, it was found that an underactuated system was unable to track the circular trajectory. In Figure 4.17, it can be seen that, despite the spacecraft's best efforts to track the circular trajectory, the system is unable to do so and instead moves in an elliptical trajectory. It is reasonable to presume that tracking unnatural trajectories requires greater control efforts as its motion will be counter to the natural tendencies of the system. It may be that the circular trajectory demands a large degree of control to counter the system's natural motions. Such taxing control might only be achievable with actuation available along both in-plane axes.

From Figure 4.17, it's evident that the orbit trajectory not only becomes elliptical, but also that its size has increased dramatically. This is a result of the increased controller demands in tracking the circular trajectory acting in a low gravity, dynamically sensitive environment. In such an environment, even small increments to control efforts will have dramatic effects on the system's motion. This is exacerbated by the lack of actuation along x_r, which forces motion along x_r to be accomplished through indirect routes, further increasing the size of the orbit.

It is interesting to note that the resulting trajectory, regardless of the initial positions, consistently resembles an ellipse as it attempts to track a circular reference. The period of the ellipse is equal to that of the short period in this case, which at first glance would imply that forcing the underactuated system to track a circular trajectory would inherently cause the system to track a natural trajectory. However, a closer analysis reveals that the period of the observed elliptical path is independent of the natural periods of motion. Rather, the elliptical trajectory has a period equal to that of the reference circular trajectory. This is illustrated in Figure 4.18, where the reference circular trajectory's period is set to be half of one natural short period. The resulting motion appears to orbit with a period equal to that of the reference circular trajectory, and not of the natural short period motion.

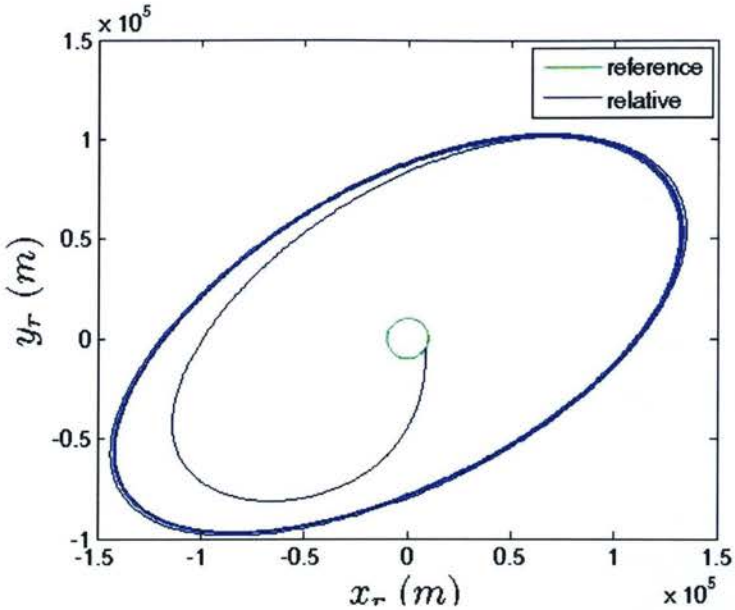

Figure 4.17 Trajectory of an underactuated system attempting to track a circular orbit

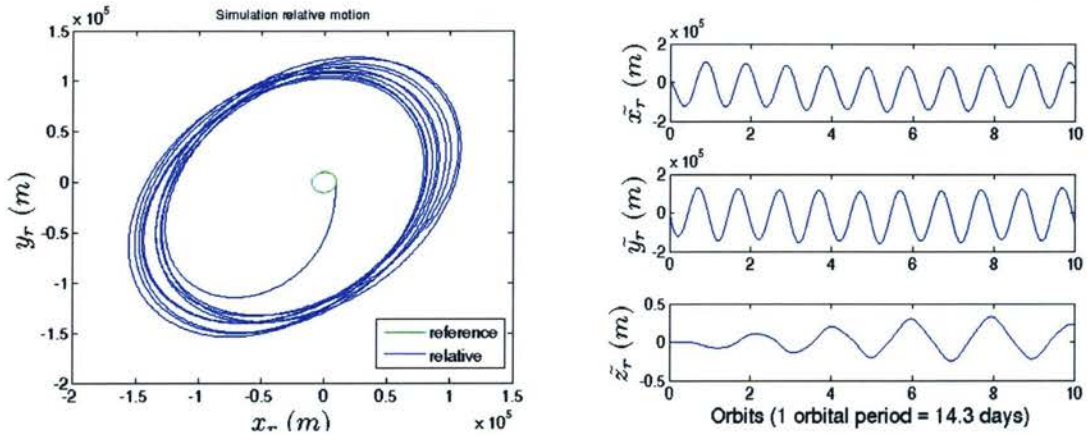

Figure 4.18 Trajectory of underactuated system attempting to track a circular orbit with a period equal to half of one natural short period

4.5 Fuel Consumption

A major criterion in the evaluation of a control strategy's effectiveness is the fuel consumption, which is directly related to the required change in velocity magnitudes. It is well known that the greater the velocity change in any maneuver, the more fuel is required. Hence, without knowledge of a system's mass, one can still gain a sense of

which control strategies are more fuel efficient simply by looking at the total velocity changes. Velocity changes for orbital correction maneuvers can vary depending on the desired response times, while gain selections could influence the control requirements for formation keeping during steady state. Since controller performance for formation keeping in each of the pertinent scenarios did not vary significantly, required fuel consumption will be analyzed for formation keeping tasks only. Table 4.2 summarizes the velocity change requirements demanded by the control methods for some pertinent scenarios. ΔV/week values are averaged values over the course of several orbits.

Table 4.2 Formation Keeping ΔV Requirements in Different Scenarios

	Actuation Status		Control Method			Reference Trajectory		Perturbations		ΔV/week (mm/s/week)
	Full	Under	LQR	SMC w/Integral	Bang-bang	Elliptical	Circular	Sun Pert.	No Pert.	
SCENARIO	✓		✓			✓			✓	1.85
	✓			✓		✓			✓	1.79
	✓		✓			✓		✓		1.95
	✓			✓		✓		✓		1.86
		✓	✓			✓		✓		4.02
		✓		✓		✓		✓		3.63
		✓			✓	✓		✓		55.43
	✓			✓			✓	✓		246.60

Given that the plots of control accelerations showed that steady state control inputs were often on the scale of 10^{-8}, it is not surprising to find that formation keeping ΔV requirements would be small in most cases. This highlights the sensitivities of the dynamics in this low gravity environment. Further exemplifying the dynamic sensitivities are the additional ΔV requirements to counter the Sun's perturbing effect. From Figure 4.5, the influence of the Sun's gravity on the relative motion is shown to be substantial. Yet, the ΔV difference between the perturbed and unperturbed case is small, demonstrating that even slight changes to the states in this system can have dramatic effects on its motion.

Since controller performance is dependent on the designed control parameters, one cannot be certain that the nonlinear controller will always outperform the linear controller. Still, in this study, the designed sliding mode control schemes consistently appeared to be more efficient at handling formation keeping tasks compared to LQR control, as can be observed by comparing the respective ΔV requirements. The bang-bang controller required the largest ΔV change to maintain a natural formation trajectory. The scale of the change is dependent upon factors such as the chosen control acceleration magnitude and trade offs between dead zone size and error tolerances. Nevertheless, of the control methods applied to the underactuated system tracking an elliptical trajectory, bang-bang control used the greatest ΔV change for station keeping tasks. Since the bang-bang controller required the most fuel for this task, this indicates that if discontinuous control methods are used, it would require far greater control efforts than those predicted by continuous controllers.

It is of no surprise that maintaining the circular formation would require the largest ΔV change of all cases. The scale of this change is more appropriately measured in 10's of centimetres per second each week, showing that tracking an unnatural formation in the three body system would place huge demands on fuel and propulsion systems.

Chapter 5

Trajectory Tracking Using Solar Sails

5.1 Introduction

In Chapter 4, relative elliptical trajectory tracking was shown to be achievable using thrusters in both fully actuated and underactuated configurations. The simulations showed that the control efforts required for orbit corrections were small, but was still on the order of 10^5 times larger than that required for station-keeping. Since most current propulsion systems do not have such a diverse range in their output magnitudes, this implied the need for a separate propulsion system to handle station-keeping tasks. A bang-bang control scheme allowed the use of station-keeping propulsion systems for reconfiguration tasks as well, but the high frequency of control input is not fuel efficient.

In the presence of solar gravitation, station keeping control efforts were continually needed to keep errors bounded to within a nominal tolerable range of a couple of kilometres. Both long burn times and sustained control efforts would rapidly consume onboard propellant reserves, reducing a mission's lifespan. Clearly, there are severe drawbacks to relying on an underactuated thruster system for formation control.

A novel method for circumventing fuel constraints would be to use solar sails. Accelerations imparted by solar radiation forces can be manipulated through adjustments

to the relative yaw and pitch angles of the solar sails. Appropriate angle adjustments can provide the necessary differential SRP forces for control purposes.

Using solar sails for control can overcome some of the aforementioned challenges faced by a thruster control system. Firstly, control using solar sails does not consume onboard fuel. Used as a failure mode control system to be activated in the event of a primary propulsion system fault, this would conserve onboard fuel to be used for mission critical maneuvers, thereby helping to salvage a mission. It could also extend the life of an otherwise shortened mission caused by such failures. Secondly, SRP is continually acting on the system, but the force it imparts is adjustable through changes to the sail orientation. This means that continuous control profiles with larger ranges in control accelerations are realistically attainable. Hence, orbit correction maneuvers, which require larger control accelerations, and station keeping tasks can be accomplished using solar sails alone.

In this chapter, the use of solar sails for elliptical trajectory tracking is explored. Since there are only two input angles dictating the motion of this three degrees of freedom system, the system is underactuated. A further constraint is introduced with using SRP; resulting control accelerations can only act in directions away from the Sun. This differs from the thruster scenario where this limitation did not exist. As is usually the case, additional constraints will likely hinder the performance of the controller. Therefore, it is reasonable to expect that the response of a system controlled using solar sails will be inferior to those attained by thruster control. Furthermore, since an underactuated thruster system was unable to achieve unnatural in-plane circular formations, an underactuated system using solar sails for control will not be able to accomplish this task either. Hence, all results presented in this chapter will pertain to the relative elliptical formation case. A linear controller is first applied to both the linear and nonlinear system. Comparisons will be made between the system responses observed here and the thruster-controlled cases. A bang-bang controller is then introduced as a possible nonlinear control strategy using SRP.

5.2 Control of the Linear System Using Linear Control

As with the thruster control scenarios, a linear controller is first applied to the linear system to gain a better understanding of the dynamics of the system. Recall that in the development of the linear controller shown in Chapter 3, small angle restrictions were imposed in order to simplify the relative SRP model. If the simplified representation of the SRP effect given by Equation (3-40) is to be used directly in the plant model, then the control angles must adhere to the small angle criterion. This restriction is in addition to the directional constraint on control accelerations mentioned in the introduction. Figure 5.1 shows the simulated response of the dimensionalized, unperturbed linear system controlled using a LQR control scheme with SRP providing the control accelerations. The state and control weighting matrix values used for this simulation were

$$Q = 3\times10^{-10}\begin{bmatrix} 1 & 0 & 0 & 0 & 0 & 0 \\ 0 & 1 & 0 & 0 & 0 & 0 \\ 0 & 0 & 200 & 0 & 0 & 0 \\ 0 & 0 & 0 & 1 & 0 & 0 \\ 0 & 0 & 0 & 0 & 1 & 0 \\ 0 & 0 & 0 & 0 & 0 & 1 \end{bmatrix}, \qquad R = \begin{bmatrix} 1 & 0 \\ 0 & 1 \end{bmatrix}$$

The area to mass ratio used for this simulation was 0.01 m^2/kg. The relative input angles are limited to being less than 15 degrees. Relative initial offset errors of 1 km in each axis are included to assess the controller's ability to perform orbit correction tasks.

Figure 5.1 clearly shows that the errors tend to zero with time, indicating that SRP can be used to control the formation system of interest in this study. Comparing the results to those of the thruster-controlled linear system of Chapter 4, it is evident that the settling time has increased substantially, requiring that the simulation time be lengthened. The errors were reduced to within hundreds of metres within a few orbits; sufficiently accurate enough for many mission scenarios. However, such long settling times may be too lengthy depending on mission requirements.

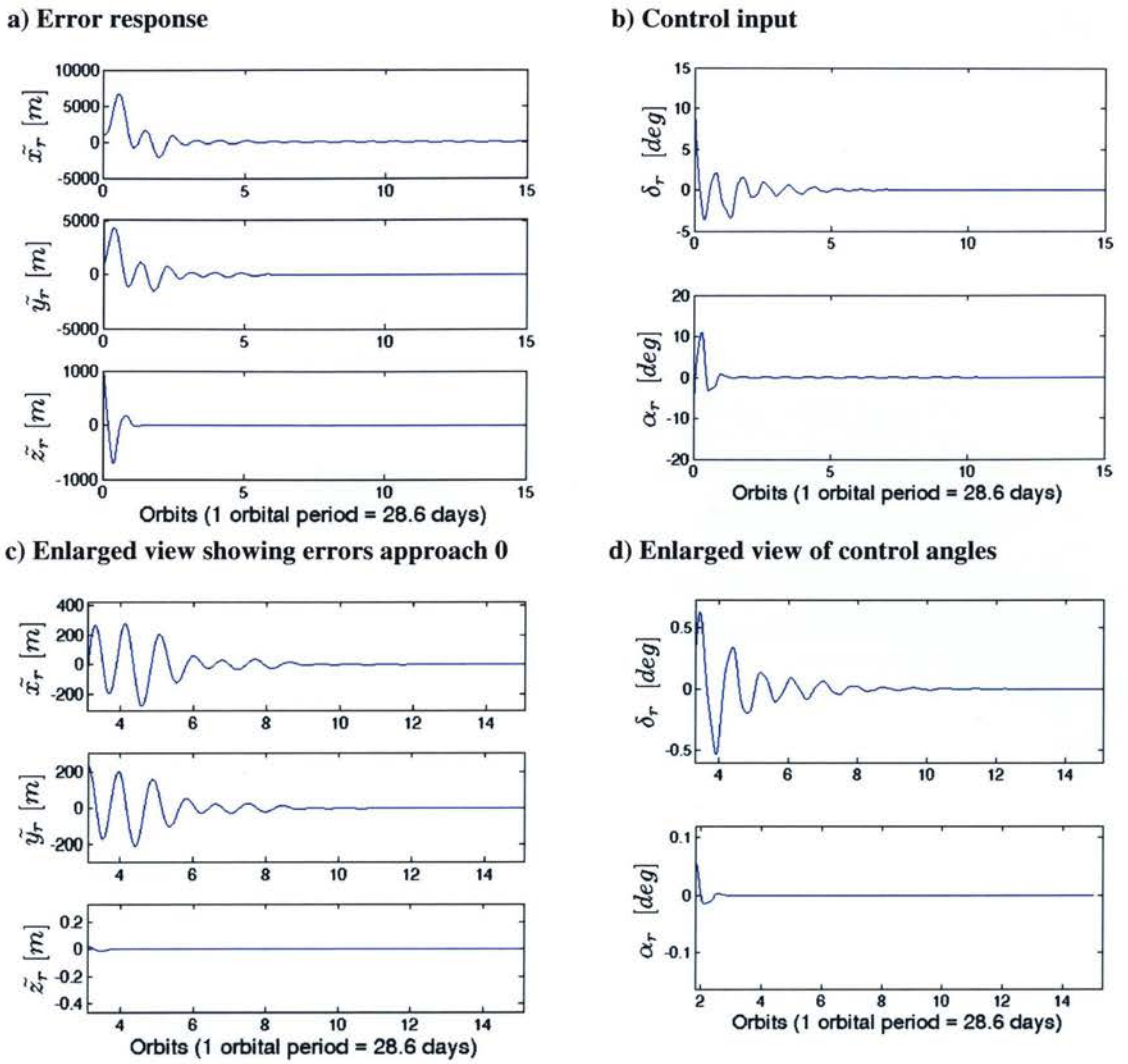

Figure 5.1 Performance of LQR control scheme on the linearized system using small relative sail angles

In the thruster-controlled setting, gains could be adjusted to induce better controller performance, so long as the control accelerations remained reasonably attainable using thrusters. In the solar-sail-controlled system, gain adjustments altered the relative control angles to ranges outside of that valid for small angle approximations, which are required for simulations involving the linearized system using the simplified SRP model. The plots shown here represent the best efforts of the designer to attain control while adhering to the small angle restrictions.

5.3 Control of the Nonlinear System Using Linear Control

As was done for the thruster control case, the linear controller using SRP is applied to the nonlinear system to assess how effectively it could handle the nonlinearities. Bounded system errors could not be demonstrated with a simulation time frame of 15 orbits. The results shown in Figure 5.2 were obtained using a simulation time of 50 orbits.

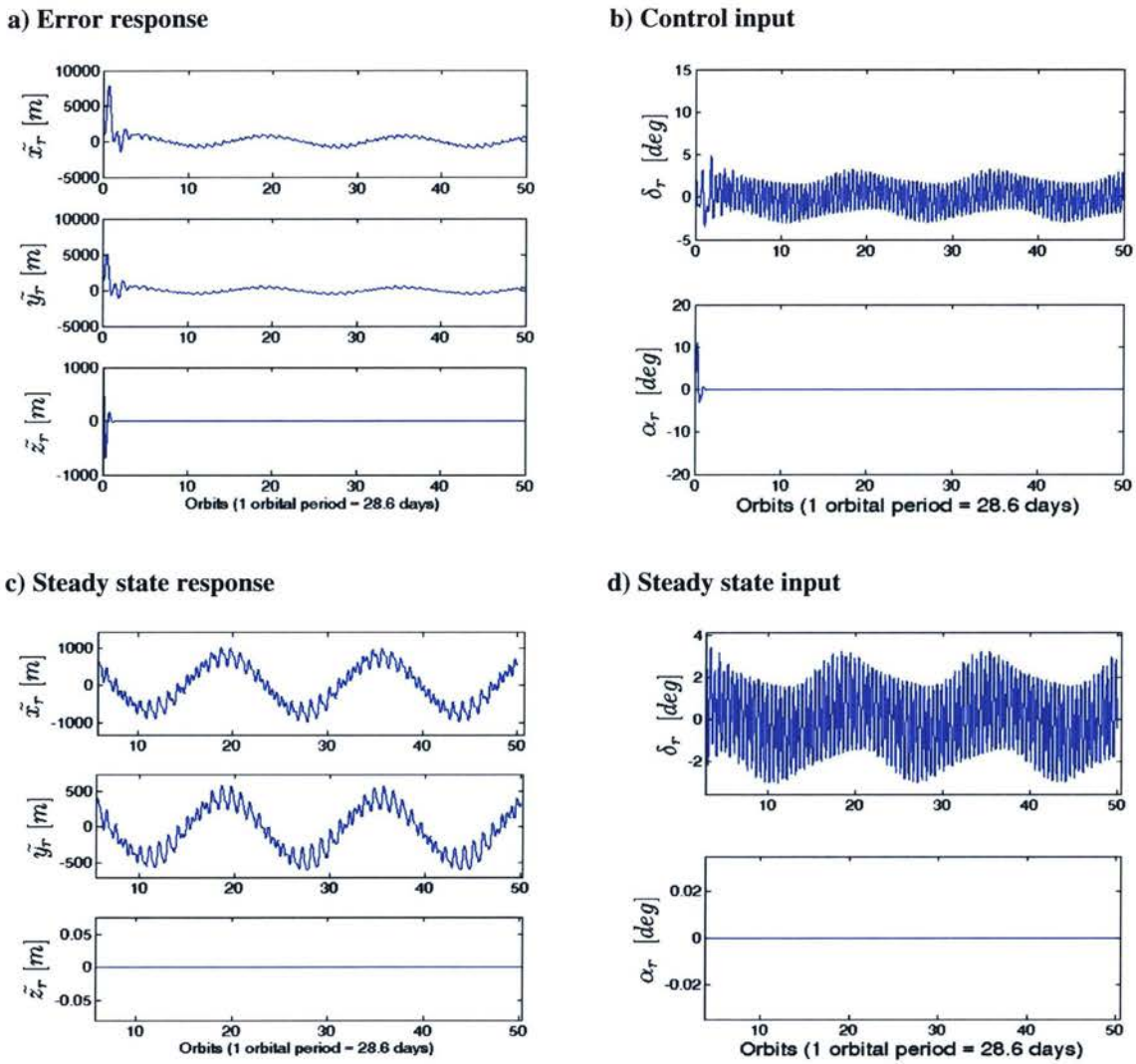

Figure 5.2 Performance of a LQR controller applied to the nonlinear system using solar sails for control actuation

Long simulation time periods undoubtedly produces results with a higher degree of numerical errors. As such, the results presented here should be viewed as very crude approximations of the system behaviour at best. In spite of this, Figure 5.2 shows

bounded performance with long time periods of oscillation, demonstrating the effectiveness of the controller. Such oscillations are caused by the nonlinearities, yet they are not seen in the results of the thruster controlled cases. Fine tuning of the gains did not appear to significantly improve the performance and observed behaviour.

The long periods of oscillation can be explained by the directional constraint on the control acceleration. When nonlinearities cause the relative motion to drift in directions away from the Sun, the ideal control acceleration would be in the sunward direction to counter the undesired motion. This is more readily achievable using thrusters, causing higher frequencies of oscillations to be observed in the thruster controlled case as changes in thrust direction causes accelerations in the opposite direction. Solar sails, however, are not able to generate thrusts in directions towards the Sun. Motion sunward is achieved by reducing orbital velocity over extended periods of time and dropping to lower orbits about the Sun. This is a more time consuming and much less direct method than using thrusters to accomplish the same task. Since the solar sails are unable to compensate for these nonlinear disturbances in a timely manner, long periods of oscillations are observed.

It appears that the in-plane steady state relative motions are bounded to about 500 m in x_r and y_r. These bounds are similar to that of the thruster controlled case shown in Chapter 4, implying that a solar sail controlled system could attain comparable performance to that of a thruster-based system.

Although not illustrated here, it should be noted that small angle restrictions are only necessary for simulations involving the linearized plant model using the simplified SRP model given by Equation (3-30). In simulations employing the full nonlinear plant model, small angle considerations are not necessary. In the nonlinear model, relative control angles are substituted back into the full expressions for relative SRP accelerations given by Equation (3-39). These nonlinear expressions are valid regardless of the magnitudes of the angles. Hence, even though the control laws were derived using small

angle approximations, controller outputs could still be large and would remain valid in the nonlinear system simulations.

5.4 Control of the Nonlinear System Using Nonlinear Control

In previous chapters, sliding mode control was effectively applied to the underactuated, thruster-controlled system. However, singularity issues make the development and application of the SMC method to the solar-sail-controlled system difficult. This implied the need for an alternative nonlinear control scheme if solar sails are to be used.

From plots of the relative control angles in Figure 5.2, it can be seen that bounded performance can be achieved using small relative angles, although this condition was not necessary for simulations pertaining to the nonlinear model. What is also readily seen is the control effort continually alternating between positive and negative values at a relatively high frequency, resembling that of a bang-bang controlled system. Hence, it is conceivable that the bang-bang control method could provide tolerable system performance.

The bang-bang controller developed in Chapter 3 is applied to the nonlinear system here. The control laws can be expressed in an identical form to those of the thruster-controlled case,

$$u_y = -\eta_1 \operatorname{sgn}\left(S_{xy}\right)$$
$$u_z = -\eta_2 \operatorname{sgn}\left(S_z\right)$$

Here, $\eta_{1,2}$ represent the magnitudes of δ_r and α_r. The definitions of the sliding surfaces remain the same as previously defined and are used as the switching control variable. To prevent excessive control efforts which would result in chattering, a dead zone of 10 m in the motion along y and z were imposed. Simulation results are shown in Figure 5.3. As with the linear controller case, long simulation time periods were necessary to highlight

the bounded nature of long period disturbance oscillations. However, due to the high frequency switching nature of bang-bang controllers, relative angle plots are not very illuminating when generated over such long simulation time periods. Therefore, Figure 5.3 will demonstrate the efficacy of the controller, but plots of the relative control angles will only be shown for simulations with shorter time spans.

a) Error response **b) Steady state response**

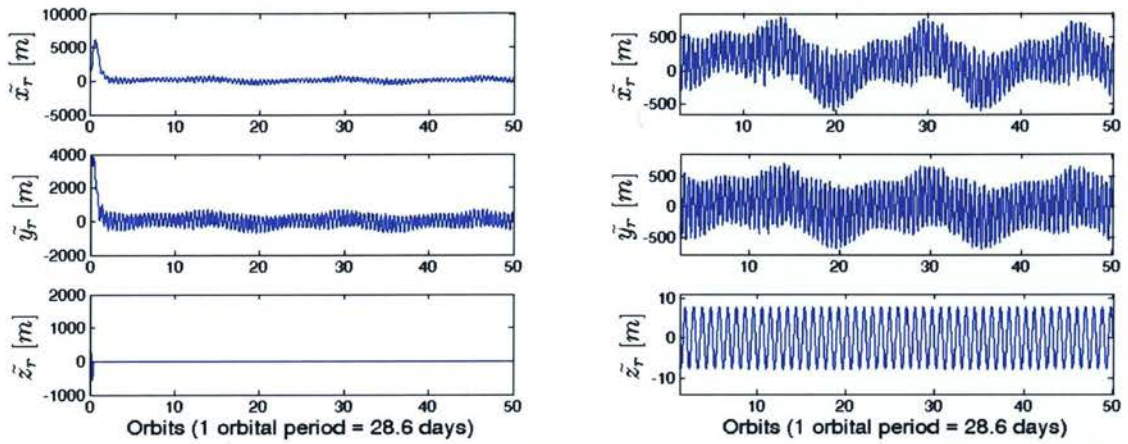

Figure 5.3 Long term simulation of the performance of a bang-bang controller, illustrating controller's ability to bound state errors

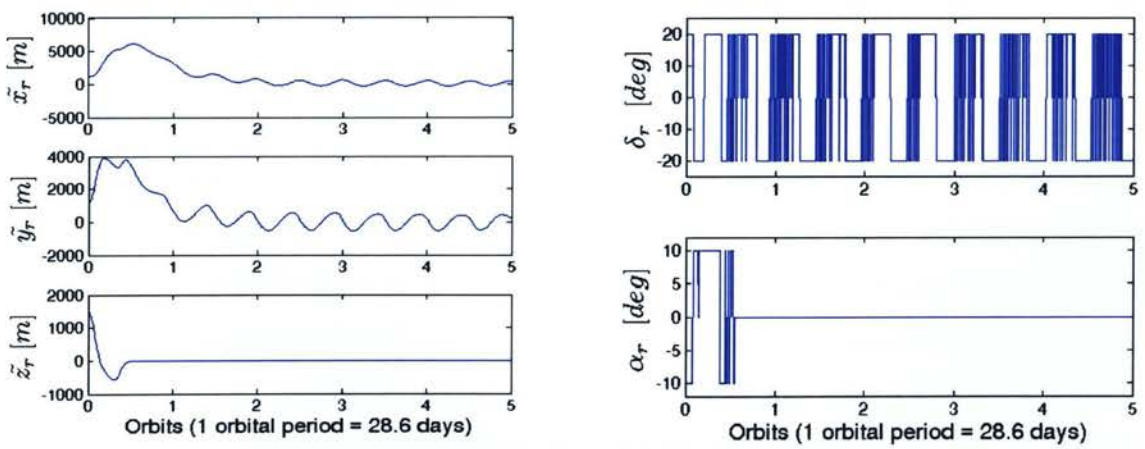

Figure 5.4 Performance of the bang-bang controller over 5 periods

The bang-bang controller appears to be able to bound in-plane motions to within 1 km. This is larger than what was achieved using the linear controller. However, there are some distinct advantages to using a bang-bang control scheme. Continuous controllers demand nonstop motor actuations and fine increments in angle adjustments once steady

state is reached. Such fine adjustments are difficult to achieve and complicate system designs. A bang-bang controller outputs angles that are more readily achievable, and its on/off nature allows for intermittent usage of actuation devices, conserving power.

In comparison to the corresponding thruster-controlled scenario, similar performances were attained using solar sails with less control switches overall. As with the thrusters controlled cases, bounded oscillations were observed. These were due to nonlinearities that could not be directly countered in a timely manner by the underactuated system. In time spans where high frequency switching is observed, such as between 4 – 5 orbits, such inputs may not seem to be practically realizable owing to limitations in the slew rate. This, however, proves to be a mute point owing to the size of the simulation time step.

The simulation was conducted with a time step of about 5 hours. Improvements in numerical accuracies and controller performance were observed to be marginal with smaller step sizes. Relative control accelerations are treated by the simulation as being constant during a time step interval and integrated. In general, maintaining a constant relative control angle does not result in constant control accelerations since the direction of the Sun vector will change. However, over time intervals that are relatively small compared with the orbital period, the formation system's position does not change greatly from its previous time step position. Since the Sun's direction vector is largely determined by the system's position, it follows then that the Sun's direction vector does not vary significantly either. Therefore, over that short time interval, approximately constant control accelerations are obtained by maintaining a constant relative angle. With this in mind, a nominal slew rate parameter of 0.05 deg/s would allow the transition time between control angle changes to be less than 15 minutes in this case; an insignificant amount of time relative to the time step size and therefore making the use of a bang-bang controller on a solar-sail-controlled system plausible.

5.5 Control of Sun Perturbed System

In the unperturbed, thruster-controlled scenario, the sliding mode controller was able to attain similar performance results as the linear controller. Since SMC is a robust nonlinear control method, it was reasonable to presume that the sliding mode controller would outperform the linear controller in a perturbed dynamic system. The same line of reasoning cannot be extended here to the solar sail controlled system, however.

The simulation results thus far in this chapter show that both a linear and nonlinear controller can effectively bound system errors. The linear controller provided better performance than the bang-bang controller but required constant motor actuations and fine angle adjustments. Since the linear controller outperformed the nonlinear controller, it was necessary to analyze the performance of both controllers in the Sun perturbed scenario.

5.5.1 Linear Control of the Sun Perturbed System

The performance of the linear controller is shown in Figure 5.5. Although clearly able to bound steady state motions, the maximum amplitude of the oscillations was almost 4 times that of the unperturbed case; despite best efforts to reduce this through tuning. The long expanding and contracting trends are similar to that which was observed in the Chapter 2 in dynamical simulations of an uncontrolled mass. Such trends are caused by the changing direction of the Sun vector as the Earth-Moon system and the satellite formation system orbits the Sun, causing an oscillating disturbance along each axis. Out-of-plane motions are small and negligible, but are maintained using unattainably small relative angles. Larger out-of-plane motions would be observed in a true model where the accuracy and scale of the relative pitch angles are limited by the precision of actuation devices.

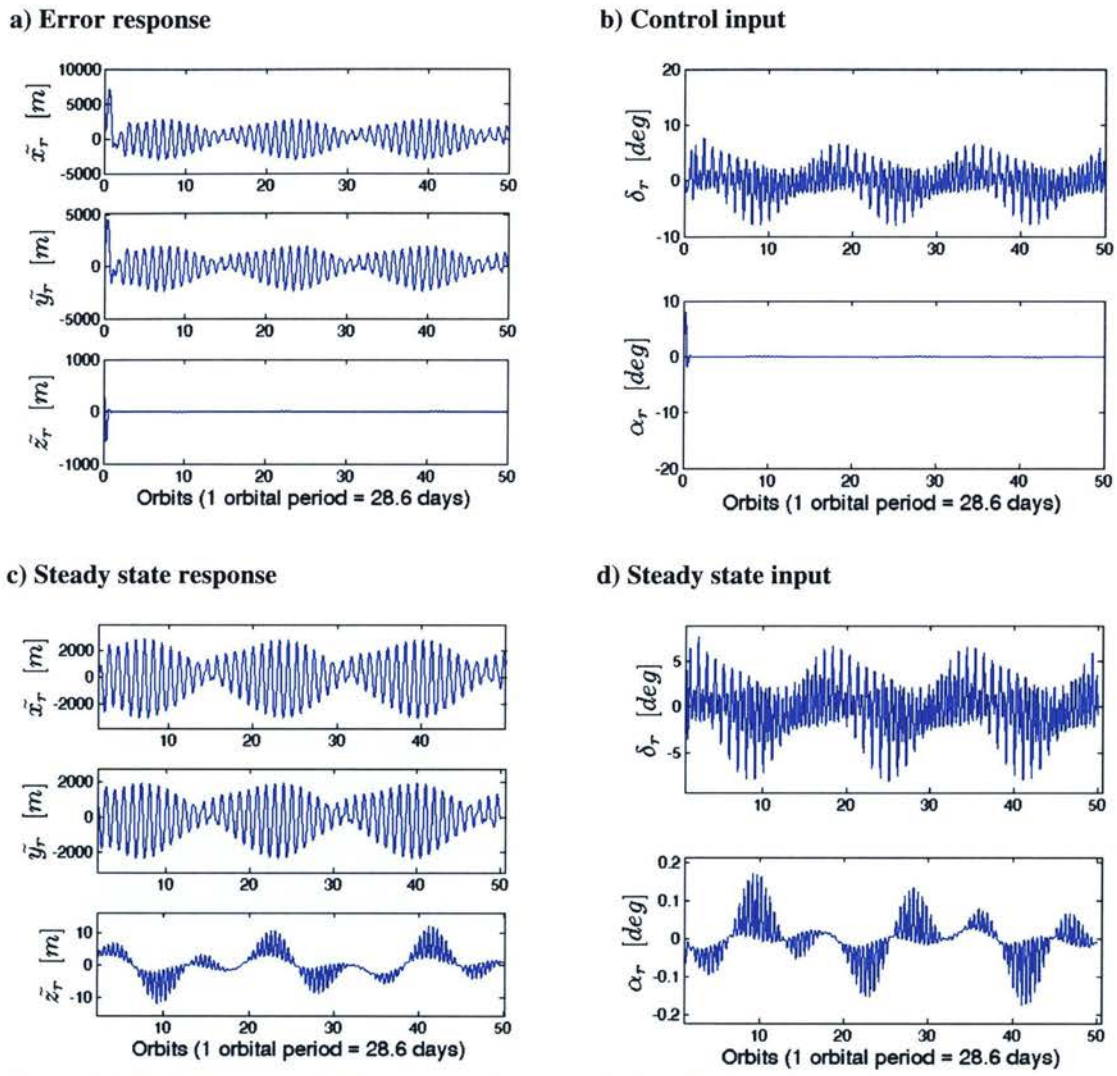

Figure 5.5 Performance of LQR control scheme applied to the Sun gravitationally perturbed system using solar sails

5.5.2 Nonlinear Control of the Sun Perturbed System

The bang-bang controller is now applied to the solar gravitationally-perturbed system. As was done for the unperturbed case, the system response during lengthy simulation time frames are presented first in Figure 5.6 to highlight the controller's ability to induce bounded motion in the presence of long period disturbances. More accurate shorter time frame simulations are then presented with the relative control angles in Figure 5.7.

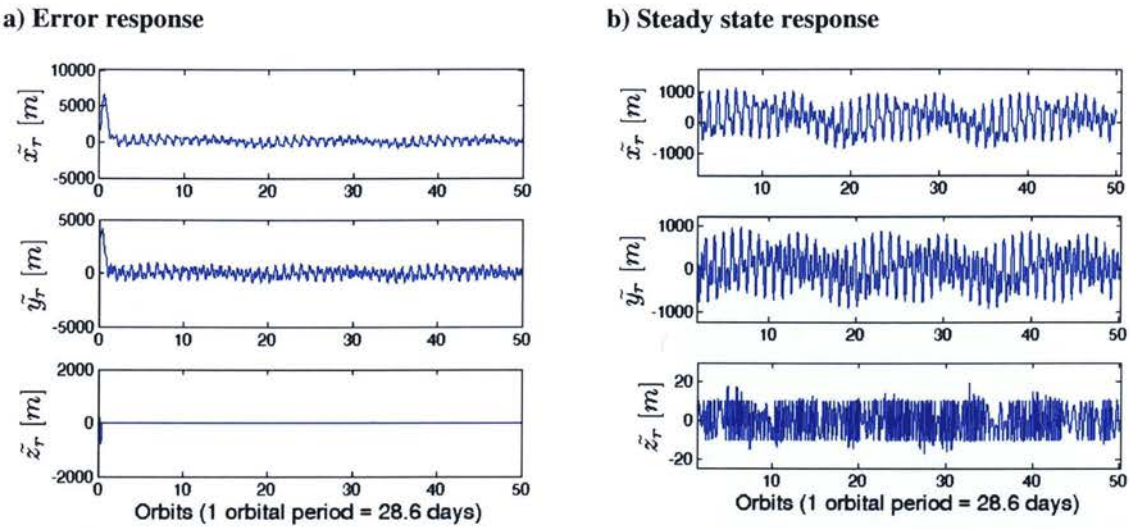

Figure 5.6 Long term simulation demonstrating the efficacy of a bang-bang controller applied to the Solar gravitationally perturbed system

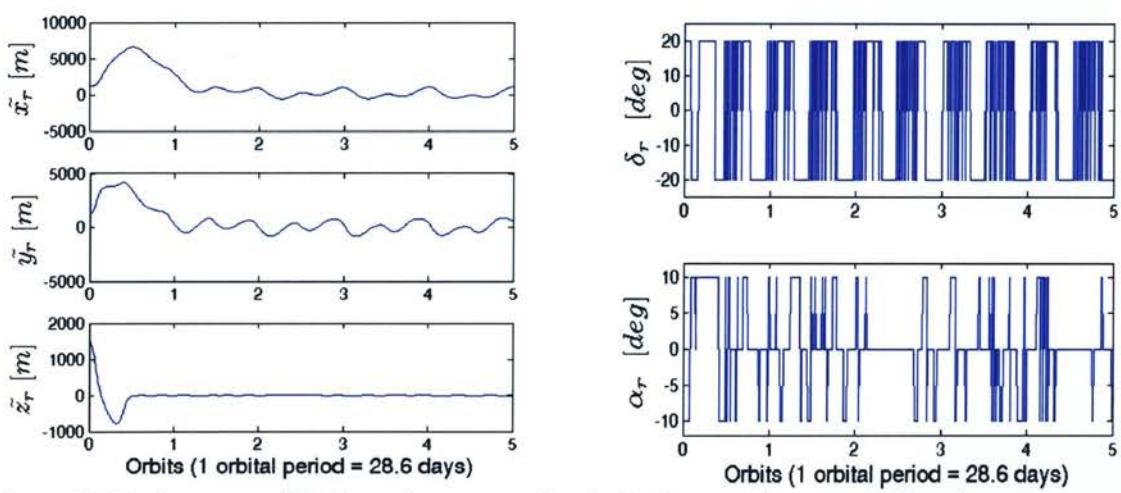

Figure 5.7 Performance of the bang-bang controller in the Sun gravity perturbed environment

From Figure 5.6, it can be seen that the Sun introduces both long and short perturbation cycles to the system. Steady state motion amplitudes increased slightly from the unperturbed case but were still around 1 km. A considerable increase in the frequency of the control effort is observed. In particular, relative pitch angle adjustments were intermittently required during the simulation. This is in contrast to the unperturbed case where the required relative pitch angle remained at 0 degrees after steady state was attained. The need for continual relative pitch angle adjustments stems from the

inclination of the reference orbital plane relative to the ecliptic. The Sun's disturbance will have an out-of-plane component in this case, which requires regular adjustments from the sail's pitch angle to counter.

Comparing the performance of the linear and nonlinear controllers, the bang-bang control scheme appears to perform better. The improved performance over the linear control scheme in a perturbed environment could be due to the robustness properties of the nonlinear controller. Its effectiveness in rejecting external disturbances can be seen by comparing the results of the perturbed to unperturbed scenarios, where the amplitude of the motions during steady state did not increase greatly. However, due to uncertainty in the tuning controllers, one cannot generalize that the nonlinear controller developed here will always outperform linear controllers.

Chapter 6

Control Using a Hybrid Propulsion System

6.1 Introduction

Previous chapters discussed the application of using thrusters or solar sails for relative control of an underactuated formation system. It was shown that the nonlinear controllers developed in this study performed better than the linear controllers in the Sun perturbed environment. In-plane motions were bounded within acceptable ranges for many prospective formation missions while out of plane motions were negligible. Due to the sensitivities of the dynamics, modelling uncertainties and numerical errors, emphasis should not be placed on the bounded values determined using long simulation time spans, but rather on the overall qualitative performance of the controllers. What was clearly evidenced in the results presented in previous chapters was the efficacy of an underactuated system in bringing about tolerable system behaviour. This would be useful in the event of faults in the primary propulsion system.

It was shown in Chapter 4 that a fully actuated thruster-controlled system using a sliding mode control scheme could perform extremely well in the Sun-perturbed environment. Unfortunately, the same cannot be said about a solar-sail-controlled system, which is inherently underactuated and constrained by its inability to directly influence motion

toward the Sun. Since the underactuated thruster-controlled system is less constrained than the solar sail controlled system, its performance represents the upper limit of that achievable by solar sails. In spite of this, Chapter 5 showed that using a nonlinear controller, a solar sail controlled system could still enforce bounded steady state behaviour in ranges similar to that achieved by an underactuated thruster system. However, neither the underactuated thrusters nor solar sail controlled systems were able to maintain the unnatural in-plane circular formation configuration. Since a fully actuated thruster-controlled system was able to track a circular formation trajectory, it was conceivable that a hybrid propulsion system, using a combination of thrusters and solar sails, could provide the full actuation needed for formation-keeping of unnatural orbits. Such a system would still reap the benefits of using solar sails; namely, the propellantless nature of solar sail propulsion systems. The hybrid system in this study will make use of thruster control along x_r while motion along y_r and out of plane motions are controlled by solar sails.

A preliminary analysis on the feasibility of a hybrid propulsion controlled system will be presented in this chapter. Linear control will be applied to the unperturbed spacecraft formation system first, to assess its ability to handle system nonlinearities. It will then be applied to the solar gravitationally perturbed system. Finally, an attempt is made to use a linear controller to track a relative circular trajectory. Once again, long simulation time periods are conducted and serve only to illustrate the effectiveness of the controller.

6.2 Elliptic Trajectory Tracking

6.2.1 Control of the Unperturbed System

To assess the ability of a hybrid propulsion system in countering the undesired motions caused by nonlinearities, it was necessary to conduct analysis on the unperturbed system. A LQR control scheme with integral control was used to track the elliptical short period trajectory. The results are shown in Figure 6.1. Bounded behaviour is clearly observed

in all axes but the steady state error in motion along the y axis never reached zero. This was due to the coupling of the in-plane motion equations as well as the inability for solar sails to dictate the magnitude of the control accelerations directly. Accelerations imparted by the thrusters not only influences motion along x_r but also along y_r. Since solar sails are not able to provide the ideal accelerations necessary to complement the effects of the thrusters for precise in-plane control, some degree of error will persist, resulting in the steady state errors observed in y_r. The oscillating trends along x_r is due to the linear controller being unable to completely compensate for the nonlinearities of the system.

In comparison to the fully actuated thruster-controlled scenario, steady state motions were bounded to larger regions. This was also due to the aforementioned limitations of solar sails and linear control methods. Compared to the underactuated cases though, it was able to drastically decrease the bounded motion amplitudes from a scale of several hundred metres to tens of metres. Thrusters accelerations during steady state were on a scale similar to that of the fully actuated case, while relative control angles remained small. The simulation results presented here were obtained using the nondimensionalized model, with the state and control weighting matrices used in the LQR control set as

$$\bar{Q} = 10^6 \begin{bmatrix} 5\times10^3 & 0 & 0 & 0 & 0 & 0 \\ 0 & 1 & 0 & 0 & 0 & 0 \\ 0 & 0 & 1 & 0 & 0 & 0 \\ 0 & 0 & 0 & 5\times10^{-5} & 0 & 0 \\ 0 & 0 & 0 & 0 & 1 & 0 \\ 0 & 0 & 0 & 0 & 0 & 3\times10^4 \end{bmatrix}, \qquad \bar{R} = \begin{bmatrix} 1 & 0 & 0 \\ 0 & 1 & 0 \\ 0 & 0 & 1 \end{bmatrix}$$

As was done in previous cases where control was achieved using solar sails, small angle approximations were used to facilitate the determination of the relative control angles. These angles were then substituted into the nonlinear expression of the SRP effects. The control effort along x_r was a sum of the SRP component acting along that axis and the thruster acceleration.

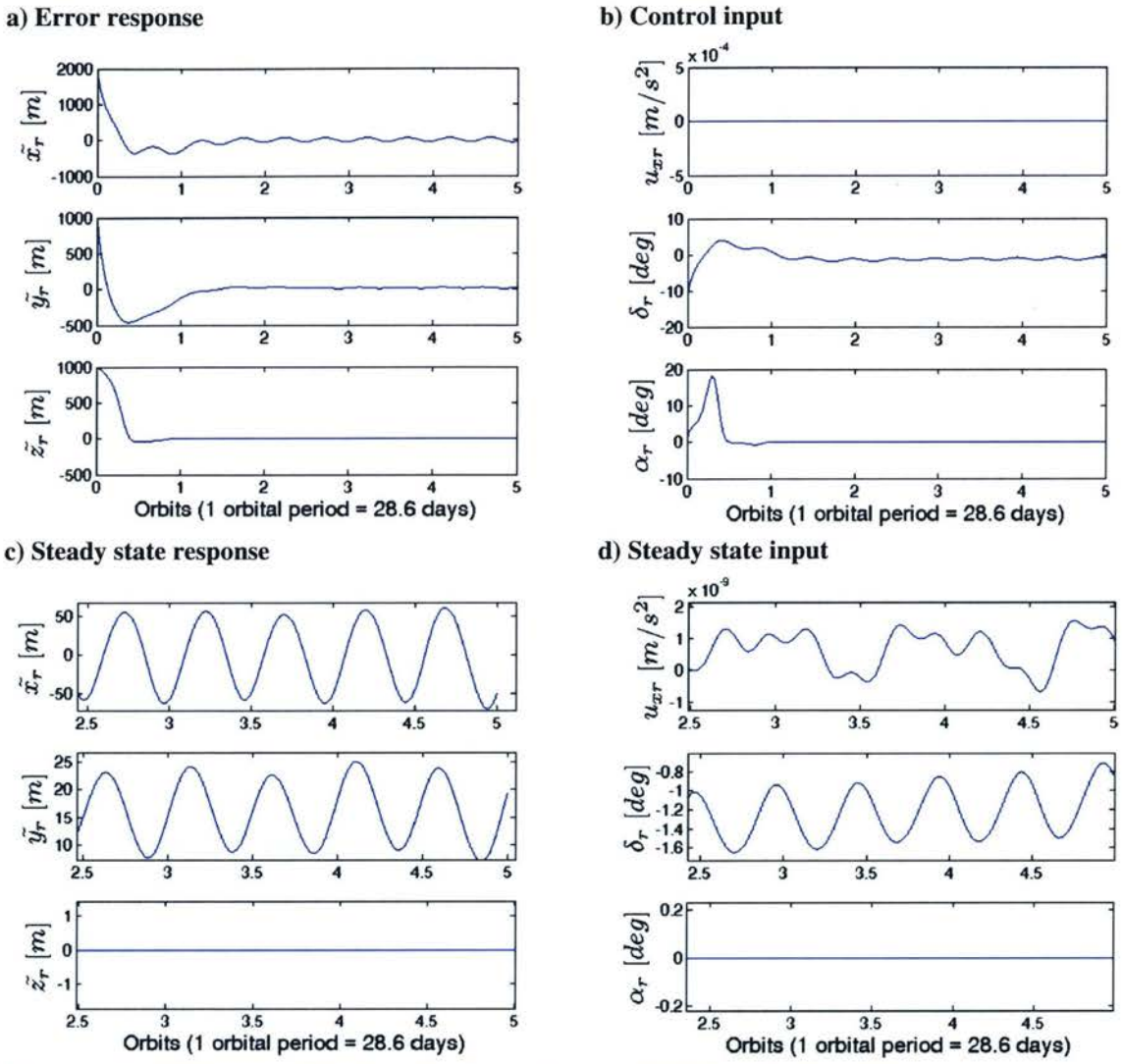

Figure 6.1 Performance of linear controller on the unperturbed nonlinear system

6.2.2 Control of the Sun Perturbed System

Simulation results for the Sun-perturbed hybrid system are shown in Figure 6.2. As with the solar sail controlled cases, long simulation periods are used to illustrate the efficacy of the controller.

Although the numerical accuracy of long term simulations is crude at best for this system, some general observations of the controller's performance can still be drawn. Bounded

steady state motions are still observed, but the amplitude of the oscillations has increased. This increase results from the linear controller being unable to fully compensate for the Sun's disturbance. This is analogous to what was observed in the solar sail controlled scenarios, where a nonlinear controller provided superior performance to the linear controller in the presence of the Sun's perturbation. Nevertheless, the steady state motion's amplitude was a couple of hundred metres, which is approximately 4-5 times smaller than what could be achieved in the underactuated configurations.

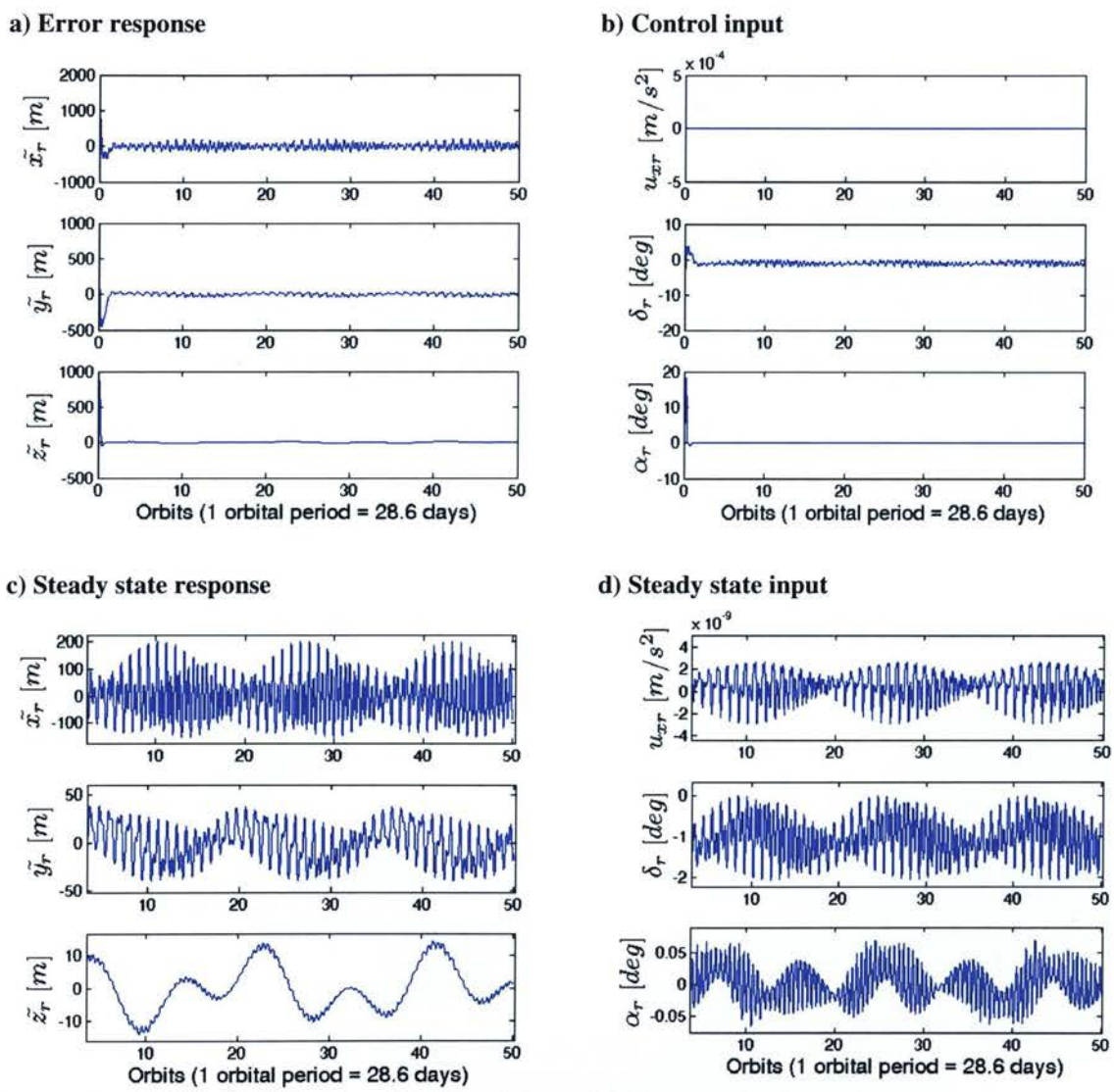

Figure 6.2 Long term simulations showing efficacy of LQR control of hybrid system

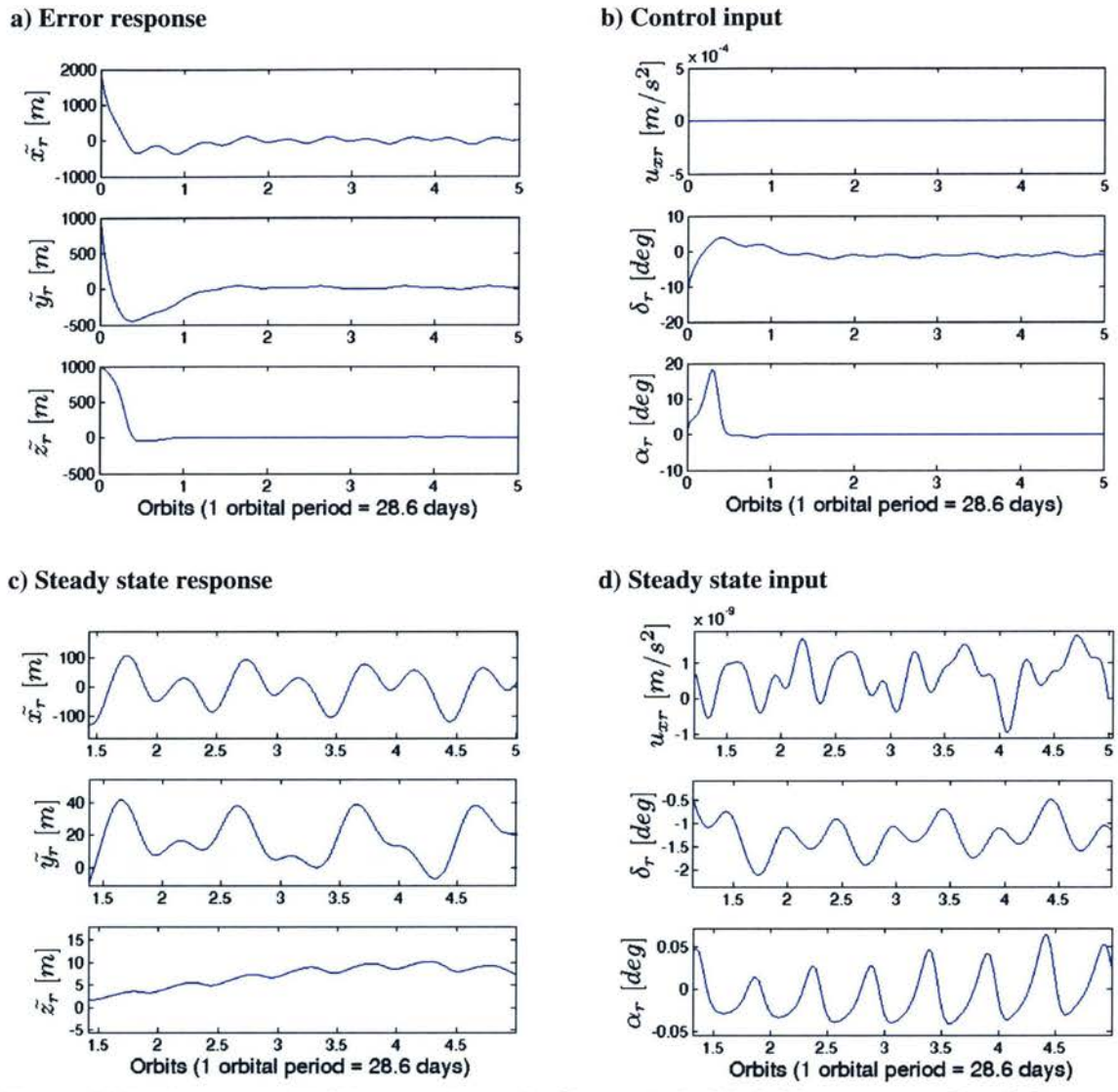

Figure 6.3 Performance of LQR controller on the Sun perturbed hybrid system over 5 periods

Observing the demanded control efforts, it can be seen that control accelerations along x_r remain small; on a scale of 10^{-9} m/s^2. This low level of acceleration is on the same scale as that demanded in the fully actuated thrusters controlled system. However, since control along y_r and out of plane motions are controlled using solar sails, fuel consumption is significantly smaller. The relative ΔV requirement was computed for motions along the x direction only and found to be approximately 0.631 mm/s/week, or one-third of that required by a purely thruster-controlled system.

The relative control angles were extremely small, particularly for control of the out-of-plane motions. Such small and precise relative angle requirements may not be attainable in practice. However, as noted in previous chapters, the Sun's perturbing effect on motion out of the orbital plane is small and out-of-plane errors only grow large after long periods of time. Approximate planar motion can still be achieved by neglecting out of plane control efforts.

6.3 Circular Trajectory Tracking

The underactuated thruster configuration was shown in Chapter 4 to be unable to track a circular reference trajectory. In that case, it was shown that unnatural spacecraft formations required large amounts of control efforts in directions that were unachievable by the underactuated system within an appropriate time frame. It was hypothesized that a fully actuated system could accomplish this task. However, as the results of Figure 6.4 show, it appears that the limitations of the solar sails also prove to be too limiting for a linear controller to track a circular formation.

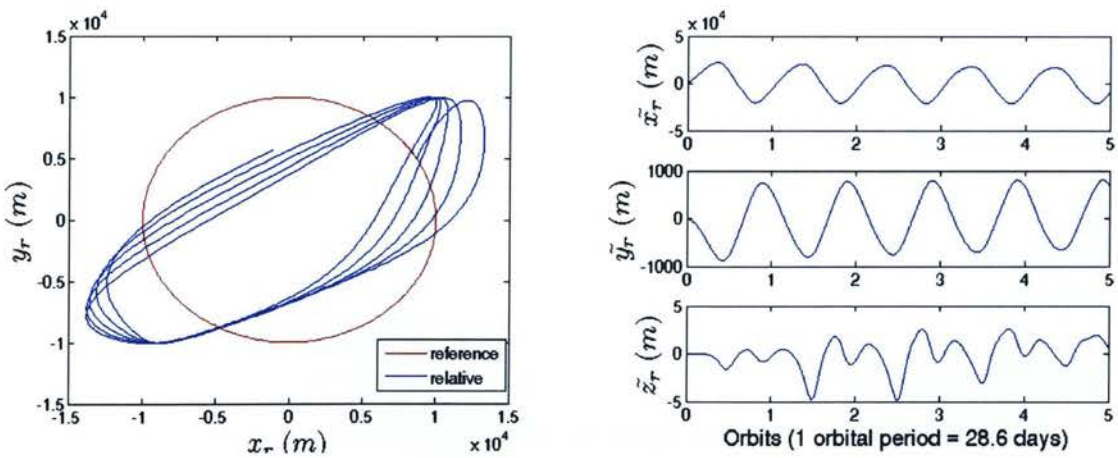

Figure 6.4 Trajectory of a hybrid system attempting to track a circular orbit

In assessing the controller performance, it is readily seen that the largest errors occured in the x_r direction. This was also the case for the underactuated thrusters system tracking the circular orbit. However, the orbit size has decreased drastically, with in-plane errors reduced by one to two orders of magnitude as compared to the underactuated thruster control scenario. Although the linear controller was not able to bring system errors to within acceptable ranges, its performance in this case highlights the challenges of maintaining unnatural formation trajectories in the event of actuation failures.

Chapter 7

Conclusions

7.1 Concluding Remarks

This thesis represents a preliminary study into the formation keeping control of a Sun perturbed spacecraft formation system orbiting the Earth-Moon L4 point. As this is a preliminary study, it should be noted that several technological advancements in solar sail and propulsion technologies would be required before the proposed control strategies in this study could be implemented. Still, this study showed that once these enabling technologies are developed, tracking of the elliptical formation trajectory could be achievable in both fully and underactuated configurations with bounded behaviour. Tracking of an in-plane circular trajectory, however, appears to only be attainable using thrusters in a fully actuated state. The use of thrusters, solar sails and a hybrid propulsion system for control actuation were examined in this thesis, and comparisons were drawn between these different methods. The main conclusions that could be drawn from the use of each of these three methods are summarized briefly here.

7.1.1 Formation Keeping Using Thrusters

The analysis of the thruster-controlled system showed that the integral augmented sliding mode controller could perform just as well or better than linear control methods. Fuel consumption was also lower when using SMC; however, one cannot definitively state that fuel consumption in general will be lower using nonlinear control methods due to uncertainty in the tuning of control parameters. Still, the use a sliding mode controller to

control the underactuated, Sun-perturbed system resulted in a lower fuel consumption than what was achieved using a LQR control scheme. The results here would favour the use of nonlinear control techniques for control of the underactuated system.

It was shown that extremely low relative control accelerations, on the order of 10^{-8} for the underactuated configurations, were sufficient to attain bounded in-plane behaviour. The periodic oscillations observed during steady state were caused by nonlinearities in the system dynamics that could not be compensated for using an underactuated thruster configuration. Short and long period oscillations were also observed when the Sun's gravity was included in the model as a perturbing force, further reflecting the limitations of the underactuated system in countering system nonlinearities.

A bang-bang controller was also developed and applied to the formation system. This was done to assess whether or not desired system performance could be attained using discontinuous control methods. It was shown that the system was controlled, but at a much higher fuel cost than with continuous methods. Nevertheless, the controller was able to bring about bounded behaviour, and thus further research into the discretized control of this system is justified.

The bulk of the cases examined in this thesis pertained to the tracking of a natural spacecraft formation trajectory in the CR3BP. In the analysis of the thruster controlled system, it was found that in-plane circular trajectories were only attained using a fully actuated configuration. The ΔV requirement for achieving this was significantly higher than that required to track the natural elliptical trajectory; in fact, more than 100 times higher. Thus, from this analysis, it would appear that reference orbit selection plays a key role in extending a mission's life. For increased reliability, it would also be wise to select a reference trajectory that could be satisfactorily tracked by an underactuated system in the event of a propulsion system fault.

7.1.2 Formation Keeping Using Solar Sails

The results shown in Chapter 5 bring to light the prospect of using solar sails for formation-keeping control. A solar-sail-controlled system is inherently underactuated, and the resulting control acceleration's direction vector is restricted in the sense that it could never point sunward. In spite of these limitations, the solar sail controlled system was still able to keep steady state motions to within ranges similar to that of the underactuated thruster-controlled system. Given that the use of solar sails requires no fuel, significant mass savings can result from the use of solar sails for formation control.

Bang-bang control was compared to the LQR control scheme and was shown to greatly outperform the latter in the Sun perturbed setting. For reasons outlined in Chapter 5, bang-bang control can be more realistically implemented for the solar sail controlled system. Furthermore, using a bang-bang control scheme can circumvent the problem of attaining small, precise relative angles required by continuous controllers.

It should be emphasized that long simulation time spans do not accurately depict the dynamics of the system, but were included only to illustrate the efficacy of the controllers and to show the expanding and contracting nature of the motions.

7.1.3 Formation Keeping Using a Hybrid Propulsion System

The hybrid system represented a fully actuated system that could take advantage of solar sails to influence motions along y_r and out of plane motions, thereby saving fuel. A linear controller was shown to adequately bound errors in the Sun gravity perturbed system to within a couple hundred metres, a much tighter tolerance than what was achieved using thrusters or solar sails alone.

As expected, fuel consumption was only one-third of that required in the fully actuated thruster-controlled system. In the event where thruster actuation along y_r fails, the hybrid control approach can be a viable secondary control method. It can even be argued that, since the hybrid system requires less fuel than that of a fully configured thruster

system, this method should become the primary control method. In which case, thrusters would form the backup control system, to be used only if actuating drives controlling the orientation of the solar sails fails, or are needed for precision maneuvers.

7.2 Future Work

This current study touched on several subjects, and can serve as a springboard for future research work. Improvements to the current dynamic model can be achieved through dynamic formulations using the elliptic restricted three body model, which would account for the eccentricity of the Earth-Moon motion. Different initial epoch conditions can also be studied to find other classes of natural spacecraft formation trajectories. Controllers developed using the elliptic model to track other natural trajectories could also be applied to ephemeris models for comparison.

A companion to spacecraft formation keeping would be attitude control. Attitude control at the Earth-Moon Lagrange points was not addressed in this study. A future study into the potential of controlling satellite orientations at these points using solar sails or thrusters in underactuated configurations would be of interest to mission designers.

A common maneuver for low Earth orbiting systems is the rendezvous maneuver, in which one spacecraft meets and joins with another, such as when a spacecraft docks with a space station. Given the risks involved with sending humans to repair a spacecraft as far away as the Lagrange point, an automated, unmanned approach to repairing systems would be more preferable. It might be possible for a repair satellite to use a hybrid propulsion system or solar sails alone to approach to within predefined ranges of the spacecraft to be repaired. A further investigation of these and other approaches may be warranted at some point.

References

[1] Aldridge, E.C., Fiorina, C.S., Jackson, M.P., Leshin, L.A., Lyles, L.L., Spudis, P.D., degGrasse Tyson, N., Walker, R.S., and Zuber, M.T., " Journey to Inpsire, Innovate, and Discover: Report to the President's Commision on Implementation of United States Space Exploration Policy," U.S. Government Printing Office, Washington, D.C., 2004.

[2] Folta, D., Hartman, K., Howell, K., and Marchand, B., "Formation Control of the MAXIM L2 Libration Point Mission," *AIAA/AAS Astrodynamics Conference Proceedings*, AIAA Paper No. 2004-5211, Providence, Rhode Island, August 2004.

[3] Darwin website (November 17, 2006), *Darwin Overview*, Retrieved on July 15, 2009, from http://www.esa.int/esaSC/120382_index_0_m.html

[4] Carpenter, K.G., Schrijver, C.J., Karovska, M, and SI Vision Mission Team., "The Stellar Imager (SI) Vision Mission", *Advances in Stellar Interferometry, Proceedings of the SPIE Conference,* paper #6268-77, May, 2006.

[5] Catlin, K.A., and McLaughlin, C.A., "Relative Motion of Two Spacecraft Near the Earth Moon Triangular Libration Points", *AIAA/AAS Astrodynamics Specialist Conference and Exhibit*, Provedence, Rhode Island, August, 2004.

[6] Farquhar, R.W., "The Control and Use of Libration-Point Satellites", *NASA TR R-346*, September 1970, pp. 89-102

[7] Wie, B., *Space Vehicle Dynamics and Control,* vol. 1, AIAA publications, Virginia, 1998.

[8] Wiesel, W.E., *Spaceflight Dynamics*, McGraw-Hill, New York, 1989.

[9] Curtis, H.D., *Orbital Mechanics for Engineering Students*, Elsevier Butterworth-Heinemann, Oxford, 2005.

[10] Szebehely, V., *Theory of Orbits: The Restricted Problem of Three Bodies*, Academic Press, New York, 1967.

[11] Gomez, G., Jorba, A., Masdemont, J., and Simo, C., *Dynamics and Mission Design Near Libration Points, vol. 1-4*, World Scientific Publishing Co., New Jersey, 2001.

[12] Mckenzie, R., and Szebehely, V., "Non-linear Stability around the Triangular Libration Points", *Celestial Mechanics*, 23, 1981, pp. 223-229.

[13] Tuckness, D.G., "Position and Velocity Sensitivities at the Triangular Libration Points", *Celestial Mechanics and Dynamical Astronomy*, 61, 1995, pp. 1 – 19.

[14] Perdios, E., and Zagouras, C.G., "Vertical Stability of Periodic Solutions around the Triangular Equilibrium Points", *Celestial Mechanics and Dynamical Astronomy,* 51, 1991, pp. 75 – 81.

[15] Deprit, A., and Bartholome, A.D., "Stability of the Triangular Lagrangian Points", *The Astronomical Journal,* Volume 72, Number 2, March 1967, pp. 173 – 179.

[16] Bhatnagar, K.B., and Hallan, P.P., "Existence and Stability of L4/L5 in the Relativistic Restricted Three-Body Problem", *Celestial Mechanics and Dynamical Astronomy*, 69, 1998, pp. 271 – 281.

[17] Blackburn, J.A., Nerenberg, M.A.H., and Beaudoin, Y., "Sateillite Motion in the Vicinity of the Triangular Libration Points", *American Journal of Physics,* Vol. 45, No. 11, November 1977, pp. 1077 – 1081.

[18] Alfriend, K.T., "Stability of and Motion About L4 at Three-to-One Commensurability", *Celestial Mechanics and Dynamical Astronomy, 4*, 1971, pp. 60 – 77.

[19] Sehnal, L., "The Stability of the Libration Points L4 and L5 in the System Earth-Moon", *Astronomical Institute of the Czechoslovak Academy of Sciences*, January 14, 1960, pp. 130 – 131.

[20] Danby, J.M.A., "Inclusion of Extra Forces in the Problem of Three Bodies", *The Astronomical Journal,* Volume 70, Number 3, 1965, pp. 181 – 188.

[21] de Vries, J.P., "The Sun's Perturbing Effect on Motion Near a Triangular Lagrange Point", *General Electric Company*, Philadelphia, Pa, Missile and Space Division, September, 1962.

[22] Breakwell, J.V., and Pringle, R., "Resonances Affecting Motion Near the Earth-Moon Equilateral Libration Points", *Progress in Astronautics and Aeronautics*, Vol. 17, Academic Press, 1965, pp. 55 – 73.

[23] Schutz, B.E.., "Application of Von Zeipel's Method to Motion About the Earth-Moon Triangular Libration Points Including the Influence of the Sun", Phd Dissertation, University of Texas at Austin, 1969.

[24] Kamel, A.A., "Perturbation Theory Based on Lie Transforms and its Application to the Stability of Motion Near Sun-Perturbed Earth-Moon Triangular Libration Points", Phd Dissertation, Stanford University, 1970.

[25] Schechter, H.B., "Three Dimensional Nonlinear Stability Analysis of the Sun-Perturbed Earth-Moon Equilateral Points", *AIAA Journal*, Vol. 6, No. 7, July 1968, pp. 1223 – 1228.

[26] Tapley, B.D., and Lewallen, J.M., "Solar Influence on Satellite Motion Near the Stable Earth-Moon Libration Points", *AIAA Journal*, Vol. 2, No. 4, April 1964, pp. 728-732.

[27] Tapley, B.D., and Schutz, B.E., "Further Results on Solar Influenced Particle Motion near Earth-Moon Libration Points", *AIAA Journal*, Vol. 3, No 10, 1965, pp 1954-1956.

[28] Tapley, B.D., and Schutz, B.E., "Numerical Studies of Solar Influenced Particle Motion near the Triangular Earth-Moon Libration Points", *In Periodic Orbits, Stability and Resonances*, 1970, pp. 128-142.

[29] Bhatnagar, K.B., Gupta, U., and Bhardwaj, R., "Effect of Perturbed Potentials on the Non-Linear Stability of Libration Point L4 in the Restricted Problem", *Celestial Mechanics and Dynamical Astronomy*, 59, 1994, pp. 345 – 374.

[30] Hallan, P.P., Jain, S., and Bhatnagar, K.B., "The Non-linear Stability of L4 in the Restricted Three Body Problem When the Bigger Primary is a Triaxial Rigid Body and a Source of Radiation", *Indian Journal of Pure and Applied Mathematics*, 32(7), July 2001, pp. 1081 – 1116.

[31] Devi, S.G., and Singh, R., "Location of Equilibrium Points in the Perturbed Photogravitational Circular Restricted Problem of Three Bodies", *Astronomical Society of India Bulletin*, 22, 1994, pp. 433 – 437.

[32] Kunitsyn, A.L., and Perezhogin, A.A., "On the Stability of Triangular Libration Points of the Photogravitational Restricted Circular Three-Body Problem", *Celestial Mechanics*, 18, 1978, pp. 395 – 408.

[33] Kumar, V., and Choudhry, R.K., "Nonlinear Stability of the Triangular Libration Points for the Photogravitational Elliptic Restricted Problem of Three Bodies", *Celestial Mechanics and Dynamical Astronomy*, 48, 1990, pp. 299 – 317.

[34] Kumar, V., and Choudhry, R.K., "On the Stability of the Triangular Libration Points for the Photogravitational Circular Restricted Problem of Three Bodies When Both of the Attracting Bodies are Radiating as Well", *Indian Journal of Pure and Applied Mathematics*, 18(11), November 1987, pp. 1023 – 1039.

[35] Colombo, G., Lautman, D., and Munford, C., "On the Libration Orbits of a Particle Near the Triangular Point in the Semirestricted Three-Body Problem", *The Astronomical Journal*, Volume 68, Number 3, April, 1963, pp. 159 – 162.

[36] Valdes, F., and Freitas, R.A., "A Search for Objects Near the Earth-Moon Lagrangian Points", *Icarus*, 53, 1983, pp. 453 – 457.

[37] Jorba, À., "A Preliminary Numerical Study on the Existence of Stable Motions Near the Triangular Points of the Real Earth-Moon System", University of Barcelona, 2000.

[38] Lissauer, J.J., and Chambers, J.E., "Solar and Planetary Destabilization of the Earth-Moon Triangular Lagrangian Points", *Icarus*, 195, 2008, pp. 16 – 27.

[39] Schutz, B.E., "Orbital mechanics of space colonies at L4 and L5 of the Earth-Moon System", *AIAA, 15th Aerospace Sciences Meeting*, Los Angeles, California, January, 1977.

[40] Munoz, J.P., "Sun-Perturbed Dynamics of a Particle in the Vicinity of the Earth-Moon Triangular Libration Points", Phd Dissertation, University of Texas at Austin, August 2008.

[41] Kolenkiewicz, R., and Carpenter, L., "Stable Periodic Orbits About the Sun Perturbed Earth-Moon Triangular Points", *AIAA Journal*, Volume 6, No. 7, July 1968, pp. 1301 – 1304.

[42] Rand, R., and Podgorski, W., "Geometrical Dynamics: A New Approach to Periodic Orbits Around L4", *Celestial Mechanics*, 6, 1972, pp. 416 – 420.

[43] Deprit, A., Henrard, J., Palmore, J., and Price, J.F., "The Trojan Manifold in the System Earth-Moon", *Monthly Notices of the Royal Astronomical Society*, Vol. 137, 1967, pp. 311 – 335.

[44] Henrard, J., "The Web of Periodic Orbits at L4", *Celestial Mechanics and Dynamical Astronomy*, 83, 2002, pp. 291 – 302.

[45] Segerman, A.M. and Zedd, M.F., "Preliminary Planar Formation Flight Dynamics Near Sun Earth L2 Point", *Advances in the Astronautical Sciences Paper*, Vol 114, 2003.

[46] Luquette, R.J., and Sanner, R.M., "Linear State-Space Representation of the Dynamics of Relative Motion, Based on Restricted Three Body Dynamics", *AIAA Guidance, Navigation and Control Conference and Exhibit Proceedings*, August 2004.

[47] Howell, K.C., and Marchand, B.G., "Natural and Non-natural Spacecraft Formations Near the L1 and L2 Libration Points in the Sun-Earth/Moon Ephemeris System", *Dynamical Systems: An International Journal*, Vol. 20, No. 1, March 2005, pp. 149 – 173.

[48] Howell, K.C., and Marchand, B.G., "Control Strategies for Formation Flight in the Vicinity of the Libration Points", *Journal of Guidance, Control, and Dynamics*, Vol. 28, No. 6, November, 2005, pp. 1210 – 1219.

[49] Li, H., "Application of Solar Radiation Pressure to Formation Control Near Libration Points", Phd Dissertation, University of Cincinnati, February 2008.

[50] Catlin, K.A., and McLaughlin, C.A., "Earth Moon Triangular Libration Point Spacecraft Formations", *Journal of Spacecraft and Rockets*, Vol. 44, No. 3, May-June 2007.

[51] McInnes, C.R., *Solar Sailing: Technology, Dynamics and Mission Applications*. Springer, Berlin, 2004.

[52] McInnes, C.R., McDonald, A.J., Simmons, J.F.L., and MacDonald, E.W., "Solar Sail Parking in Restricted Three-Body Systems", *Journal of Guidance, Control and Dynamics*, Vol. 17, No. 2, March, 1994, pp. 399 – 406.

[53] Smirnov, G.V., Ovchinnikov, M., and Guerman, A., "Use of Solar Radiation Pressure to Maintain a Spatial Satellite Formation", *Acta Astronautica*, 61, 2007, pp. 724 – 728.

[54] Baoyin, H., and McInnes, C.R., "Solar Sail Orbits at Artificial Sun-Earth Libration Points", *Journal of Guidance, Control, and Dynamics*, Vol. 28, No. 6, November, 2005, 1328 – 1330.

[55] Burns, R.S., *Advanced Control Engineering*, Butterworth-Heinemann, Oxford, 2001.

[56] Slotine, J.J.E. and Li, W., *Applied Nonlinear Control*, Prentice Hall, New Jersey, 1991.

[57] DeCarlo, R.A., Zak, S.H. and Matthews, G.P., "Variable Structure control of Nonlinear Multivariable Systems: A Tutorial", *IEEE Proceedings*, Vol. 76, No. 3, pp. 212-232, March 1988.

[58] Eker, I., and Akmal, S.A., "Sliding mode control with integral augmented sliding surface: design and experimental application to an electromechanical system", *Journal of Electrical Engineering (Archiv fur Elektrotechnik)*, Springer Berlin, Vol. 90, No. 3, pp. 189 – 197, June 2007.

[59] Godard, and Kumar, K.D., "Robust Attitude control of Underactuated Spacecraft Based on Variable Structure Techniques", *(Submitted to) IEEE transactions on Aerospace and Electronic Systems*, July 2009.

[60] Moler, C., *Numerical Computing with MATLAB*, SIAM, Philidelphia, 2004.

[61] Mathworks website, (n.d), *Differential Equations in MATLAB*, Retrieved Sept. 5, 2009, from http://www.mathworks.com/support/tech-notes/1500/1510.html#fixed